A CUSP IN PION-PROTON ELASTIC SCATTERING

A thesis submitted for the
degree of Doctor of Philosophy of
the University of London

by

Hidangmayum Nandakumar Sarma

The Blackett Laboratory of Physics,
Imperial College,
London, S.W.7.

August, 1976.

Abstract

The $\pi^- p$ elastic scattering cross-section is measured in the range of $\cos\theta^* \simeq -0.60$ to $\cos\theta^* \simeq 0.80$, in the centre of mass system using a system of drift chambers surrounding a liquid hydrogen target. The measurements are made in the range of incident pion momentum between 0.600 GeV/c and 0.780 GeV/c.

A cusp has been observed in the elastic differential cross-section across the threshold for η meson production. Relative phases of the S_{11} wave and $f(\theta^*, K)$, the non-spin flip amplitude, are extracted from the behaviour of the cusp as a function of $\cos\theta^*$. The production cross-section of $\pi^- p \rightarrow \eta n$ is also extracted from the behaviour of the cusp and is found to be $\sigma_{reac} / p^*_{\eta n} \geqslant (19.91 \pm 0.87)$ μb/(MeV/c).

The phase of the S_{11} wave at the η-threshold is $\delta_0 = 25.13^\circ \pm 1.59^\circ$. There is no evidence for any narrow N^* across the threshold for η-production.

Contents

			Page
	Abstract		i
1.	Introduction		
	1.1	$\pi^- p$ elastic scattering	1
	1.2	Phase shift analysis	3
	1.3	η meson production in $\pi^- p$ interaction	11
	1.4	η meson production near its threshold	12
2.	Theory		
	2.1	$\pi^- p$ elastic scattering differential cross-section	17
	2.2	Elastic scattering differential cross-section near η-threshold	19
3.	Apparatus (Beam line)		
	3.1	Beam	26
	3.2	Floating wire measurement	29
	3.3	The liquid hydrogen target	34
4.	Apparatus (Detecting system)		
	4.1	Drift chamber	37
	4.2	Mechanism of drift chamber	37
	4.3	Diffusion without electric field	39
	4.4	Diffusion in electric field	41
	4.5	Different types of drift chambers	42
	4.6	Left and right ambiguities and position measurement	46
	4.7	Imperial College drift chambers	49
	4.8	Test of the Imperial College drift chambers	52

Page

5. Data collection

5.1 Logic system 57

5.2 Mode of data collection 60

6. Data analysis

6.1 Enriching the data 64

6.2 Writing DST (Data Summary Tape) 65

6.3 Rate effect 79

6.4 Corrections for systematic effects 80

6.5 Differential cross-sections 84

7. Cusp

7.1 Cusp in $\pi^- p$ elastic scattering differential cross-sections 97

7.2 Relative phase of S_{11} and $f(\theta^*, K)$ 101

7.3 η -production cross-section 107

7.4 Spin flip and non-spin flip cross-sections 108

7.5 Phase of S_{11} and $f(\theta^*, K)$ 111

8. Conclusions 119

Acknowledgements 121

References 122

1. Introduction

This thesis describes an experiment carried out at the Rutherford Laboratory, using the 8 GeV Proton Synchrotron, Nimrod, by the Imperial College counter group of which the author was a member. This experiment was part of a series to study boson resonances near threshold, to study the curious behaviour of ω and X^0 meson production, to set a lower limit for the X^0 width and to search for cusps near the η-threshold in $\pi^- p$ elastic scattering.

$\pi^- p$ elastic scattering cross-sections were measured with drift chambers surrounding the liquid hydrogen target and ω and X^0 production were studied by detecting neutrons with neutron counters. For the width of the X^0, one of the decay products of the X^0 was simultaneously detected in the drift chambers, thus giving the interaction point in the liquid hydrogen target.

A large amount of experimental work has been done on the elastic scattering of $\pi^- p$ at intermediate energies. A brief survey of this work is given below.

1.1 $\pi^- p$ elastic scattering

Duke et al (1966) measured the differential cross-section of $\pi^- p$ elastic scattering at incident beam momenta in the range 0.875 to 1.579 GeV/c by a counter technique at RHEL. Using two arrays of scintillation counters, the scattered pions from a liquid hydrogen target were detected in coincidence with recoiling protons. The differential cross-sections were measured at eighteen angles in the range $-0.97 \leqslant \cos\theta^* \leqslant 0.75$, at thirteen incident beam momenta.

Abillon et al (1972) measured the elastic differential cross-section in the range $0.92 \leqslant \cos\theta^* \leqslant 0.99$ at fifteen momenta between 0.875 and 1.58 GeV/c using magnetostrictive spark chambers and a magnet for momentum analysis.

Crabb et al (1971) used a double arm spectrometer to measure the differential cross-section near $\cos\theta^* \simeq -1.0$, at thirtythree incident pion momenta in the range 0.600 to 1.280 GeV/c.

Rothschild et al (1972) studied $\pi^- p$ elastic scattering cross-sections near $\cos\theta^* = -1.0$ using a double arm spectrometer in the momentum range 0.572 to 1.628 GeV/c. The differential cross-section exhibits peaks at 0.690, 0.970 and 1.430 GeV/c.

Brody et al (1971) measured the total and differential cross-sections of $\pi^- p$ elastic scattering at thirtyfive momenta between 0.557 and 1.660 GeV/c in a bubble chamber experiment. They normalized their data to the counter experiment results in the range of scattering angle, $-0.80 \leqslant \cos\theta^* \leqslant 0.70$.

Debenham et al (1975) measured the differential cross-section of $\pi^- p$ elastic scattering near $\cos\theta^* \simeq -1.0$, by detecting recoil protons by a time-of -flight technique at fiftytwo momenta in the range 0.600 to 1.000 GeV/c. The data show a cusp like behaviour near the ηn threshold.

Richards et al (1974) measured $\pi^- p$ elastic differential cross-section at thirtyfive incident momenta in the momentum range 0.600 to 1.280 GeV/c, over the angular range $\cos\theta^* \simeq -0.906$ to -0.998. They used a double arm spectrometer. In the momentum range between 0.700 to 0.900 GeV/c, the slope of the backward angular distribution goes rapidly through zero from negative to positive. Two prominent dips appear at 0.880 and 1.150 GeV/c in the elastic differential cross-sections at $\cos\theta^* = -1.0$.

In Table 1.1 we have shown some of the $\pi^- p$ elastic scattering experiments.

Table 1.1

Experiment	Accelerator	Momentum range GeV/c	Number of momenta	Experimental technique
Brody (1971)	ZGS/Bevatron	0.557-1.660	35	Bubble chamber
Rothschild (1972)	Bevatron	0.572-1.628	44	Double arm counter
Debenham (1975)	Nimrod	0.600-1.000	52	Counter
Duke (1966)	Nimrod	0.875-1.579	13	Counter
Richards (1974)	Bevatron	0.600-1.270	33	Double arm counter

1.2 Phase shift analysis

The meeting ground of large quantities of experimental data and proposed theories in pion-nucleon system is the phase shift analysis. Since 1965 phase shift analyses have been in general agreement with the interpretation of pion-nucleon scattering below 1.000 GeV/c, incident pion momentum. S_{11}, P_{11} and D_{13} partial waves show resonant behaviour in the region about 0.700 GeV/c, while D_{15} and F_{15} waves are also important in the range of 1.000 GeV/c. The approach of the various groups in the phase shift analysis is different and we will briefly summarize their work here.

Roper et al (1965) obtained the phase shifts as a function of energy by considering simultaneously all data in the energy range of interest (0-700 MeV). They parametrized the phase shifts and absorption parameters as polynomials in c.m. momentum or some partial waves as Breit-Wigner resonances. The correct threshold behaviour is guaranteed for the phase shifts and approximated for the absorption parameters. Unitarity was preserved in their solutions. Though the idea of parametrizing the phase shifts as a function of energy appears to be basically sound there are some arguments against this parametrization.

i) The threshold behaviour may not be correctly predicted.

ii) Satisfaction of the dispersion relation which connects the real and imaginary parts of partial wave amplitude is not guaranteed.

They found that the phase shift of the P_{11} amplitude went through 90° at M=1485 MeV. This is known as the Roper resonance, and subsequent analyses have confirmed its existence.

Bransden et al (1965) performed a phase shift analysis with energy independent parameters in the energy range 0.300-0.700 GeV. Their parametrization was based on a dispersion relation satisfied by analytic properties of the partial wave scattering amplitudes and thus ensured unitarity. Though, in principle their method of parametrization is capable of reproducing behaviour of any degree of complexity; in practice because of the number of limited parameters, their result can reproduce a reasonably smooth behaviour with energy of each partial wave. So if the physical partial wave amplitudes are not smooth in their energy dependence, they expect their solutions will still reproduce gross features of the amplitudes while ignoring the fine structure. Both their solution 1 and solution 2 show an η-threshold cusp at 0.558 GeV in S_{11} wave. They noted that since S wave is in a region where other waves are strongly varying the direct experimental observation of the cusp is almost impossible.

Auvil et al (1964) performed an energy independent phase shift analysis from 0.300-0.700 GeV using dispersion relations. They found a notable inelastic cusp in S_{11} wave at the threshold for η-production, the magnitude of which was consistent with η-production cross-section. Coinciding with this cusp in the inelasticity, the S_{11} phase rises sharply to 60° and falls backs. This is obviously due to the Ball-Frazer mechanism (1961) which means a rapid rise in the real part of a phase is associated with a rapid rise in inelasticity, which may not be necessarily the production of an actual resonance. Their phase family differs considerably from Roper's.

Bareyre et al (1965) fitted all waves freely. The only assumption made was a regular behaviour with energy of the partial waves. The interval between the energies at which the analysis has been done was of the order of 50 MeV. They found that only one set of phase shifts could be joined smoothly with the solution found at lower energy. In their 1968 phase shift analysis (Bareyre et al 1968) they essentially used the same method of 1965 but included more input data and extended upto higher energy 1.600 GeV. They claim the resulting solution to have a high probability of being the real solution, because at each energy, the fit of the experimental data is good and maintain a fair continuity for the variation of partial wave amplitudes with energy. If there are any important discontinuities (cusps or other mechanisms), they expect their solution will be inadequate. However, they feel that an important discontinuity is quite improbable. The cusp that has been found in the S_{11} wave at η-threshold in Bransden et al (1965) was only because it was forced in the parametrization. The strong inelastic effect in the S_{11} state which appears near a mass of 1535 MeV has been correlated to the rise above threshold of the η-production cross-section. The behaviour of S_{11} below 1.000 GeV has been interpreted with a general formulation as the sum of an inelastic and an elastic resonance.

An energy independent analysis using the method of least squares was performed by Cence (1966) from 0.300 to 0.700 GeV. His solution differed from previous ones in that no phase shift lies outside $\pm 45^{\circ}$ except P_{33} which is approaching 180°. In qualitative agreement with others Cence's solution has a large phase shift, $\delta(S_{11})$, reaching a peak of $+35^{\circ}$, accompanied by the sudden onset of absorption at 0.580 GeV. This is due to the opening of the two body channel $\pi^{-}p \rightarrow \eta n$, which is known to occur in the S_{11} state near threshold. The S_{11} absorption in his solution is sufficient to give the cross-section for the reaction $\pi^{-}p \rightarrow \eta n$. His set of phase shifts and absorption parameters do not show any resonance except for P_{33} [Δ (1236)]. According to his analysis the large bump at 0.600 GeV ($M_{\pi p} = 1512$ MeV) is not due to a resonance, since none of the partial waves shows a resonant behaviour in that region.

Donnachie et al (1968) in their phase shift analysis used partial wave dispersion relations, which can smoothen the phase shifts and eliminate structures which violate causality. By using phase shifts from an energy independent analysis of the data, dispersion relations were evaluated and new phases and absorption parameters were calculated. The predictions were then included with the experimental data as input for another analysis and the process was iterated until the experimental phase shift analyses and theoretical dispersion relation fits move very close to each other. These two solutions are known as CERN Experimental and Theoretical solutions respectively. They claimed nine new resonances and emphasised that it was not possible to find any resonably continuous solution without several new resonances, unless the experimental data are seriously wrong.

Another two solutions, known as Glasgow A and Glasgow B were derived by Davies (1970). They break up the energy range 0.310-1.450 GeV into intervals of about 100 MeV and parametrized the phase shifts (δ) and absorption parameters (η) in each energy range as quadratics in the c.m.

momentum. In the next interval, quadratic parameters were sought that encouraged the continuity in phase shift. The Wigner condition prohibiting fast clockwise circling in amplitudes in their Argand diagrams was used to reject some fits. To give the connection between the energy dependence of η and δ , implied by partial wave dispersion relations, the opportunity of showing itself, they relaxed their continuity constraints on the derivatives of η or δ if the other was varying rapidly. Having found a solution for the whole energy range in this way phase shifts were fitted by Breit-Wigner resonances with background, and parameters of these were adjusted by comparing with experimental data to give solution A. Solution B was derived by the same method of resonance fitting but started from CERN Experimental phase shifts.

One of the surprising results of solution B is the narrow resonance 36 MeV width just at the threshold for η-production, then a very broad one at 1766 MeV. Such a narrow resonance is quite contrary to the interpretation of the η- production cross-section with abroader width S_{11} (Davies et al 1967).

Brody et al (1969) made a comparision of different phase shift solutions and pointed out that the dispersion relation fit of CERN Theoretical solution showed a marked discrepancy with the experimental data. They also pointed out that by smoothing the partial wave phase shifts by imposing theoretical conditions one can extract the resonance parameters more accurately. However it is extremely difficult to determine the significance of fine structures observed in the partial wave phase shifts and to determine which of these structures needs to be smoothed out.

In Figs. 1.1(a), (b) and (c) we show a compilation of $\pi^- p$ elastic scattering differential cross-sections at Cos θ^* =0.60, Cos θ^* =-0.20 and Cos θ^* =-0.60 respectively, for different phase shift solutions.

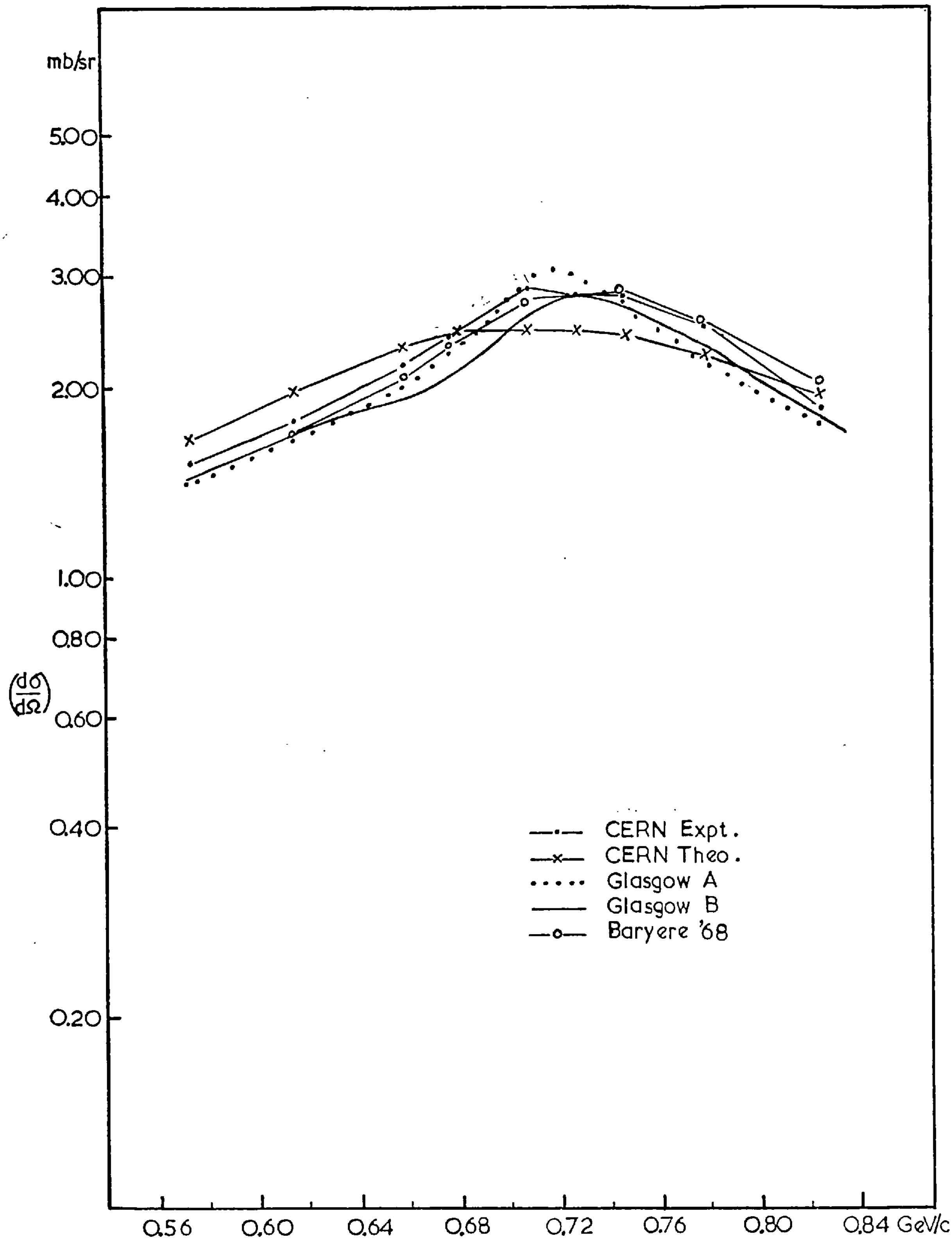

FIG. 1.1 (a) $\pi^- p$ Elastic scattering at $\cos\theta^* = 0.60$

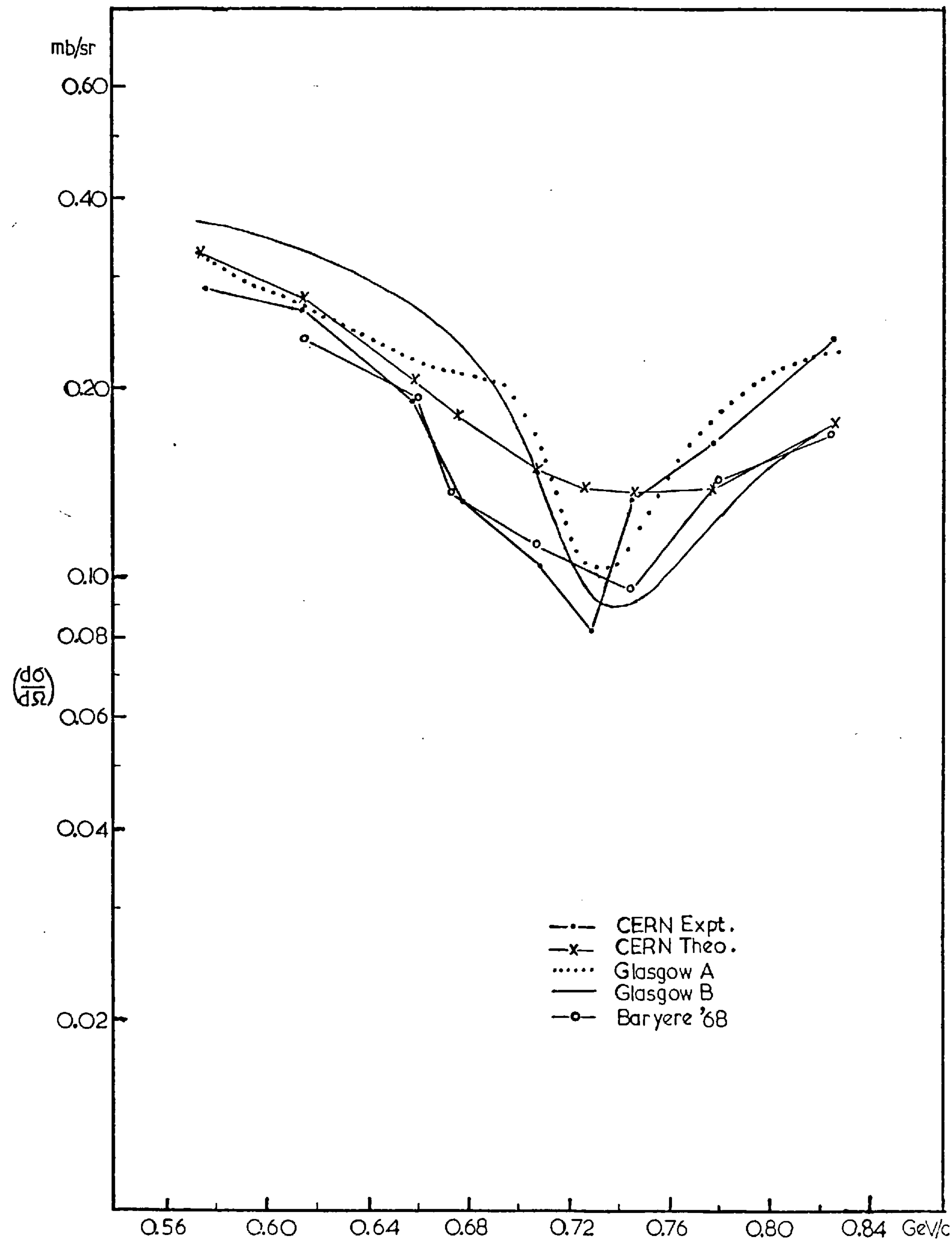

FIG. 1.1 (b) $\pi^- p$ Elastic scattering at $\cos\theta^* = -0.20$

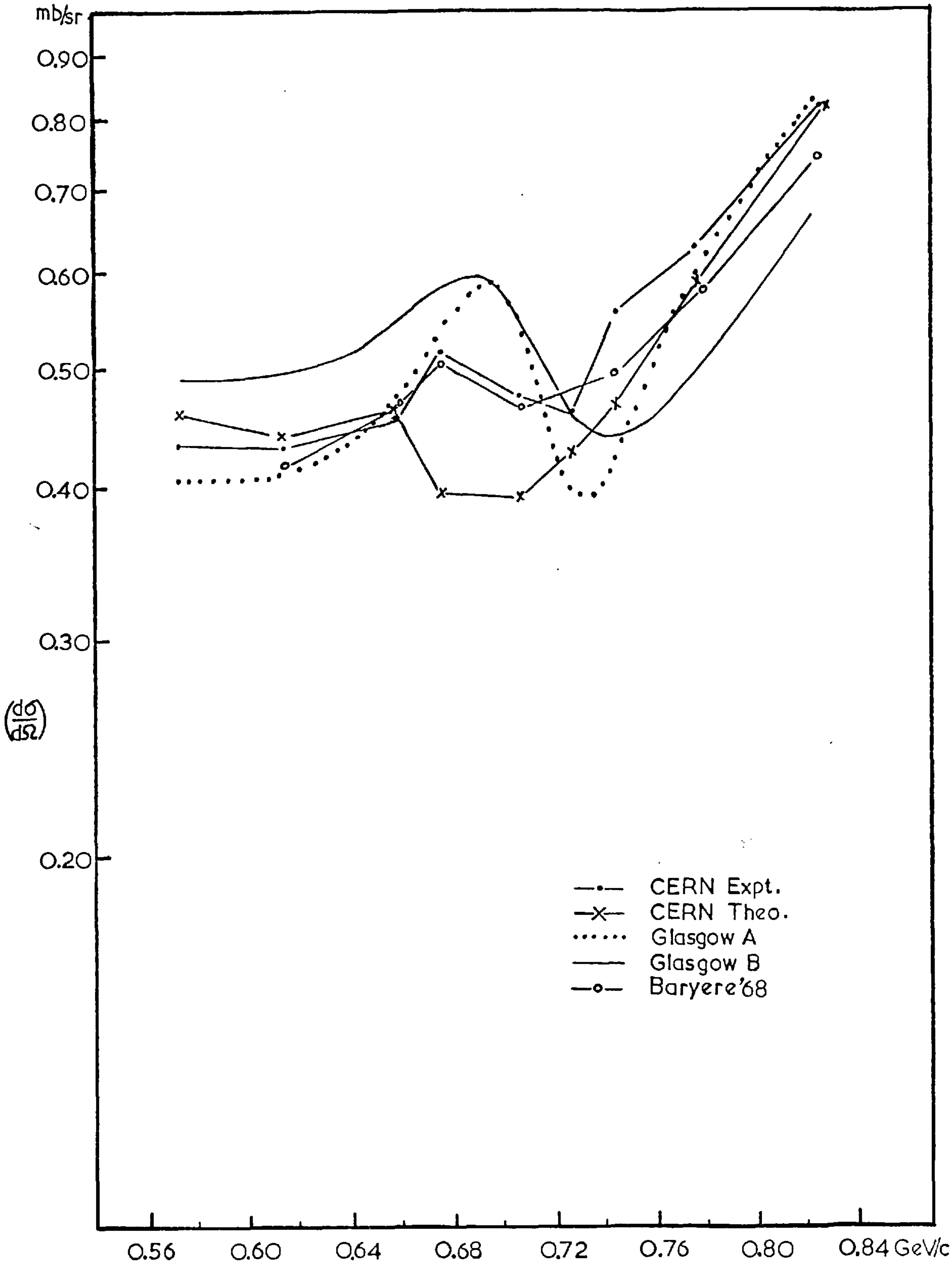

FIG. 1.1(c) $\pi^- p$ Elastic scattering at $\cos\theta^* = -0.60$

1.3 η meson production in $\pi^- p$ interaction.

The η meson was discovered by Pevsner et al (1961) in the interaction of π^+ in a deuterium bubble chamber at 1.23 GeV/c. The observed bump in the effective mass distribution of $\pi^+\pi^-\pi^o$ system in the reaction $\pi^+ d \rightarrow p p \pi^+\pi^-\pi^o$ was attributed to the production of a particle of mass 546 MeV. The current value of η mass is 548.8 ± 0.6 MeV (Particle Data Group 1976). The quantum numbers of the η meson are $I^G (J^P) C_n = 0^+ (0^-) +$ and the width $\Gamma = (2.63 \pm 0.58)$ KeV. The η meson fits well into the SU(3) octet of 0^- mesons as the I = 0, Y = 0 member and its mass approximately satisfies the octet mass formula,

$$3 m_\eta^2 = 4 m_K^2 - m_\pi^2 \qquad (1.1)$$

The η is free to mix with SU(6) singlet 0^- state, but the mixing is expected to be small as the singlet and octet are in different SU(6) multiplets. $\eta'(959)$ is the best candidate for SU(6) singlet state. All known η decays are via electromagnetic interactions.

The two models for η production are shown in Figs. 1.2(a) and 1.2(b)

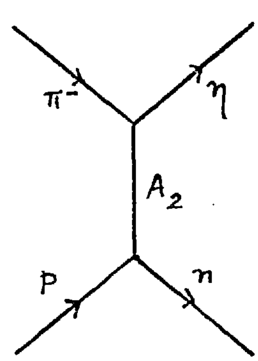

Peripheral Model
(A_2 exchange)
Fig 1.2 (a)

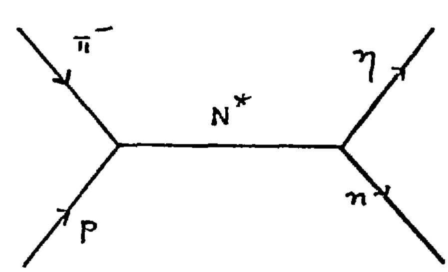

Isobar Model
Fig 1.2 (b)

Though the peripheral model and its extensions, the absorption model and the Regge pole model, have great success in explaining many of the production processes in particle physics, η-production in $\pi^- p$ reaction is not a good candidate for a simple peripheral model. The Isobar model can explain most of the bumps and shoulders observed in the energy dependence of the total cross-sections. The exchange of an A_2 meson of mass (1310 $\pm$ 10) MeV in the peripheral model implies the shorter range of interaction and its effect will be important only at high energies. The Regge pole model in η -production has an advantage that only one Regge trajectory associated with A_2 can contribute. Philip and Rarita (1965) analysed the η -production data of Guisan et al (1965) from 5.938 GeV/c to 18.239 GeV/c and found it to be consistent with a single Regge trajectory which was in turn consistent with A_2 mass.

1.4 η meson production near its threshold

Much work has been done on interpreting η total and differential cross-sections and the observed effect of the η -threshold on the S_{11} partial wave. A brief review of the analyses of the various authors is given below.

(i) Uchiyama - Campbell (1965) analysed $\pi^- p \rightarrow \eta n$ data using zero-effective range approximation for the S- matrix. He fitted the S_{11} phase shifts and absorption parameters of Auvil et al (1964) assuming that πN and ηN channels constituted two channels, found no pole in the vicinity of the inelastic threshold and concluded that the rising of the inelastic cross-section in $\pi N \rightarrow \eta N$ is not rapid enough to imply a pole near the threshold.

(ii) Dobson (1966) has performed a two channel scattering length analysis on $\pi^- p \rightarrow \eta n$ data and elastic $\pi^- p$ data using Auvil et al (1964) and Cence's (1966) phase shifts. He found that Auvil et al (1964) phase shifts would require a Breit-Wigner type resonance in

ηn channel with mass $M \simeq 1510$ MeV, while Cence's phase shift would require a "virtual" state at mass $M \simeq 1460$ MeV. His fit to the ηn total cross-section is shown in Fig. 1.3. Although high energy points are in agreement with data, it misses the lowest energy points.

(iii) Ball (1966) has constructed a dynamical model of the η-nucleon interaction which satisfies the requirements of analyticity and unitarity. His fit to the ηn cross-section is shown in Fig. 1.3, and misses the lowest energy points. His model predicts a virtual state pole below ηn threshold at a mass 1420-1460 MeV.

(iv) Hendry and Moorhouse (1965) examined the pion-nucleon scattering data together with η-production cross-section at energies very close to η-threshold. They consider the possibility that the S_{11} pion-nucleon scattering below η-threshold is elastic, and above the threshold the inelasticity is solely provided by η-production, since Bulos et al (1964) data indicated an approximately linear rise in the η-production cross-section with ηn c.m. momentum. However, when they compare the phase shift analyses data and experimental cross-section for η-production, the two channel hypothesis does not give a good fit. On the basis of their search for a resonance to introduce a third channel, they explained the rapid energy variation in the η-production cross-section and phase shift analyses around η-threshold in terms of a resonance lying 20-30 MeV above the η-threshold at about 1510 MeV with a full width of about 100 MeV. Their fit to the η-production cross-section is shown in Fig. 1.3.

(v) Davies and Moorhouse (1967) explored the possibility that the large η-production cross-section is not connected with S_{11} resonance,

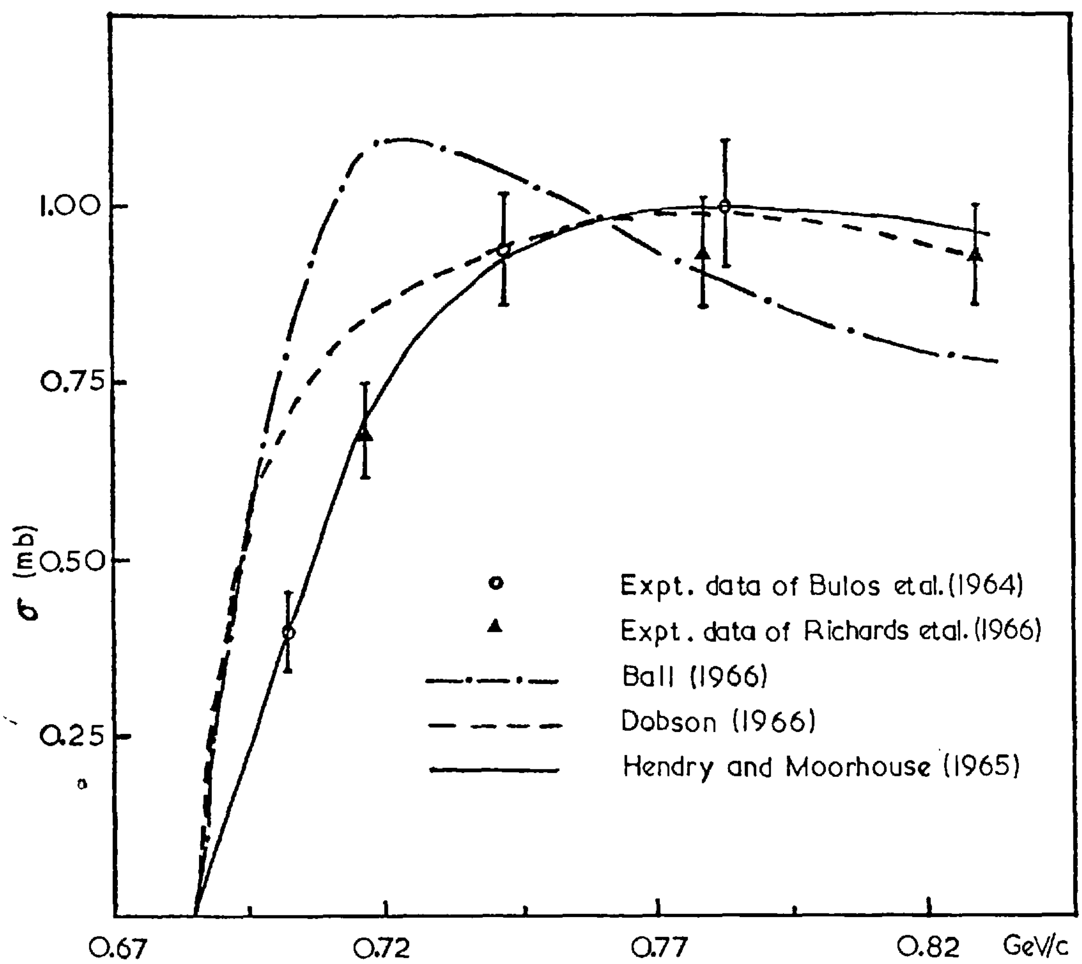

FIG. 1.3 Cross-section for $\pi^- + p \rightarrow \eta + n$; $\eta \rightarrow 2\gamma$ as a function of pion momentum. The continuous curves are various fits to experimental data (Davies and Moorhouse 1967).

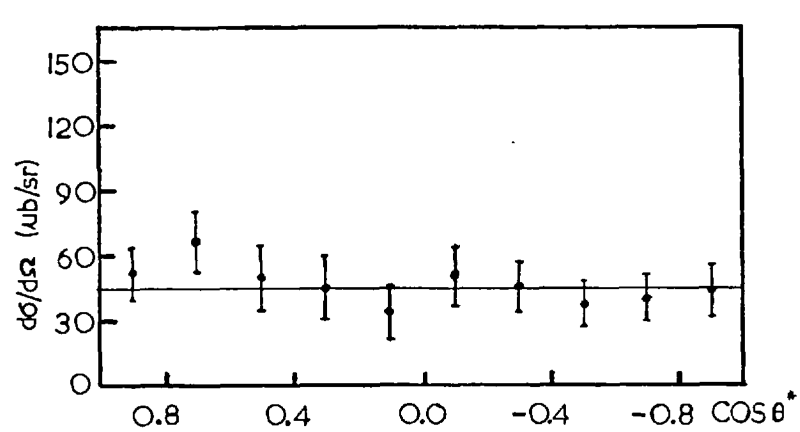

FIG. 1.4 Partial differential cross-section for η production at pion momentum of 0.718 GeV/c (Richards et al. 1966).

but produced by other amplitudes. After trying different fits they found that a good fit required the S_{11} resonance contribution to be at least 90% of the peak of the ηn cross-section.

(vi) Debenham et al (1975) fitted the differential cross-section of $\pi^- p \rightarrow \eta n$ at $\cos\theta^* = -1.0$ with a model incorporating only direct channel resonances and poles. They found that P_{11} (1530 MeV) as claimed by Lemoigne et al (1973) was not essential to fit the data. There was no evidence for a narrow N^*. Such a narrow N^* is claimed near η - threshold by Davies (1970) in his phase shift analysis solution (Glasgow B).

Richards et al (1966) measured the total and differential cross-section for the reaction $\pi^- p \rightarrow \eta n$ ($\eta \rightarrow 2\gamma$). Their η angular distribution is isotropic near threshold, but require terms through $\cos^2\theta^*$ for adequate fit for $T_{\pi^-} = 655$ MeV. Fig. 1.4 shows their partial differential cross-section at pion momentum of 0.718 GeV/c. Jones (1966) measured the η -production cross-section ($\eta \rightarrow 2\gamma$) very near to the threshold and found a linear rise in η -production cross-section upto $p^*_\eta \simeq 80$ MeV/c. The value of the η -production cross-section is $\sigma / p^*_\eta \simeq 17.0 \pm 2.3$ μb/ (MeV/c) . Binnie et al (1973) measured the η -production cross-section near to its threshold and found a linear rise of cross-section at a rate of $\sigma / p^*_\eta \simeq 21.2 \pm 1.8$ μb/ (MeV/c). They have also recalculated the value of Jones (1966), using more recent values of the $\eta \rightarrow$ neutral branching ratio and neutron counter efficiency and found $\sigma / p^*_\eta = 22 \pm 3$ μb/ (MeV/c) in good agreement with their result. Feltesse et al (1975) fitted their angular distribution data for $\pi^- p \rightarrow \eta n$ ($\eta \rightarrow 2\gamma$) with Legendre polynomials:

$$\left(\frac{d\sigma}{d\Omega}\right) = \chi^2 \sum_{l=0}^{l=max} C_l \, P_l \, (\cos\theta^*) \qquad (1.2)$$

and found a linear rise of C_0 upto $p^*_\eta \simeq 100$ MeV/c with all the other coefficients being zero, suggesting the crucial role of S_{11} wave in η-production.

From all these considerations it is plausible to assume that just near threshold, η meson is produced in S wave. In the next chapter we have derived the behaviour of elastic differential cross-section of $\pi^- p$ elastic scattering across the threshold for η -production.

2. Theory

In this chapter we examine the behaviour of the $\pi^- p$ elastic scattering cross-section across the threshold for η-production, assuming η is produced in S-wave near its threshold.

2.1 $\pi^- p$ elastic scattering differential cross-section

In order to understand the behaviour of elastic differential cross-section near η-threshold, we express the differential cross-section in terms of partial waves.

The asymptotic wave function which describes the scattering in the centre of momentum system is

$$\psi(r) = e^{ikz} + F(\theta^*, k) \frac{e^{ikr}}{r} \qquad (2.1)$$

where K is the c.m. momentum. The first term in (2.1) represents the incoming wave along the positive z - axis and the second term represents the scattered wave as an outgoing spherical wave. The differential cross-section is,

$$\left(\frac{d\sigma}{d\Omega}\right) = \left| F(\theta^*, k)\right|^2 \qquad (2.2)$$

The general expression for $F(\theta^*, K)$ in terms of partial waves can be expressed as

$$F(\theta^*, K) = \frac{1}{K} \sum_{l=0}^{\infty} (2l+1)\, a_l(K)\, P_l(\cos\theta^*) \qquad (2.3)$$

a_l is the partial wave amplitude and is given by

$$a_l(k) = \frac{\eta_l e^{2i\delta_l} - 1}{2i} \qquad (2.4)$$

where η_l is the absorption parameter and δ_l is the phase shift. In the case of scattering of spin 0^- and spin $\frac{1}{2}^+$ particles ($\pi^- p \rightarrow \pi^- p$), we will have spin flip and non-spin flip amplitudes. Hence the differential cross-section given by (2.2) should be written in the case of scattering from unpolarised target as,

$$\left(\frac{d\sigma}{d\Omega}\right) = \left| f(\theta^*, K) \right|^2 + \left| g(\theta^*, K) \right|^2 \qquad (2.5)$$

where $f(\theta^*, K)$ and $g(\theta^*, K)$ are the non-spin flip and spin flip amplitudes respectively and are given by,

$$f(\theta^*, K) = \frac{1}{K} \sum_{l=0}^{\infty} \left\{ (l+1)\, a_{l,l+\frac{1}{2}}(K) + l\, a_{l,l-\frac{1}{2}}(K) \right\} P_l(\mathrm{Cos}\,\theta^*) \qquad (2.6a)$$

and

$$g(\theta^*, K) = \frac{1}{iK} \sum_{l=0}^{\infty} \left\{ a_{l,l+\frac{1}{2}}(K) - a_{l,l-\frac{1}{2}}(K) \right\} P_l^1(\mathrm{Cos}\,\theta^*) \qquad (2.6b)$$

where $P_l(\mathrm{Cos}\,\theta^*)$ and $P_l^1(\mathrm{Cos}\,\theta^*)$ are respectively Legendre polynomial and associated Legendre polynomial of the first kind. Considering the two isospin states $I = \frac{1}{2}$ and $I = 3/2$, and using the convention

	$l = 0$	$l = 1$	$l = 2$	$l = 3$	
$l + \frac{1}{2}$	S_1	P_3	D_5	F_7	
$l - \frac{1}{2}$	0	P_1	D_3	F_5	ete.

we can write $f(\theta^*, K)$ and $g(\theta^*, K)$ respectively as,

$$f(\theta^*,k) = \frac{1}{6ik}\Big[\big(2S_{11} + S_{31}\big) + \big(2P_{11} + 4P_{13} + P_{31} + 2P_{33}\big)\cos\theta^*$$

$$+\big(4D_{13} + 6D_{15} + 2D_{33} + 3D_{35}\big)\big(\tfrac{3}{2}\cos^2\theta^* - \tfrac{1}{2}\big)$$

$$+\big(6F_{15} + 8F_{17} + 3F_{35} + 4F_{37}\big)\big(\tfrac{5}{2}\cos^3\theta^* - \tfrac{3}{2}\cos\theta^*\big) + \cdots\Big]$$

(2.7 a)

and

$$g(\theta^*,k) = -\frac{1}{6k}\Big[\big(P_{33} + 2P_{13} - P_{31} - 2P_{11}\big)\sin\theta^* +$$

$$3\big(D_{35} + 2D_{15} - D_{33} - 2D_{13}\big)\sin\theta^*\cos\theta^*$$

$$+\tfrac{3}{2}\big(F_{37} + 2F_{17} - F_{35} - 2F_{15}\big)\big(5\cos^2\theta^* - 1\big)\sin\theta^* + \cdots\Big]$$

(2.7 b)

where we have used the notation $L_{2I,\,2J}$.

2.2 Elastic scattering differential cross-section near η-threshold.

We can write the π^-p elastic scattering differential cross-section at η-threshold as,

$$\left(\frac{d\sigma}{d\Omega}\right)_{thres} = \left|f(\theta^*,k)\right|^2 + \left|g(\theta^*,k)\right|^2 \tag{2.8}$$

Since η meson is produced from S_{11} wave near threshold, in order to conserve probability, we can write $\left(\frac{d\sigma}{d\Omega}\right)$ above η-threshold as,

Above threshold:

$$\left(\frac{d\sigma}{d\Omega}\right) = \left|\frac{1}{6ik}\Big[\big(2S_{11}' + S_{31}\big) + \big(2P_{11} + 4P_{13} + P_{31} + 2P_{33}\big)\cos\theta^*\right.$$

$$\left. + \cdots\cdots\right|^2 + \left|g(\theta^*,k)\right|^2 \tag{2.9}$$

We have to find out $S_{11}^{\prime}$, in general we can write,

$$S_{11}^{\prime} = \left(\eta_0 - |\Delta\eta_0|\right) e^{2i\delta_0} - 1 \tag{2.10}$$

where η_0 is the absorption parameter, $|\Delta\eta_0|$ is the change in η_0 and δ_0 is the phase shift of the S_{11} wave. Assuming S_{11} wave is elastic at the η-threshold ($\eta_0 = 1$), we can write

$$\begin{aligned} S_{11}^{\prime} &= \left(1 - |\Delta\eta_0|\right) e^{2i\delta_0} - 1 \\ &= \left(e^{2i\delta_0} - 1\right) - |\Delta\eta_0| e^{2i\delta_0} \\ &= S_{11} - |\Delta\eta_0| e^{2i\delta_0} \end{aligned} \tag{2.11}$$

Hence,

$$\left(\frac{d\sigma}{d\Omega}\right) = \left| f(\theta^*, k) - \frac{2}{6ik} |\Delta\eta_0| e^{2i\delta_0} \right|^2 + \left| g(\theta^*, k) \right|^2 \tag{2.12}$$

We can find the value of $|\Delta\eta_0|$ from the conservation of probability as,

$$\begin{aligned} \sigma_{reac} &= \int \left(|\psi_{in}|_{S_{11}}^2 - |\psi_{out}|_{S_{11}} \right) r^2 d\Omega \\ &= \frac{\pi}{K^2} \left(1 - \left| 1 - |\Delta\eta_0| \right|^2 \right) \end{aligned} \tag{2.13}$$

If we restrict ourselves near to threshold, we can neglect terms containing $|\Delta\eta_0|^2$ in the expansion of $\left|1 - |\Delta\eta_0|\right|^2$. Hence we can write finally σ_{reac} as,

$$\sigma_{reac} = \frac{2\pi}{K^2} |\Delta\eta_0| \tag{2.14}$$

Taking into account the isospin factor we have,

$$\sigma_{reac} = \frac{2\pi}{K^2} \cdot \frac{2}{3} |\Delta\eta_0|$$

$$\therefore \; |\Delta\eta_0| = \frac{3K^2}{4\pi} \sigma_{reac} \tag{2.15}$$

For convenience if we denote the c.m. momentum of elastic channel by K at threshold and reaction channel (ηn) by K_1 , we have

$$|\Delta\eta_0| = \frac{3K^2}{4\pi}\sigma_{reac}(K_1) \tag{2.16}$$

Near threshold $\sigma_{reac}(K_1)$ is proportional to K_1 , hence

$$\sigma_{reac}(K_1) = AK_1 \tag{2.17}$$

where A $\simeq$ (21.2 $\pm$ 1.8) μb/(MeV/c) (Binnie et al 1973).
Hence we write $\left(\frac{d\sigma}{d\Omega}\right)$ given by (2.12) as,

$$\left(\frac{d\sigma}{d\Omega}\right) = \left| f(\theta^*,k) - \frac{k}{4\pi i} AK_1 e^{2i\delta_0}\right|^2 + \left|g(\theta^*,k)\right|^2$$

$$= \left| f(\theta^*,k) + \frac{k}{4\pi} AK_1 e^{i(2\delta_0+\pi/2)}\right|^2 + \left|g(\theta^*,k)\right|^2$$

$$= \left|f(\theta^*,k)\right|^2 + \left|g(\theta^*,k)\right|^2 - \frac{k}{2\pi}AK_1\left|f(\theta^*,k)\right| \mathrm{Sin}\left(2\delta_0 - \alpha(\theta^*)\right)$$

$$\therefore \left(\frac{d\sigma}{d\Omega}\right) = \left(\frac{d\sigma}{d\Omega}\right)_{thres} - \frac{k}{2\pi}AK_1\sqrt{\left(\frac{d\sigma}{d\Omega}\right)_{thres} - \left|g(\theta^*,k)\right|^2}\ \mathrm{Sin}\left(2\delta_0 - \alpha(\theta^*)\right) \tag{2.18}$$

where δ_0 is the phase of S_{11} wave and $\alpha(\theta^*)$ the phase of the scattering amplitude $f(\theta^*, K)$. The amplitude of S_{11} wave takes a left hand turn of $\pi/2$ at threshold.

Below threshold:

In order to find the differential cross-section below η-threshold we can make the analytic continuation,

$$\sigma_{reac} = A i |K_1| \tag{2.19}$$

which implies $K_1 = i|K_1|$, the other possibility $K_1 = -i|K_1|$ leads to an exponentially increasing wave below threshold. Hence we can write $\left(\frac{d\sigma}{d\Omega}\right)$ below threshold as,

$$\left(\frac{d\sigma}{d\Omega}\right) = \left| f(\theta^*, \kappa) - \frac{\kappa}{4\pi i} A i |K_1| e^{2i\delta_0} \right|^2 + \left| g(\theta^*, \kappa) \right|^2$$

$$= \left(\frac{d\sigma}{d\Omega}\right)_{thres} - \frac{\kappa}{2\pi} A |K_1| \sqrt{\left(\frac{d\sigma}{d\Omega}\right)_{thres} - |g(\theta^*, \kappa)|^2} \; Cos\left(2\delta_0 - \alpha(\theta^*)\right) \tag{2.20}$$

We can write expressions (2.18) and (2.20) in a combined form as,

$$\left(\frac{d\sigma}{d\Omega}\right) = \left(\frac{d\sigma}{d\Omega}\right)_{thres} - \frac{\kappa}{2\pi} \sqrt{\left(\frac{d\sigma}{d\Omega}\right)_{thres} - |g(\theta^*, \kappa)|^2} \; \sigma_{reac}(|K_1|) \begin{cases} Sin\left(2\delta_0 - \alpha(\theta^*)\right) & \text{above threshold} \\ Cos\left(2\delta_0 - \alpha(\theta^*)\right) & \text{below threshold} \end{cases} \tag{2.21}$$

In deriving the above relation (2.21), in addition to the conservation of probability and analytic continuity we assumed the followings:

(i) η meson is produced practically through S wave or in other words the expansion of powers of K_1 can be stopped at the first term.

(ii) All the other energy dependent quantities which are not influenced by the η-production can be supposed to be slowly varying, and their values can be calculated at the η-threshold, giving a very good approximation.

In order to satisfy the above conditions we have to consider a narrow momentum interval around threshold say 5 ~ 10 MeV/c above and below threshold. The expression (2.21) reduces to the expression obtained by Baz (1958) for spin zero, spin zero particle scattering.

Since η is stable against strong decay, a cusp at the η-threshold is plausible. The shape of the cusp depends in which quadrant $(2\delta_0 - \alpha(\theta^*))$, the relative phase of S_{11} wave and non-spin flip amplitude $f(\theta^*, K)$ lies. The magnitude of the cusp depends on reaction cross-section and the magnitude of contribution of spin-flip cross-section to the differential cross-section. Some possible shapes of cusps occurring in elastic differential cross-sections at η-threshold are shown in Fig. 2.1. If $(2\delta_0 - \alpha(\theta^*))$ is in the first quadrant we have a cusp at the threshold (Fig. 2.1(a)), if $(2\delta_0 - \alpha(\theta^*))$ lies in the third quadrant, the cusp turns into a valley (Fig. 2.1(c)); while if $(2\delta_0 - \alpha(\theta^*))$ is in the second or fourth quadrant, the differential elastic cross-section exhibits a step (Figs. 2.1(b) and 2.1(d)).

From the behaviour of a cusp we can extract the followings :

(i) $\sigma_{reac}(|K_1|)$, for this the measurement of $\pi^- p$ elastic scattering differential cross-section at $\cos\theta^* = -1.0$ is essential. The behaviour of the cusp in the elastic scattering differential cross-section will give directly the value of $\sigma_{reac}(|K_1|)$ since $|g(\theta^*, K)|^2 \to 0$ in this region.

(ii) Once the value of $\sigma_{reac}(|K_1|)$ is known from the behaviour of the cusp or from some independent production cross-section measurements, then the spin-flip cross-section $|g(\theta^*, K)|^2$ and non-spin flip cross-section $|f(\theta^*, K)|^2$ in different c. m. scattering angles can be extracted from the behaviour of the cusp in those regions.

(iii) Cusp behaviour will give direct information of the relative phases of S_{11} and $f(\theta^*, K)$.

(iv) The phases of S_{11} and $f(\theta^*, K)$ waves can be determined from

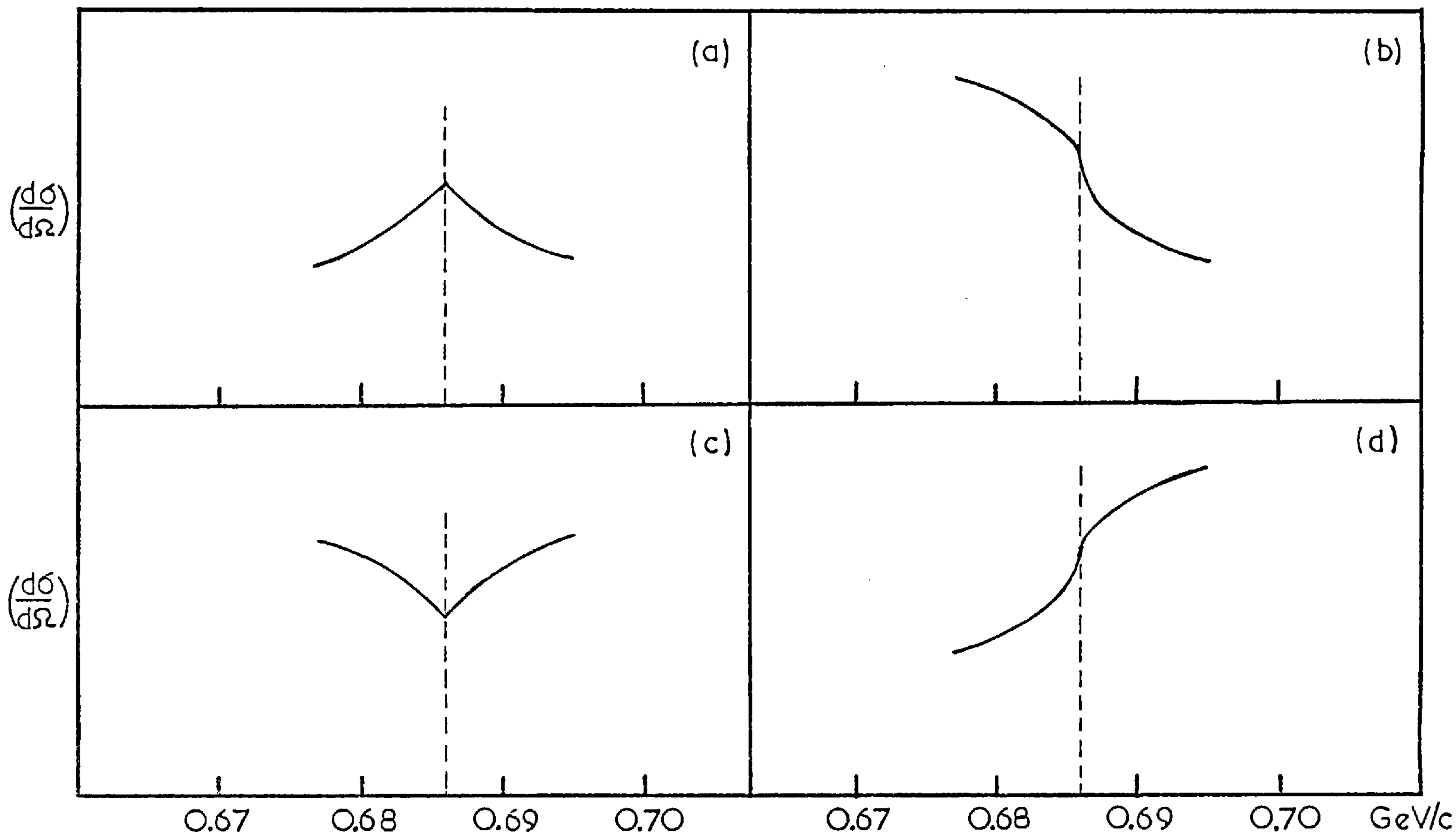

FIG. 2.1 Some possible shapes of cusps occuring in cross-sections at η - threshold .

the values of $(2\delta_0 - \alpha(\theta^*))$ and $|f(\theta^*, k)|$ which are known as functions of Cos θ^* at the η-threshold.

Wigner (1948) first pointed out the fact that in physical quantities e.g. cross-section, polarization etc. for a given reaction, one has to expect cusps in the energy behaviour at the threshold energies for the competing channels. Theoretical contributions have been given by Adair (1958), Baz' and Okun' (1959), and Nauenberg and Pais (1961). Pais (1961) discussed in detail the possibility of determining the relative Σ-Λ parity by the method of cusps.

An experimental study of $\pi^- p \rightarrow \Lambda + K^0$ has been made in the region of ΣK threshold by Eisler et al (1961) and Wolf et al (1961). Their result was not simple. The total cross-section did not show a cusp. Upto F waves were essential to fit the differential cross-section. As the momentum crosses the thresholds for $\Sigma^- K^+$ and $\Sigma^0 K^0$, the angular distribution does change rapidly. Because of the Minami ambiguity it was not clearly established which of the coefficients in the Legendre polynomial fit have cusp behaviour.

For the experimental observation of cusps, one needs a high experimental accuracy on data used and a very good beam momentum resolution ($\sim$ 0.10%), a thin target or an evaluation of the interaction point in the liquid hydrogen target. In other words one requires a precision experiment in high energy physics.

3. Apparatus (Beam line)

A very high resolution beam line was set up at the π8A beam line of the Rutherford Laboratory. A momentum resolution of approximately 0.025 % was achieved using multi-wire proportional chambers in the beam line.

3.1 Beam

Fig 3.1 shows the layout of the beam line of π8A. Pions were produced by causing the Nimrod proton beam to strike an external copper target. A beam was accepted, momentum analysed and focussed onto the liquid hydrogen target 60 mm. in diameter and 200 mm. in length, by a system of dipole and quadrupole magnets. The beam layout was designed by Dr. D. M. Binnie.

The quadrupole magnets Q603 and Q422 focus in the vertical and horizontal plane respectively, at the first focus F1. The bending angle of the dipole magnet M213 is 19.5°. A rough momentum selection is made in the second stage, where Q418 and Q417 focus the beam 1.495 meters downstream of G and 54.3 cm. upstream of G in the vertical and the horizontal plane respectively. (Q509 was not used for beam momentum below 1.500 GeV/c). The bending angle of the M118 magnet is 13.38°. A high resolution momentum analysis is performed in the third stage. Two spectrometer bending magnets M201 and M202 each of bending angle 16.3°, and quadrupole magnets, Q113 focussing vertically and Q402 focussing horizontally form an image at the liquid hydrogen target. The dimensions of the beam at this focus are $\pm$ 14 mm horizontally and $\pm$ 15 mm vertically for a 10 cm copper target (X_3). Two sets of hodoscope counters are located at G and H , which are conjugate foci of the spectrometer with unit horizontal magnification. The overall dispersion produced at H is 40.5 mm per 1 % momentum variation. The G hodoscope consists of eight fingers of scintillator each of width 7.5 mm and the H hodoscope has six fingers of

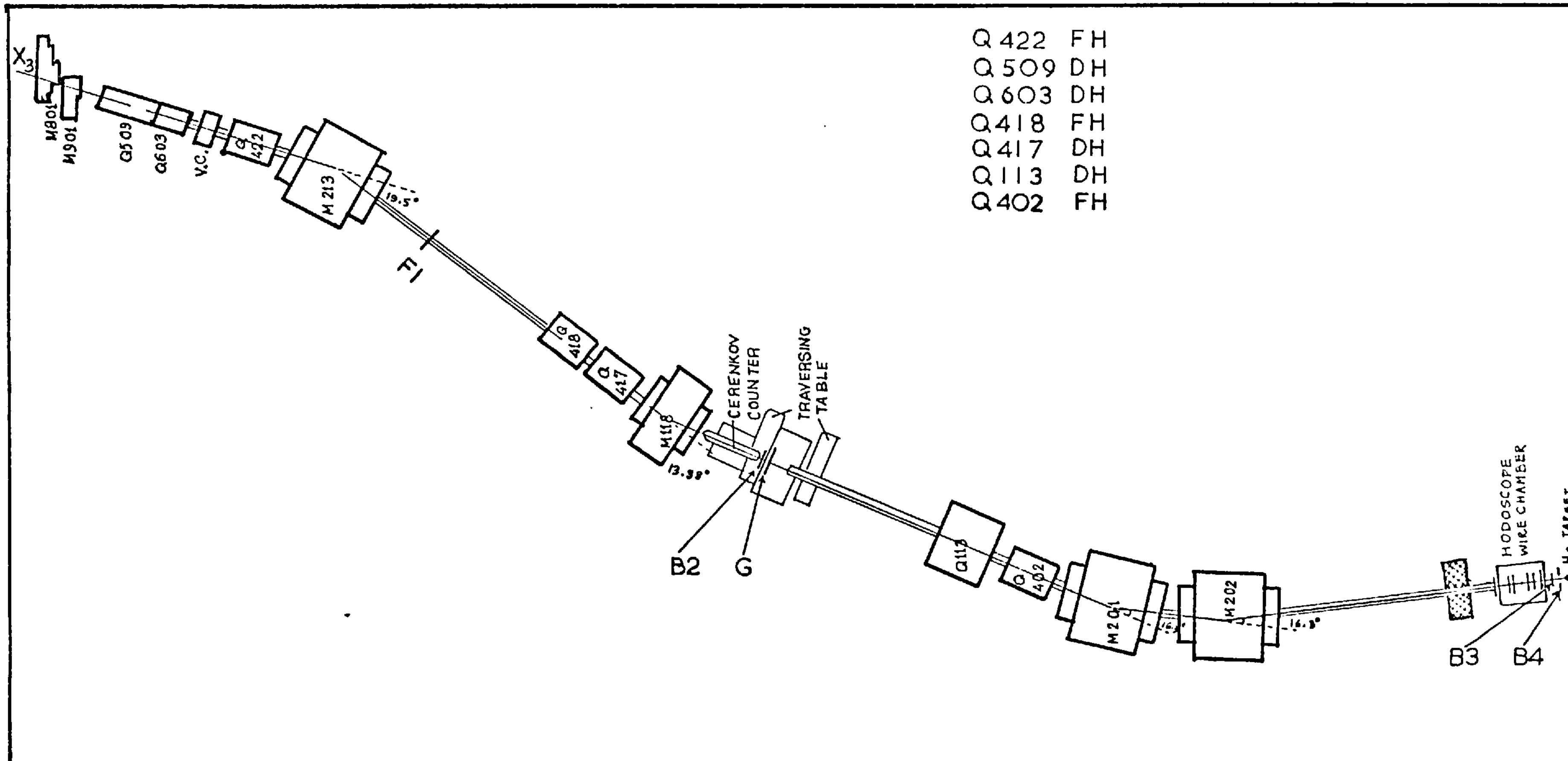

FIG. 3.1 PLAN OF π8A BEAM LINE.

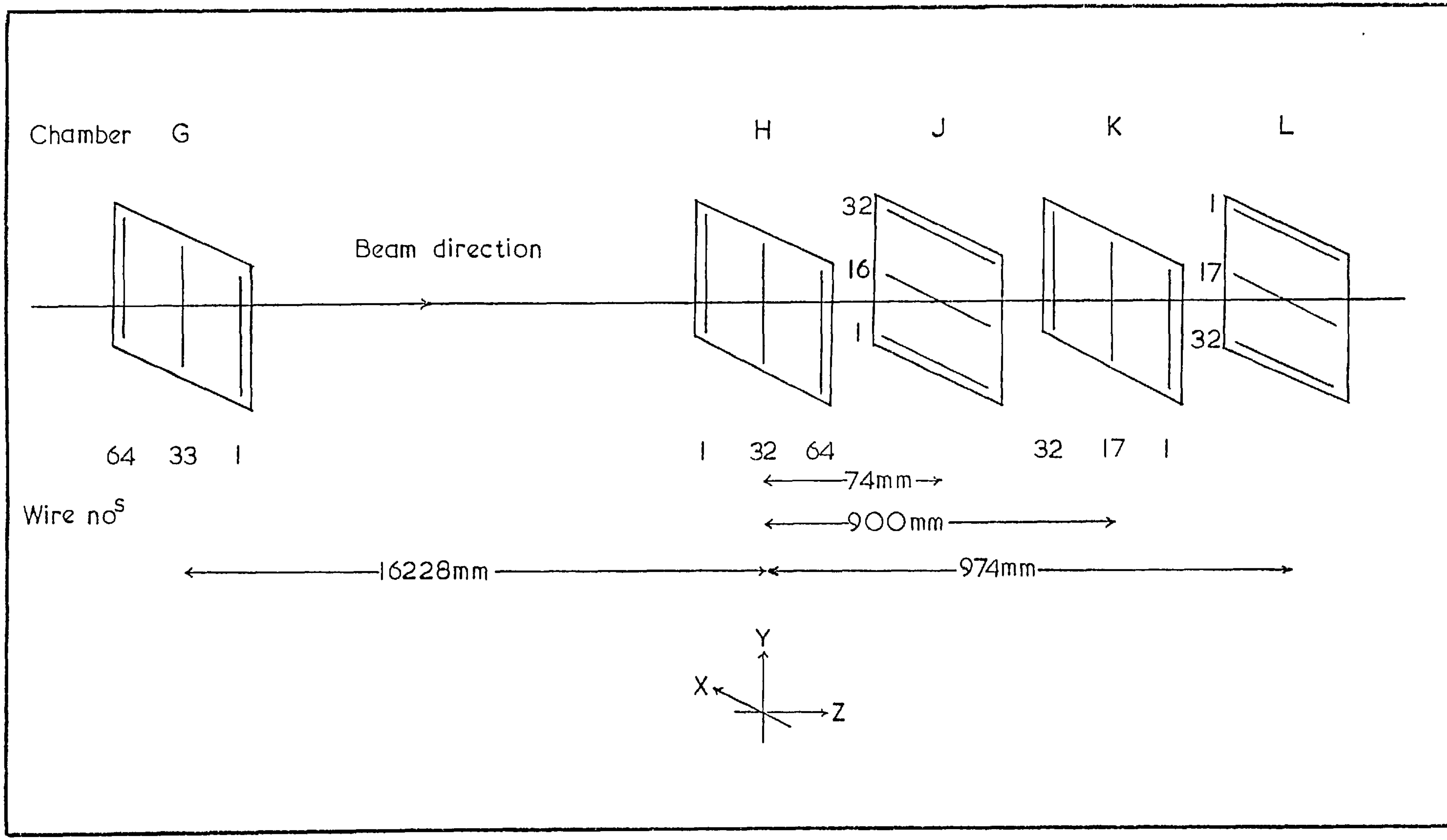

FIG. 3.2 Wire chamber arrangement in π8A beam line.

width 7.5 mm. Four momentum bins are accepted for ΣP_{π}, the total number of incident pions. Five multiproportional wire chambers (Fig 3.2) G , H (of 1 mm wire spacing), J , K and L (2 mm wire spacing) are used for accurate momentum and angle determination. The G wire chamber is located near the G hodoscope and the remaining chambers are near the H hodoscope. A gas Čerenkov counter , C , filled with freon is used to veto electrons in the beam. The only non-negligible contamination remaining in the negative pions is from muons. Three scintillation counters B2 , B3 and B4 are used for triggering the beam logic.

Preliminary estimates of the required currents were made, using the Rutherford Laboratory programme ' TRAMP '. The IPSO FACTO programme was used for calculating the beam profile and acceptance. The currents in the spectrometer magnets M201 , M202 , Q113 and Q402 were determined in the floating wire measurements. The currents for the second stage beam line magnets were also roughly determined by a floating wire technique. The currents of the remaining magnets in the beam line were determined in beam tuning runs.

3.2 Floating wire measurement

In order to determine the relationship between M201 , M202 fields and particle momentum , one requires to calibrate with particles of known momentum. Similarly one requires such particles to find the correct currents for Q113 and Q402 in order to achieve vertical and horizontal focussing at the proper plane. The floating wire method provides the equivalent of particles of known momentum.

A charged particle moving with velocity $\vec{v}$ in a magnetic field $\vec{B}$ experiences a force

$$\vec{F} = e \left(\vec{v} \times \vec{B} \right) \qquad (3.1)$$

The change in the direction $d\theta$ in an element of length dl is given by

$$\frac{d\theta}{dl} = \frac{e}{p} \hat{n} \times \vec{B} \qquad (3.2)$$

where $\hat{n}$ is the direction vector , p the momentum and e is the charge.

For a wire carrying a current i , under a tension T , we have

$$\frac{d\theta}{dl} = - \frac{i}{T} \hat{n} \times \vec{B} \qquad (3.3)$$

Therefore the equilibrium configuration of the wire under tension and magnetic force will be identical with the trajectory of the charged particle whose momentum obeys the relation ,

$$\frac{e}{p} = - \frac{i}{T} \qquad (3.4)$$

for e equal to the electron charge , we have in practical units

$$p = 2 \cdot 94144 \; T/I \qquad (3.5)$$

where p is the momentum of the particle in MeV/c , T in grams and I in amperes. A weight of 200 gm was used throughout the floating wire measurements. The numerical constant g has been obtained from the value of g at Teddington with a small correction ($\sim$ 13 ppm) for the altitude of the Rutherford Laboratory.

The set up of the floating wire measurement is shown in Fig. 3.3. Reference points on the beam axis , in the form of fine holes in perspex

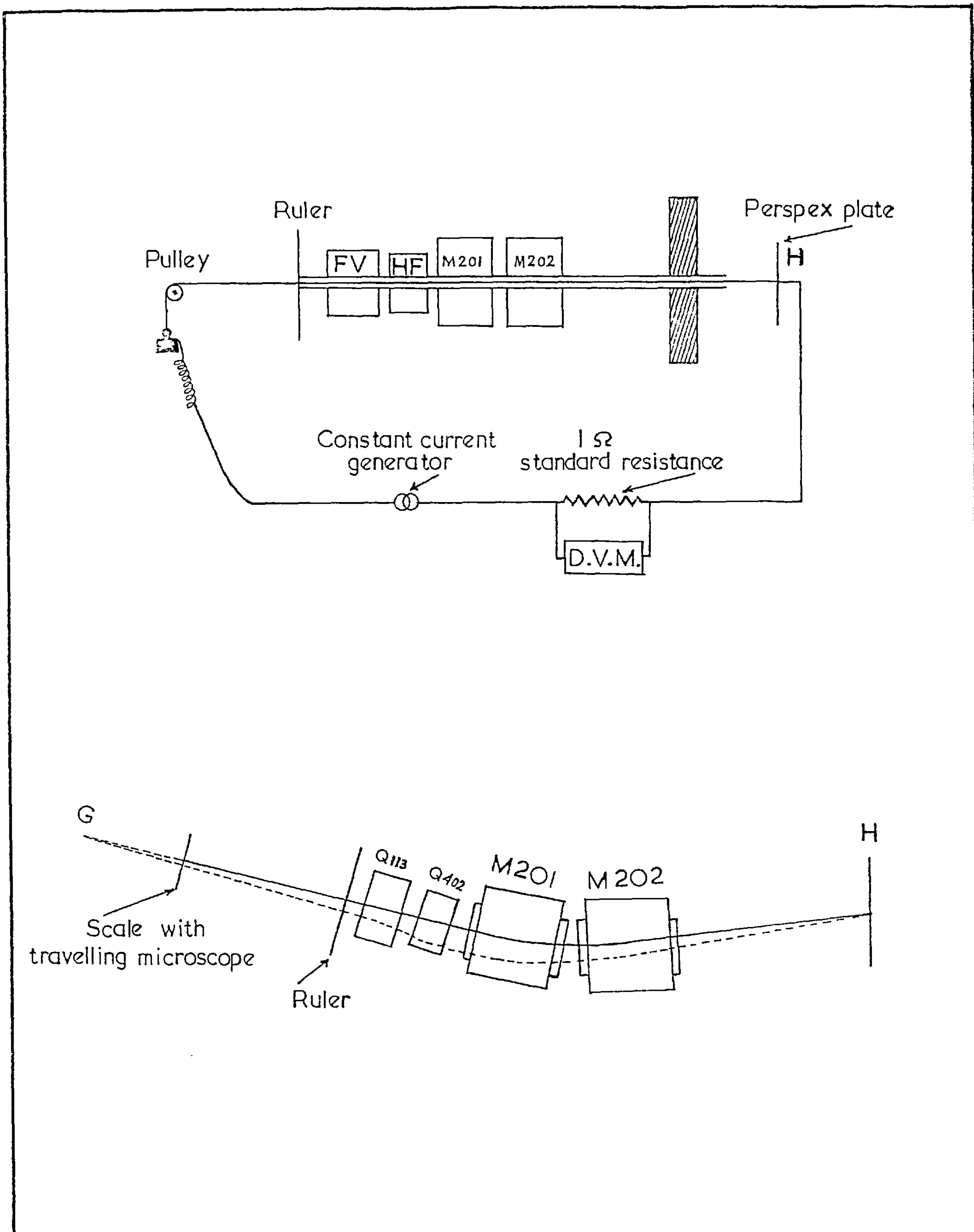

FIG. 3.3 Plan layout of floating wire measurement.
(Not to scale)

plates were provided at G and H planes by Imperial College technicians. When the magnet currents are set properly, the point H should be the image of point G, so all trajectories through one would pass through the other. A light copper wire was fixed at a point in the H plane and run through the beam pipe through the four magnets and over the air bearing pulley (Binnie et al 1970) which was placed 106cm downstream of G plane. The electric circuit was completed through a constant current generator and the wire current was determined by a Hewellet Packard DVM from the voltage developed across the standard 1 ohm resistance.

The wire current (equivalent momentum) and approximate the magnet currents were set and the position of the wire was observed at the pulley by a travelling microscope, and near Q413 by eye. This was done for a series of pulley positions and the trajectories were extrapolated to the point of intersection of the rays to give the position of the image of H.

In order to minimise the hysteresis effects in quadrupoles they were set to the desired currents by making a series of occursion below and above the final current. This was also done for setting the quadrupole currents in taking data.

The procedure followed in each momentum of the floating wire measurements is given below:

First, set the quadrupole currents to the values given by TRAMP and also the currents in M201 and M202 to give the approximate field strength. Horizontal and vertical scans were made to try to get the bending angle right, then to try to get the horizontal and vertical foci in the right positions and then finally to check the bending angle. The adjustment of the quadrupoles currents were made by using the approximate relations,

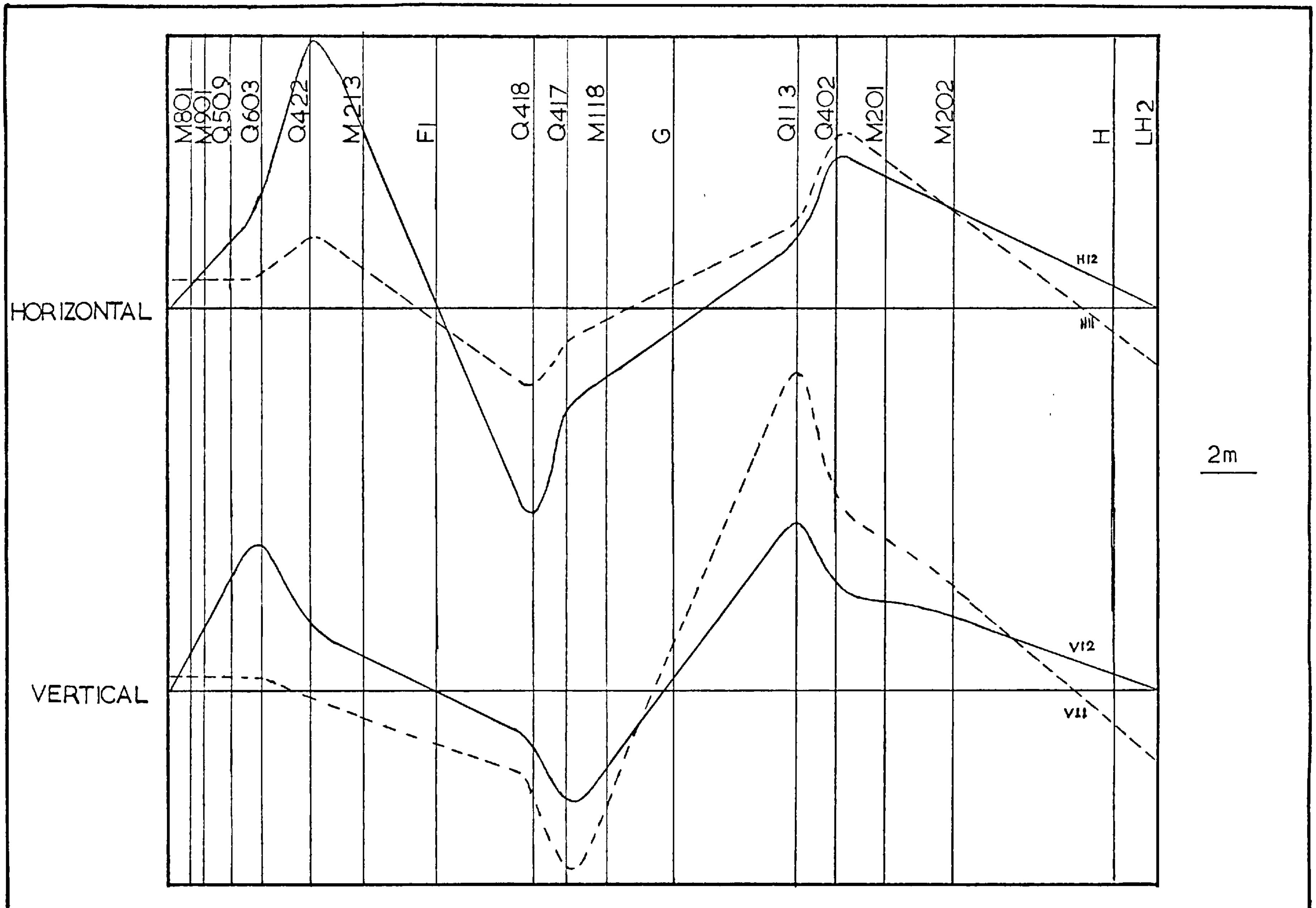
M801
M901
Q509
Q603
Q422
M213
F1
Q418
Q417
M118
G
Q113
Q402
M201
M202
H
LH2
HORIZONTAL
VERTICAL
H12
H11
V12
V11
2m

FIG. 3.4

$$\delta Q_{113}\ (\%) = \frac{\delta F_V}{16} + \frac{\delta F_H}{105} \qquad (3.6\ a)$$

$$\delta Q_{402}\ (\%) = \frac{\delta F_H}{40} + \frac{\delta F_V}{35} \qquad (3.6\ b)$$

which were derived from a number of runs of TRAMP changing the currents in quadrupoles a few percent. δF_V and δF_H are the changes in vertical and horizontal positions, in centimetres, to be made to adjust to the correct focussing positions. A positive sign convention was taken for a focus downstream of the G plane and negative for upstream positions. About four or five scans were required to get the final horizontal and vertical focuses in correct positions.

In this way, the required currents for quadrupoles Q113, Q402 and NMR frequencies for the bending magnets were obtained for a series of momenta 0.700 GeV/c, 1.100 GeV/c and 1.500 GeV/c. All the currents and NMR frequencies for other momenta were found by a quadratic interpolation method from the values of currents and NMR frequencies where the floating wire measurements were carried out. The stabilities of the bending magnets were better than 1 part in 10^4 and that of the quadrupoles 1 part in 10^3. Fig. 3.4 shows the trajectory of a particle in the π 8A beam line.

3.3 The liquid hydrogen target

The liquid hydrogen target was supplied by the Rutherford Laboratory. The liquid hydrogen is contained in a cylindrical flask 60mm in diameter and 200mm in length, with its axis parallel to the beam. An outer casing of aluminium provided a vacuum for heat insulation. By means of a constant pressure device the effective density of the boiling hydrogen was maintained at 0.07 gm/cc. The design of π 8A liquid hydrogen target is shown in Fig. 3.5.

At ~ 0.700 GeV/c the momentum loss of a π^- in the liquid hydrogen target is ~ 0.0029 MeV/c/mm. The momentum of the incident pions was corrected from the known interaction point for the momentum lost in the target.

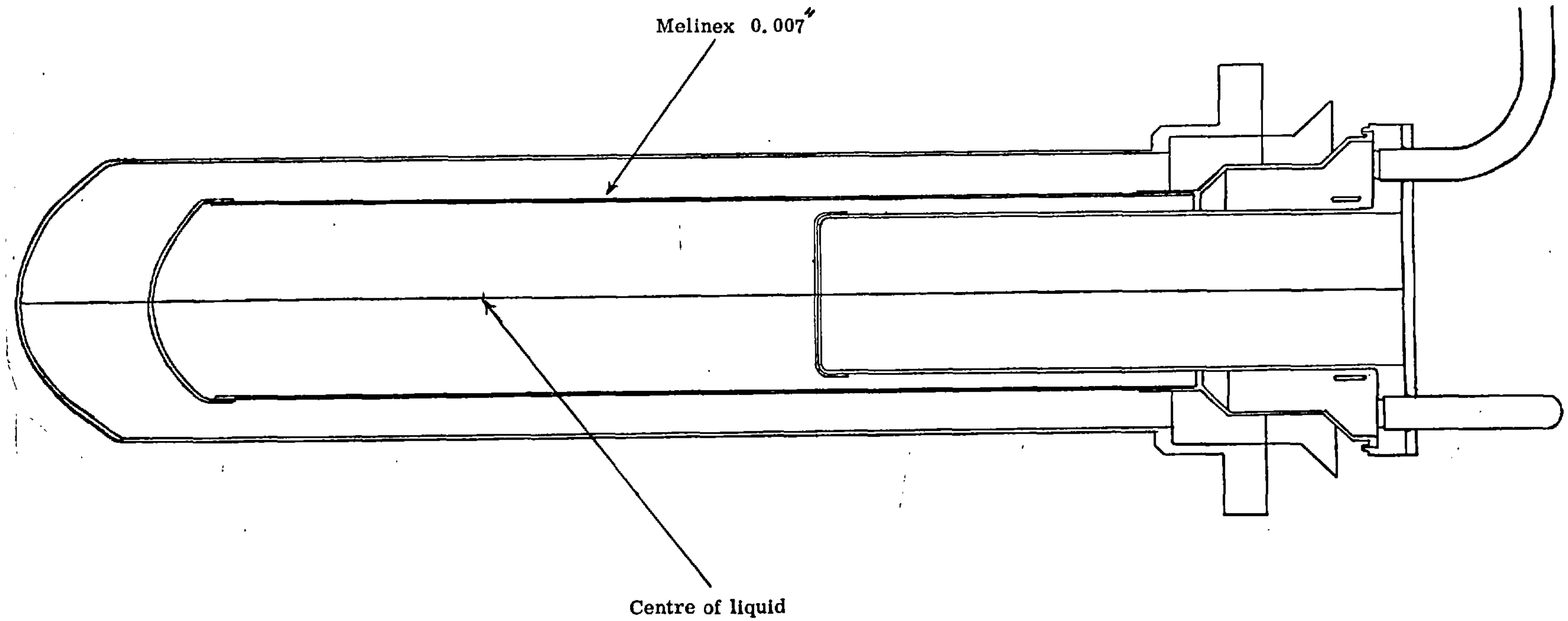

FIG. 3.5 π8 A Liquid Hydrogen Target.

4. Apparatus (Detecting system)

Drift chambers surrounding the liquid hydrogen target were used to detect the scattered π^- and p . Fig. 4.1 shows the arrangement of drift chambers in π 8A beam line around the liquid hydrogen target.

4.1 Drift chamber

The drift chambers in π 8A were required for the high resolution and high statistics study of $\pi^- p$ elastic scattering near the inelastic thresholds of ηn , ωn , $K\Lambda$, $K\Sigma$ and $X^0 n$ ($X^0 = \eta'$), in order to throw light on the production mechanisms of ωn and $X^0 n$ which show peculiarly behaved production cross-sections near threshold (Binnie et al 1973). The elastic scattering studies near the ηn , $K\Lambda$ and $K\Sigma$ thresholds were searches for cusps. It was necessary to recognise the elasticly scattered particles and to get the interaction point in the liquid hydrogen target for the accurate momentum determination. A further need for the drift chambers was in the study of the X^0 width in $\pi^- p \rightarrow X^0 n$, detecting one of the charged decay products of the X^0 in the drift chambers and the neutron in neutron counters. This experiment could give an upper limit of the X^0 width of $\sim$ 0.35 MeV.

4.2 Mechanism of drift chamber

In a drift chamber the electrons liberated in a gas medium by ionizing collisions are moved away by electric field from their initial position to a well defined position where they are detected. The accurate measurement of the time interval between the production and detection gives the position where the charged particle passed through the drift chamber. Spatial accuracies $\sim$ 100 μm and timing accuracies $\sim$ 5 nsec can be obtained without too much complication (Charpak 1974).

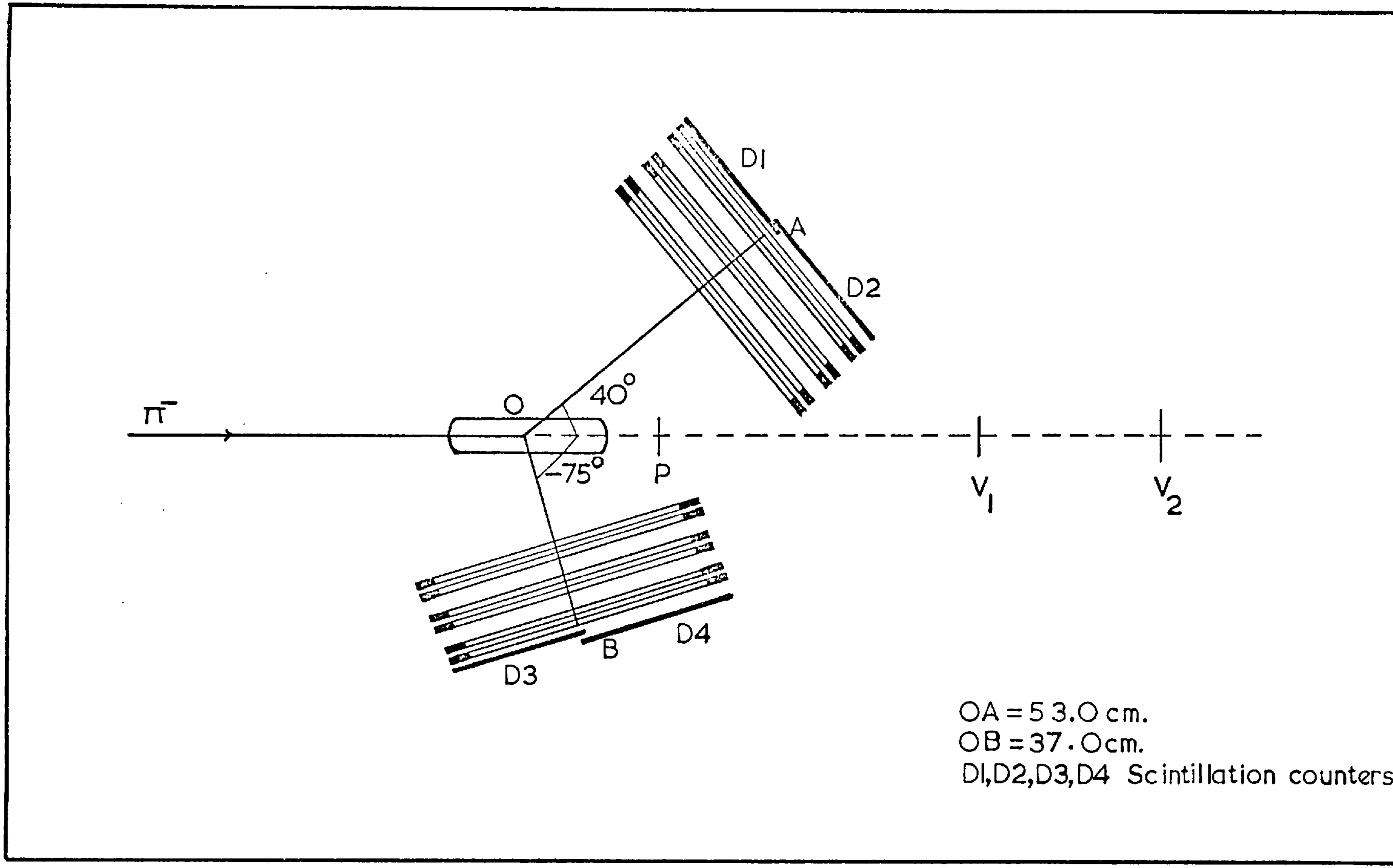

FIG. 4.1 Schematic arrangement of drift chambers around the liquid hydrogen target (not to scale).

The primary electrons liberated by ionizing particles have a few microns range at most at NTP in most of the gases. Each primary electron liberates ~ 2 or 3 secondary electrons before being stopped, and secondary electrons move towards the signal wire (Fig. 4.2). The accuracy of the measurement of the trajectory depends on the range of primary electrons in addition to other factors e.g. electric field, gas mixture etc. So long as we are interested in accuracies greater than 100μm, one does not have to worry about the initial track thickness which appears as infinitely small. The drift velocity varies widely with the composition of the gas mixture and its nature. In most of the cases the drift velocity reaches a nearly constant value with electric field (Charpak 1974) Fig. 4.3. In the measurement of the position of a particle with a drift chamber from the time of drift of the electrons to the sense wire one has to find gas mixtures where the velocity is independent of electric field unless the measurements are restricted to a region of constant field.

4.3 Diffusion without electric field

The basic laws of interdiffusion of two gases are applicable to electrons also in the absence of electric fields.

If N_o is the number of electrons at r = 0 and t = 0, then the distribution of electrons under the influence of diffusion is given by

$$N_x = \left(N_o / \sqrt{\pi D t} \right) exp \left(-x^2 / 4Dt \right) dx \qquad (4.1)$$

The square root of the average squared displacement along an axis is,

$$\sigma = \sqrt{\overline{x^2}} = \sqrt{2Dt} \qquad (4.2)$$

where the coefficient of diffusion D is a function of gas density, mass, pressure and temperature. The kinetic theory gives,

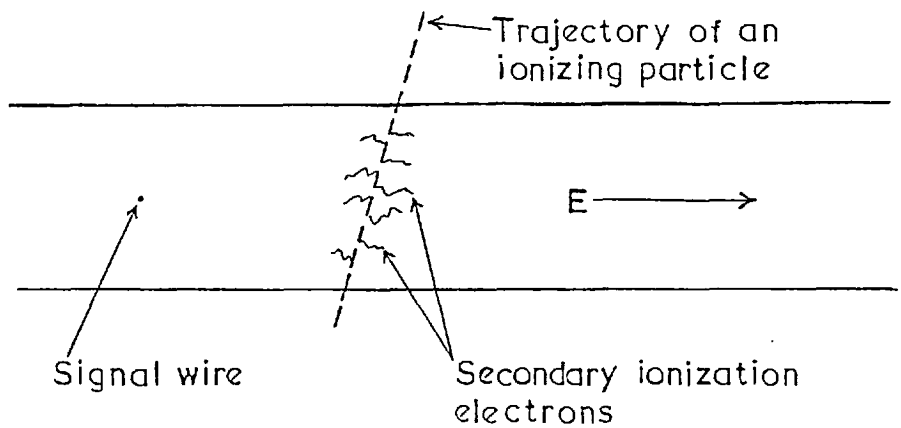
Trajectory of an ionizing particle
E
Signal wire
Secondary ionization electrons

FIG. 4.2

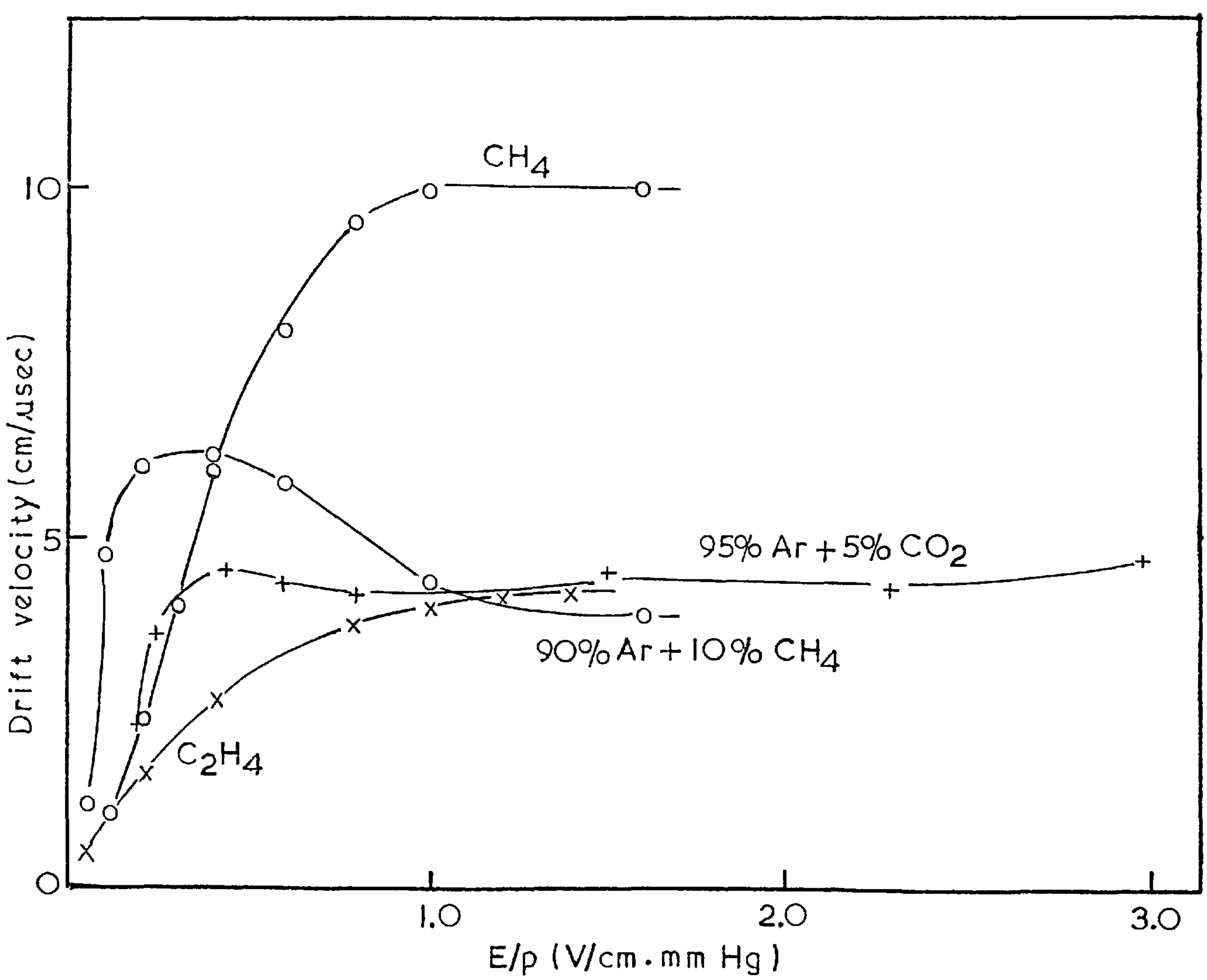
CH4
95% Ar + 5% CO2
90% Ar + 10% CH4
C2H4
Drift velocity (cm/μsec)
E/p (V/cm.mm Hg)
10
5
0
1.0
2.0
3.0

FIG. 4.3

$$D \simeq \frac{0 \cdot 815\ v . l}{3} \sqrt{\frac{m+M}{M}} \qquad (4.3)$$

where l is the mean free path and $v = \langle c^2 \rangle^{1/2}$ is the average velocity of the electrons.

4.4 Diffusion in electric field

Inspite of the fact that electrons travelled many mean free path for every centimetre of advance in electric field, the electrons experience the same average advance per sec and hence drift speeds are very sharp.

The drift velocity is defined by,

$$W = \langle C_x \rangle = \int C_x\ F(r, \bar{c}, t)\ d\bar{c} \qquad (4.4)$$

where F (r, $\bar{c}$, t) is the velocity distribution of electrons at point r and at time t. One usually defines the mobility (μ_0) at 273°K and 76 cm of Hg as

$$\mu_0 = \frac{T_0}{T} \cdot \frac{p}{p_0}\ \mu \qquad (4.5)$$

where μ is the drift speed divided by electric field.

Because of the considerable ratio of the masses of the molecules to electrons, electrons usually do not exchange kinetic energy with gas molecules and hence in electric field the electrons have a temperature much higher than the gas temperature.

The drift velocity w is given by the following expression

$$w = 0 \cdot 815\ \frac{eE}{m}\ \frac{l}{v} \qquad (4.6)$$

Hence, we have

$$\frac{D}{\mu} = \frac{kT_e}{e} \qquad (4.7)$$

where T_e is the electron temperature defined by

$$\frac{3}{2} K T_e = \frac{1}{2} m v^2 \tag{4.8}$$

One usually defines the characteristic energy $\mathcal{E}_K$ as

$$\mathcal{E}_K = \frac{eD}{\mu} \tag{4.9}$$

The characteristic energy ($\mathcal{E}_K$) is of the order of 1 eV at 1 KV/cm at NTP which corresponds to an average electron velocity of 10^8 cm/sec, which is about 20 to 100 times greater than the drift velocity at this field.

For optimum condition one has to minimize $\sigma_x = \sqrt{2Dt}$. We have after 1 cm of drift $\sigma_x = \sqrt{2\mathcal{E}_K/eE}$. σ_x is constant if $\mathcal{E}_K$ is proportional to E, so we have to work in condition of low $\mathcal{E}_K$. But one has to see favourable condition so that the drift voltage to be on plateau may not be very high when one adds a gas mixture in order to bring $\mathcal{E}_K$ low.

4.5 Different types of drift chambers

Different types of drift chambers had been constructed and tested by various groups.

(a) CERN chamber

A multiwire drift chamber with an adjustable electric field has been extensively studied at CERN by Charpak et al (1973, 1974). Fig. 4.4 shows an element of a large chamber with the central plane having anode sense wires alternating with field wires. The chamber is 0.6 cm thick. The electric field is produced by enveloping cathode planes of parallel equidistant wires at rising negative potential. The cathode planes are made of 100 μm diameter wires, 2 mm apart. The thick cathode wires at a potential equal to the

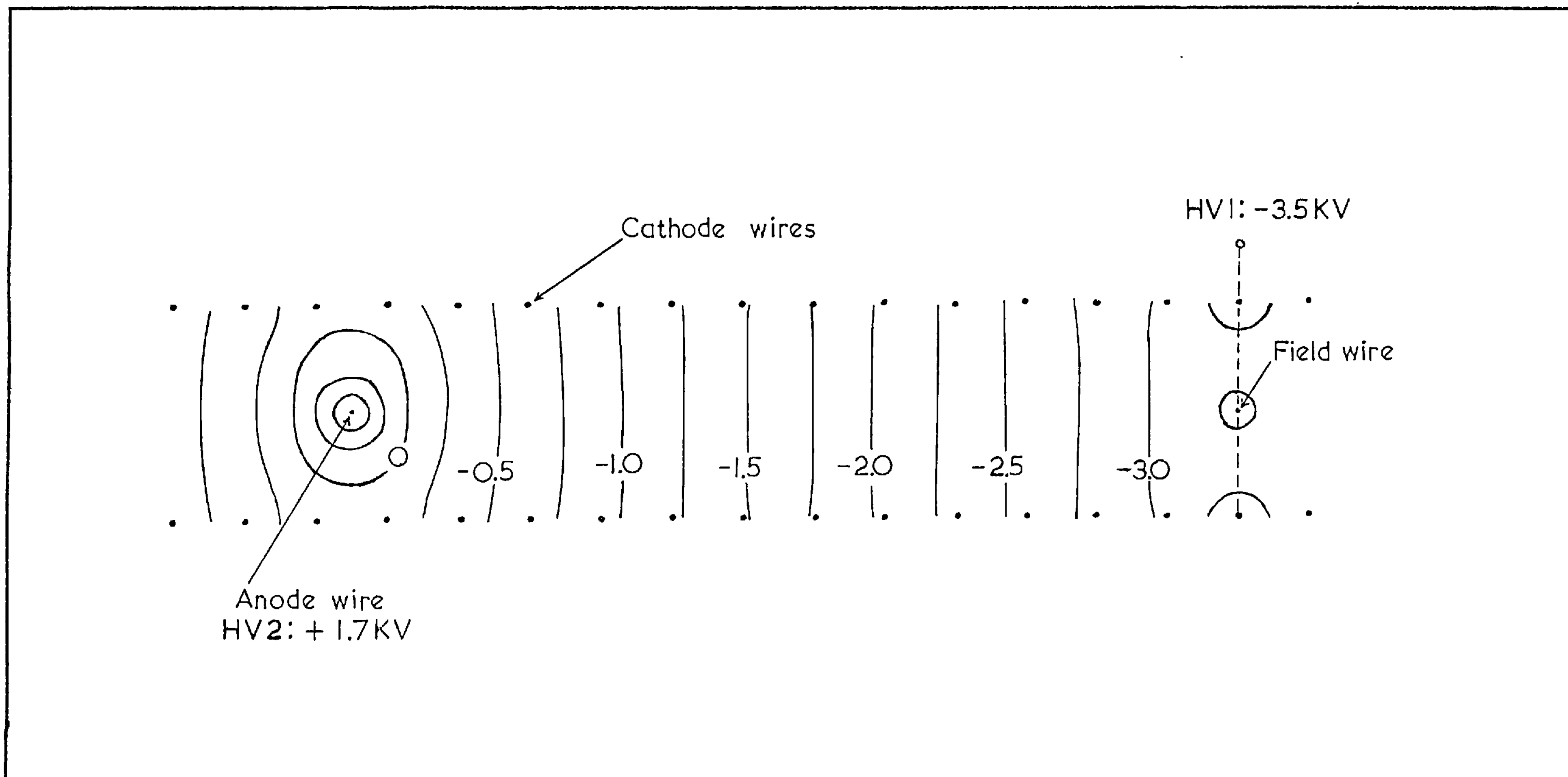

HV1: -3.5KV
Cathode wires
Field wire
-0.5
-1.0
-1.5
-2.0
-2.5
-3.0
Anode wire
HV2: + 1.7KV

FIG. 4.4

maximum cathode potential are mounted symmetrically around the anode wires between the cathode planes 50 mm apart, in order to help in keeping a sharp separation between the adjacent drift space. The primary electrons produced by charged particles in the gas are moved towards the anode wire (20 μm diameter), are amplified and detected. In a typical operation HV1 = - 3.5 KV and HV2 = 1.7 KV.

Though operating adjustable electric field drift chamber with independent drift and anodic potential has a lot of salient features, the electric field in such chamber is far from being constant. An accuracy of 100 μm can be achieved by operating the chamber where the drift velocities are saturated for the gas composition of 75% Ar, 23% isobutane and 2% methylal. In addition however the following characteristics are observed (Charpak 1974).

(i) The space time curve is extremely linear for tracks orthogonal to the chamber planes.

(ii) With suitable gas mixture the drift velocity is very stable against small changes of temperature, gas mixture and drift field.

(iii) At large angle of incidence ($\gtrsim 20^{o}$) the response is a combination of two linear responses, which are independent of position and can be corrected by simple formula.

(b) Saclay chamber

A double chamber with long drift paths (50 mm) has been developed by Saclay group (Saudinos et al 1973). A high tension - 45 KV creates a field $\sim$ 820 V/cm down in the drift region and drifting electrons are detected at the anodes of proportional chambers which are maintained between 0 and

700 V. Pure methane was used as a filling gas which gives a drift speed of $\sim$ 9.7 cm/μsec.

(c) Harvard chamber

Very large drift chambers with 3.6 m X 3.6 m sensitive area have been built by the Harvard group (Cheng et al 1974). With thirtyfour sensing wires a position determination of 0.35 mm was obtained by the use of redundant planes. The chamber module is made from a square frame 5 cm thick with 1 mm metallic sheet on both sides in order to give mechanical support. The central plane is composed of alternate field and sense wires separated by 5 cm, which leads to 35 sense wires for 3.6 m span. Gold plated 100μm molybdenum field and sense wires were used. Operating voltages were + 6 KV on the sense wire, and - 1 to - 2.5 KV on field wires. Ethylene was used as the basic operating gas with some portion of argon $\sim$20% was added to reduce the working voltage. Three modules sandwiched each other at 60^{o} with respect to the other was used to remove the left and right ambiguity and also provides excellent time and spatial resolution.

(d) Heidelberg chamber

A system of large multiwire drift chambers ($\sim$1 m^2) had been designed at Heidelberg (Walenta 1973). Fig. 4.5 shows the principle of multiwire drift chamber. The volume between the cathode planes C (- 1.80 KV) was divided into separate drift spaces by potential wire P (- 2.2 KV) and anode wire pairs A_i , A_{i+1} (earthed). The drift time of ionization electrons from the track to the counting wire A_i and the address of the counting wire determine the location of the track. To overcome the left right ambiguity, two closely spaced counting wires A_i , A_{i+1} were used. Though the counting wire pair is in stable electrostatic equilibrium, the individual wires of each pair repel each other. In order to compensate the forces electrostatically a further potential wire (P') was placed between the counting wires. (Fig. 4.6) The potential of P' is adjusted such that the repelling force between the wires A_i and A_{i+1} is not completely compensated.

Though the field inside the drift chamber is inhomogeneous, the linearity of drift time and drift length can be achieved by using suitable counting gas. By using a mixture of 84% argon, 9% methane and 7% iso-butane they got a nearly linear time distance relationship. In drift chambers using two closely placed counting wires (A_i , A_{i+1}) quenching is very important, otherwise avalanch in one wire will propagate to the other counting wire. Large amounts of quenching agents e.g. isobutane imply higher operating voltages. In general it is desirable to decrease the iso-butane content to lower the operating voltage, but 7% was the limit which gave satisfactory results.

4.6 Left and right ambiguities and position measurement

(a) Modules stacked

Different varieties of combinations of drift chambers have been tried for the left right ambiguity and position (x, y) measurement. It is impossible to distinguish left and right of the sense wire in a multiwire drift chamber type (Fig. 4.4). The method adopted by Heidelberg group is to employ two closely placed sense wire with an intermediate potential wire (Fig. 4.6), but if the tracks pass between any pair of sense wire then it leads to difficulties. The method suggested by Charpak (1974) is the use of stack of three chambers with parallel wires so displaced that the central one has the wire displaced by a half wire spacing with respect to the other two. Harvard group used three multiwire chambers each oriented at 60° with respect to others, which is good for removing multiparticle ambiguities as well.

Another scheme is the use of four planes, a pair of two module systems

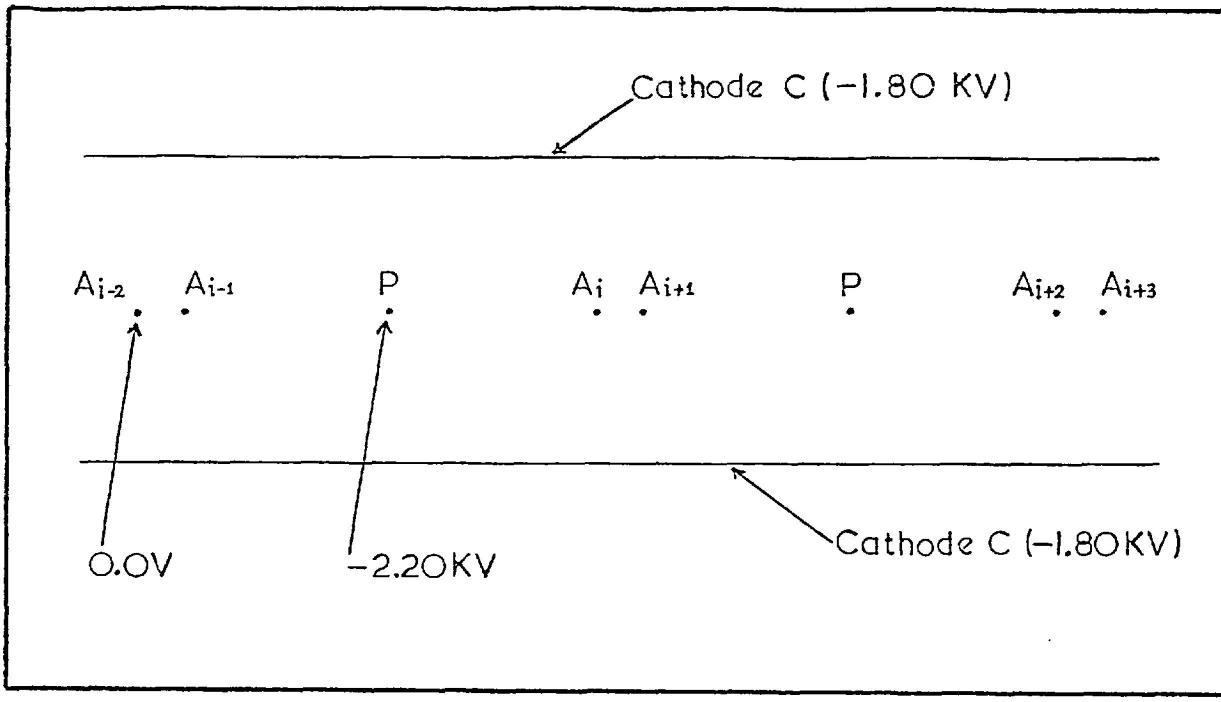

Cathode C (−1.80 KV)
A_{i-2}
A_{i-1}
P
A_i
A_{i+1}
P
A_{i+2}
A_{i+3}
Cathode C (−1.80KV)
0.0V
−2.20KV

FIG. 4.5

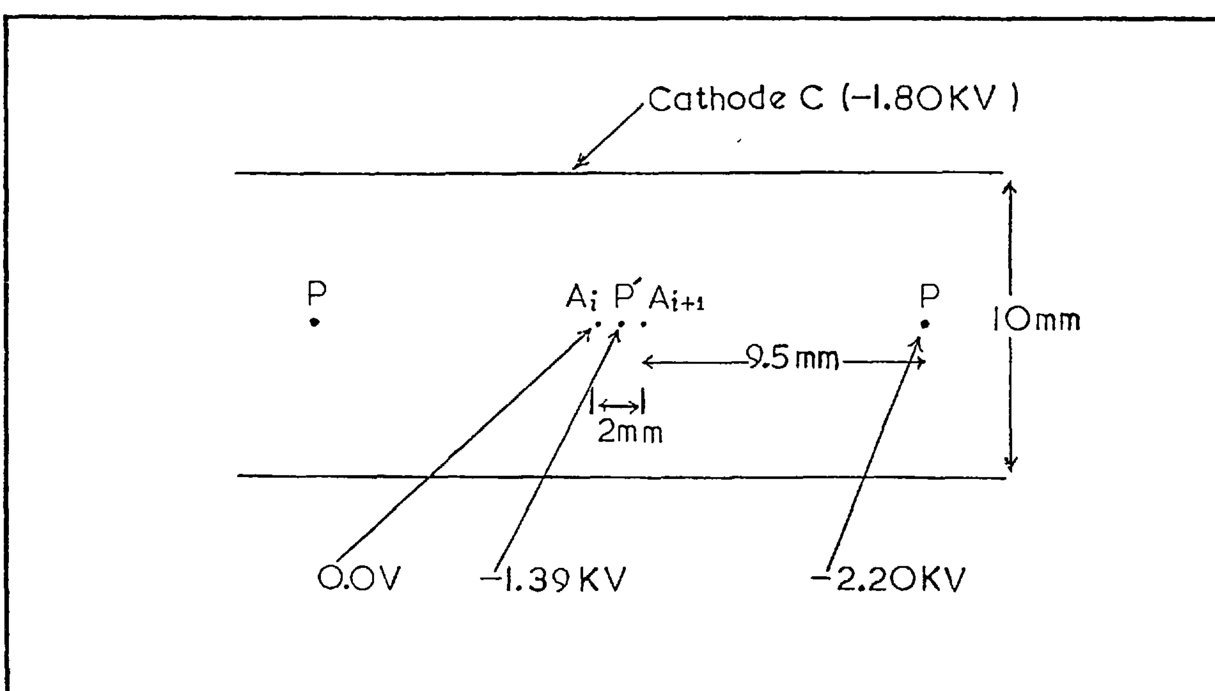

Cathode C (−1.80KV)
P
A_i P′ A_{i+1}
P
9.5 mm
10mm
2mm
0.0V
−1.39 KV
−2.20KV

FIG. 4.6

sandwiched so that the wires run in the sequence x-y-x-y. Parallel sense wires in different planes are displaced by half a cell. A knowledge of four independent drift times not only removes the ambiguity but also determine the angular direction of the particle.

(b) Current division

The determination of co-ordinates from the same signal wire by the method of current division has been investigated in the case of multiwire proportional chambers by Foeth et al (1973). The natural sharing of currents flowing on two sides of the signal wire where the avalanch is produced is used to locate the position of the particle.

If an avalanch is produced on the wire and if i_L and i_R, where $i_L + i_R = i_o$, are the currents flowing through the left and the right paths via the amplifier (Fig. 4.7), then we have

$$X_L = \frac{i_R}{i_R + i_L} L \quad ; \quad X_R = \frac{i_L}{i_R + i_L} L \qquad (4.10)$$

The sharing of current i_L and i_R is inversely proportional to the two resistive paths and directly related to X_R and X_L, where $X_R + X_L = L$, the length of the wire. Using a gas mixture of argon and iso-butane of approximately equal proportion Foeth et al (1973) obtained a good linearity of response in 10 μm gold plated tungsten wire of multiwire proportional chamber with position determination accuracy upto 6 mm in 11 X 11 cm^2 chamber.

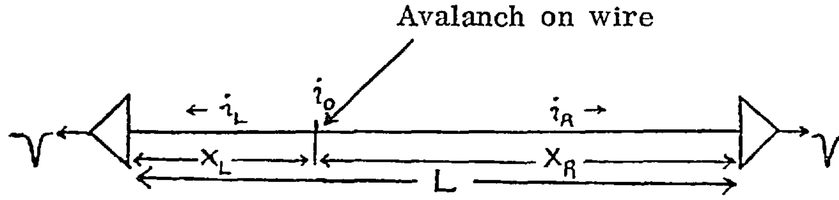

FIG. 4.7 Principle of current division

(c) Delay line

Use of current division method gives accuracies ~ 1 cm in 1 m length sense wire and hence there are difficulties in accurate position measurement. Breskin et al (1974) investigated another approach based on delay lines parallel to sense wires. Using thin delay lines of diameter less than 2 mm, and parallel to the sense wire, accuracies between 2 mm and 3 mm along the wire were obtained in a drift chamber of 150 cm length.

4.7 Imperial College drift chambers

Graded cathode drift chambers of 42.8 cm X 40.0 cm sensitive area were constructed for the experiments in π8A beam line of the Rutherford Laboratory. The details of construction is shown in Fig. 4.8 and Fig. 4.9. The frame is made from Tufnol sheets 1 cm thick. The cathode device is made from polyester sheets (5 mil) deposited with copper (0.5 mil) and etched into strips with a pitch of 5 mm. A high resistance bridge is included in the chamber and $\sim$500 V/cm is maintained across the length of the chamber. A - 12.0 KV voltage is applied on the bifilar cathode and the gain of the chamber can be adjusted by adjusting the - 3.0 KV voltage applied near the signal wire. Cathode and sense wires are made of gold plated tungsten wires of diameters 100 μm and 20 μm respectively (Fig. 4.8).

(a) X-Y chamber

In order to determine the position (x, y) of a particle, two such chambers were mounted together, each rotated through an angle of 5^{o} with the vertical (Fig. 4.10). The distance between the chambers centres were 3.1 cm, so that x, y planes in which the track co-ordinates are measured are separated by that amount. We call the two chambers which are rotated through 5^{o} each with the vertical a " module ".

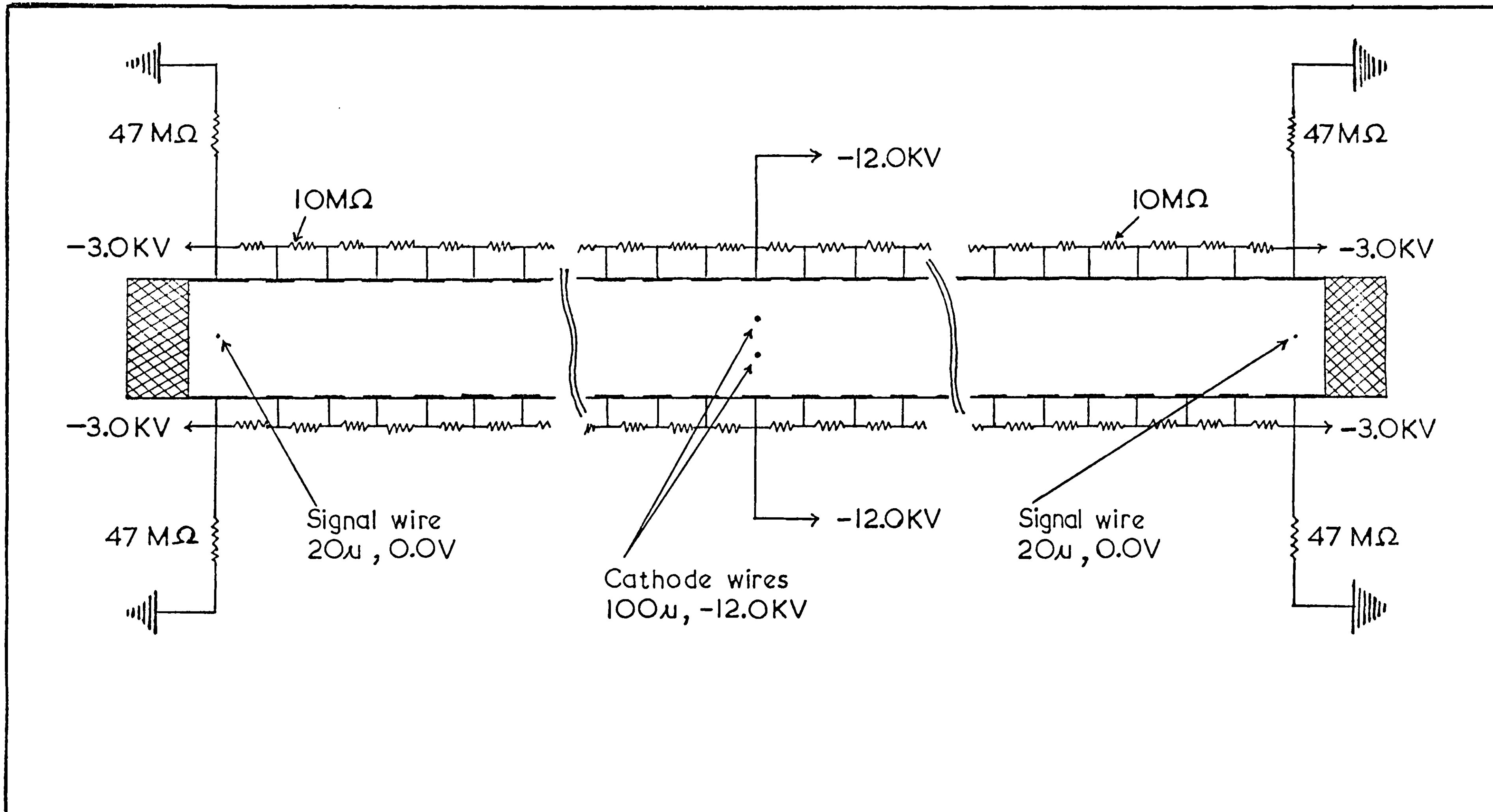

FIG. 4.8 Schematic diagram of I.C. drift chamber.

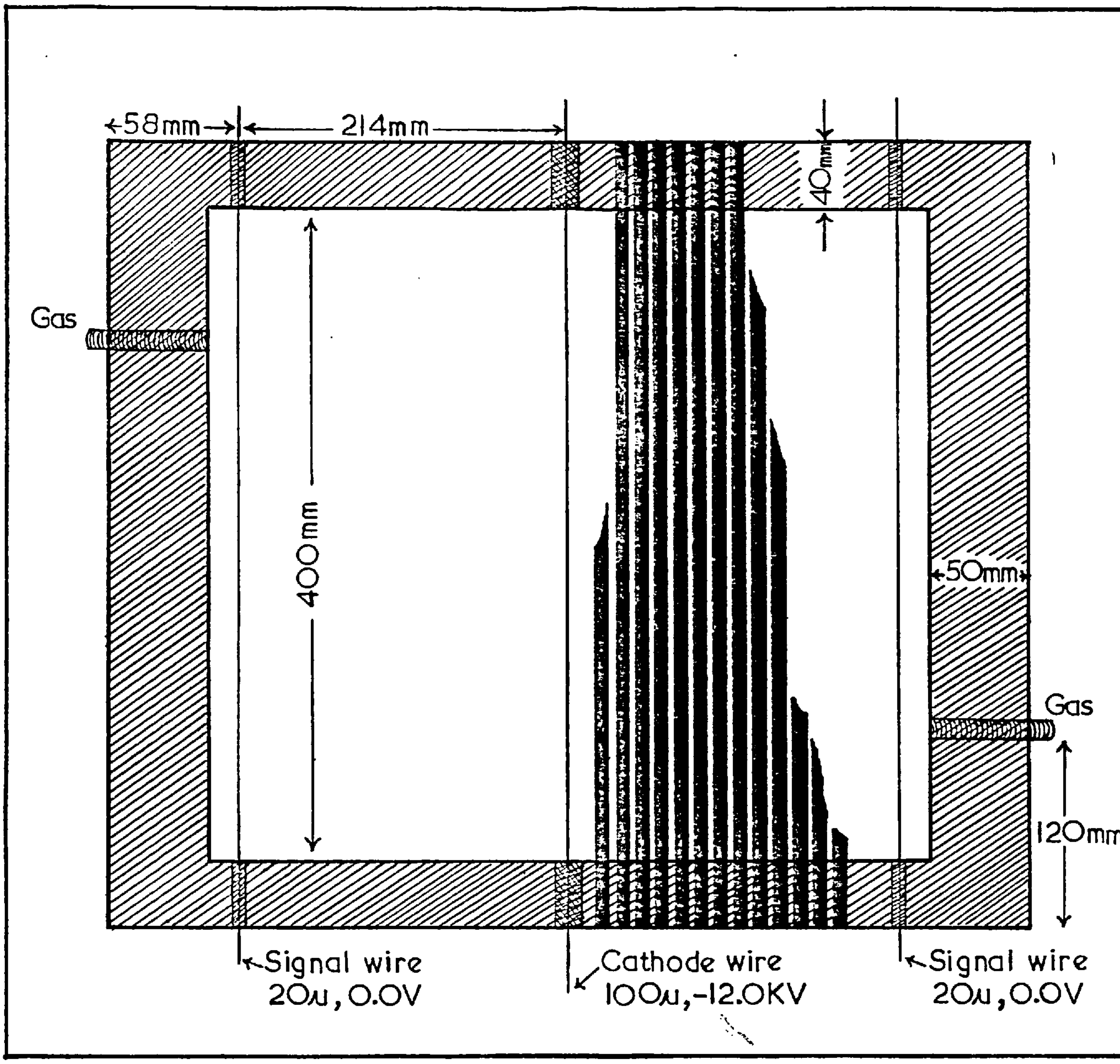

FIG. 4.9

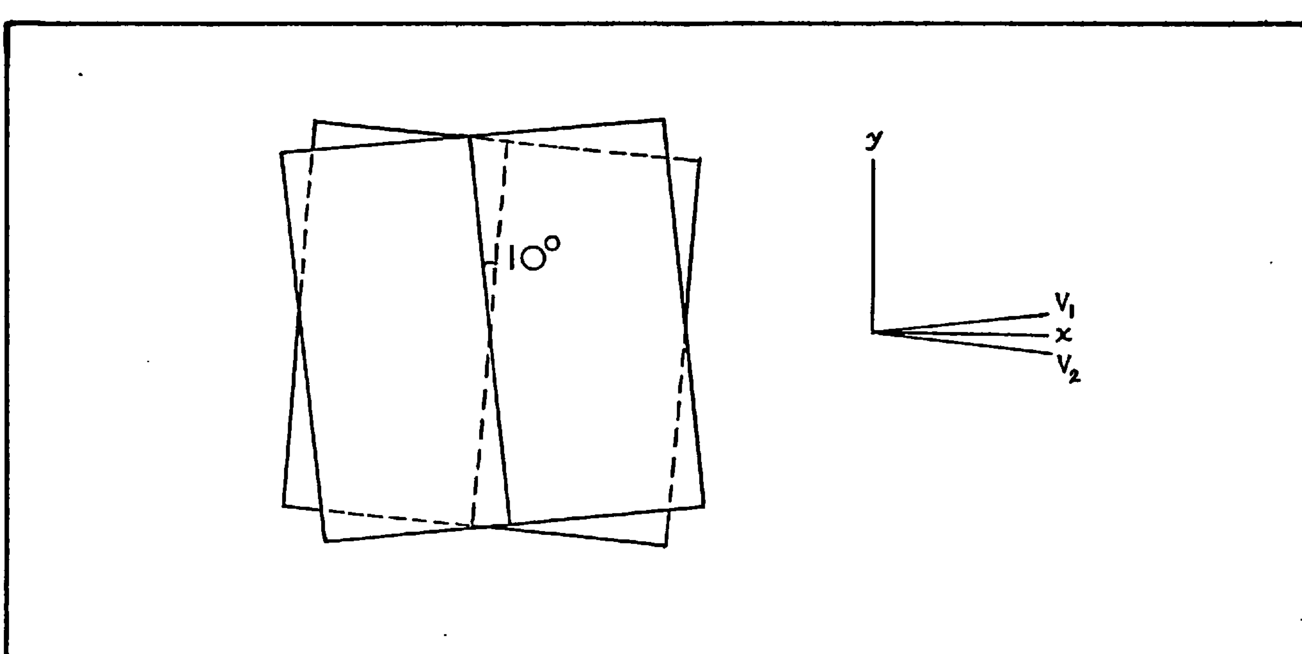

FIG. 4.10

The position and error in x and y due to the rotation of the chambers through 5^{o} with each other is given by

$$x = \frac{V_1 + V_2}{2 \cos 5^{o}} \qquad (4.11a)$$

and

$$y = \frac{V_1 - V_2}{2 \sin 5^{o}} \qquad (4.11b)$$

$$x = 0.7 \Delta v \simeq 0.7 \text{ mm (FWHH)} \qquad (4.12a)$$

$$y = 8 \Delta v \simeq 8 \text{ mm (FWHH)} \qquad (4.12b)$$

(b) Gas mixture

As we wanted short memory times, which implies a gas mixture with high drift speed, we started with 100% CH_4 and - 20 KV on cathode. The drift velocity is $\sim$ 10 cm/μsec, and has a memory time $\sim$ 2 μsec for 20 cm drift length. One of the problems which we faced was the corona discharge and noise in the module. Finally we ended up by using a mixture of 25% CH_4 and 75% Ar. For this gas mixture a lower voltage $\sim$ - 12 KV was applied to the cathode. This gas mixture gives a drift velocity of $\sim$ 7 cm/μsec in this field and hence about 3μsec memory time.

4.8 Test of the Imperial College drift chambers

Drift chambers were mounted on the traversing table for the test purposes. A two stage amplification was used in the signal wires of the drift chambers. Pulses from signal wires $\sim$ 50 μA (5μA $\rightarrow$ 200μA) were amplified by the first stage amplifier to give $\sim$ 50 mV in 50Ω for a pulse of 10μA. The second stage amplifier had an amplification factor of 25. The threshold of the discriminators were set at $\sim$ 100 mV which corresponded to $\sim$ 1μA on the signal wire. A clock consisting of a 200 MHz oscillator with a scalar (CAMAC) was started by a scintillation counter pulse and stopped by the signal from the signal wire.

(i) Linearity

The linearity between the drift distance and time of drift was tested by defining a narrow beam by a finger scintillation counter. A non-linearity of ~ 1 mm was found at ~ 2.5 mm near the cathode plane for perpendicular tracks.

Linearity for the tracks making an angle to the chamber were also tested. For this purpose the drift chambers were mounted on the traversing table making an angle of 45^{o} to the beam direction. Readings were taken for every 20 mm displacement on the traversing table which correspond to ~ 28.3 mm in drift chambers. The linearity was very good even for tracks making an angle of 45^{o} to the chambers. Fig. 4.11(a) and (b) show a typical scan at 45^{o}.

(ii) Stability of the drift speed

The stability of drift speed depends on the stabilities of gas mixture, pressure, voltage, temperature etc. Drift speeds of each run in test runs and data taking runs were calibrated from the histrogram of events which trigger both sides of signal wires. The change of drift speeds was $< 1\%$ from run to run and so it contributed a very small error in the position measurement.

(iii) Resolution

The stop and start of the 200 MHz clock were unrecognised to 1 bin, which is equivalent to 5 nsec. This corresponds to an uncertainty of ~ 0.37 mm

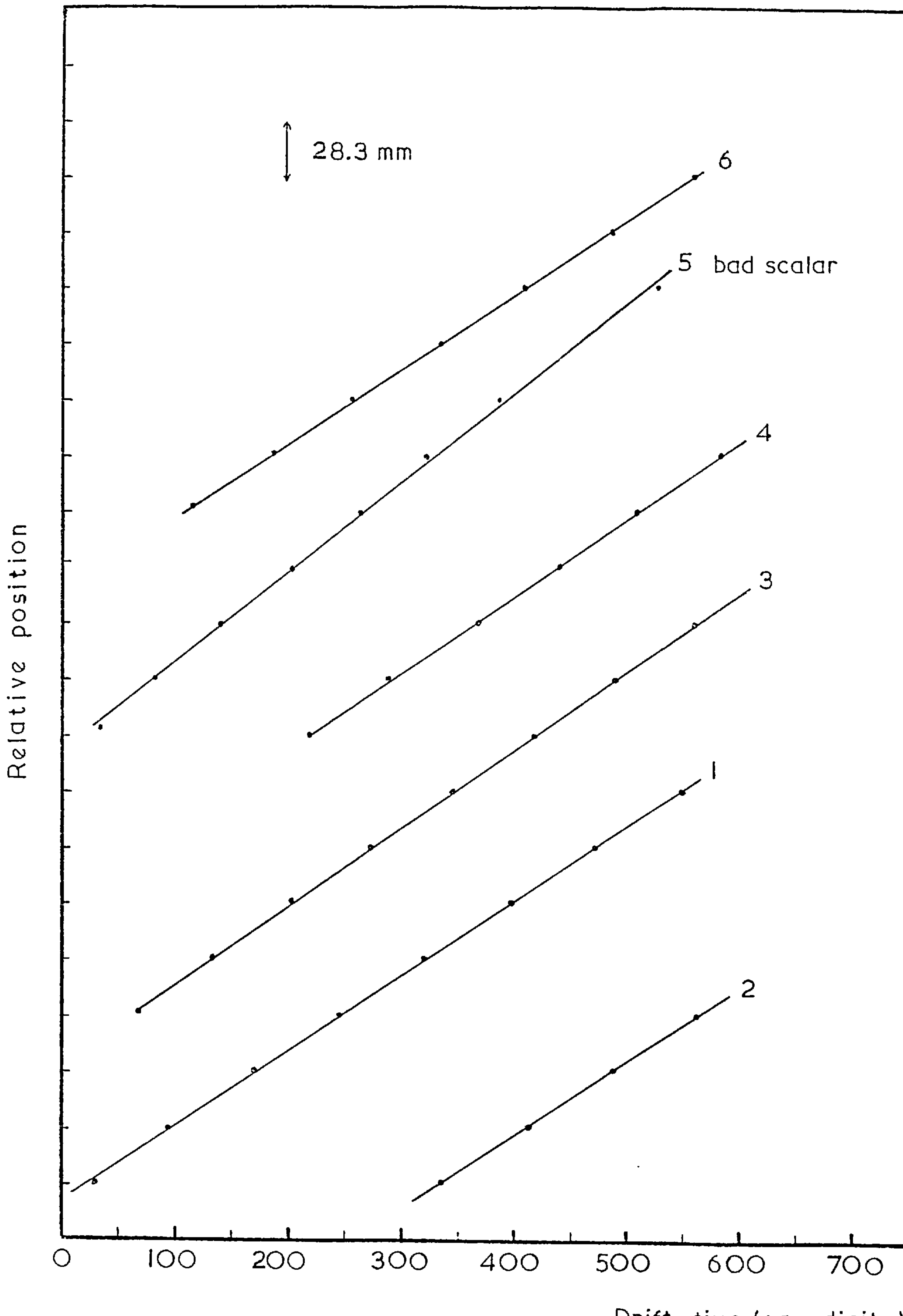
28.3 mm
6
5 bad scalar
4
3
1
2
Relative position
0
100
200
300
400
500
600
700
Drift time (raw digits)

FIG. 4.11(a)

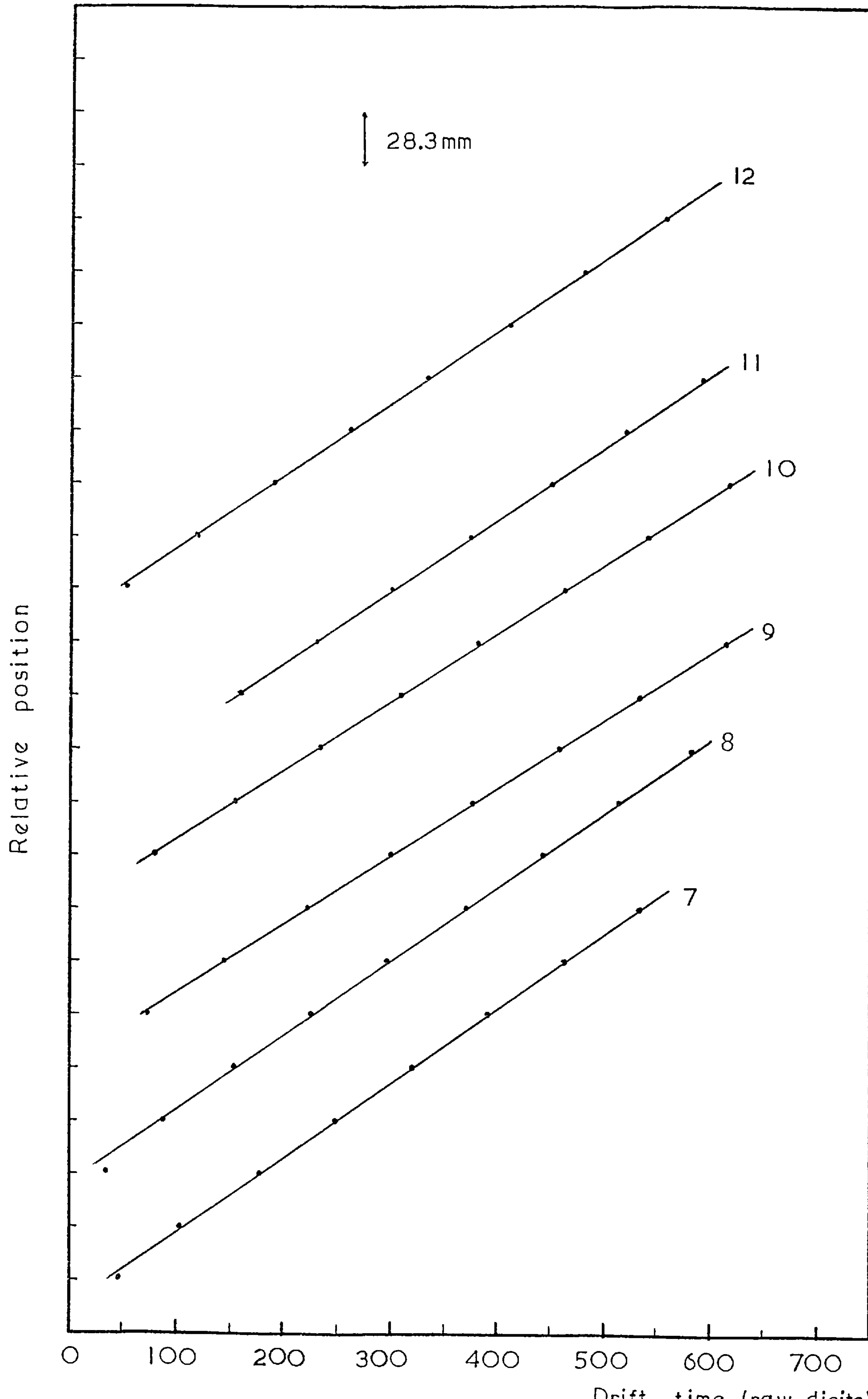
28.3mm
12
11
10
9
8
7
Relative position
0
100
200
300
400
500
600
700
Drift time (raw digits)

FIG. 4.11(b)

in position measurement.

Rise time of the signal pulses were $\sim$ 8 nsec. Pulse heights were discriminated at constant low level. The uncertainty in position measurement was less than 5 nsec ($<$ 0.37 mm) due to rise time of signal pulses.

(iv) Efficiency

The efficiency of the drift chambers were better than 99.7% for a single chamber and 99.5% for a x, y module.

5. Data collection

$\pi^- p$ elastic scattering data were collected on line, using DDP 516 computer. In all, 51 runs were taken in the momentum range from 0.600 GeV/c to 0.780 GeV/c towards the end of the year 1974.

5.1 Logic system

The experiment in principle was automatic. The permanent electronic logic and counter output circuit were connected through a suitable interface to a DDP 516 computer. The computer had been programmed to record the data on a 7 track magnetic tape for off-line analysis and to perform some preliminary analysis between the bursts. The experimenters were able to inspect histograms of various rates and counter distributions while data taking, to ensure that a run was not going wrong. The logic system was divided into

(i) The trigger logic
(ii) The readout logic
(iii) The camac registers
(iv) The interface.

The trigger logic system was designed to give every beam particle counted an equal chance of causing an event. An event was defined as a coincidence between the interaction of a beam particle in the liquid hydrogen target and counts in the D's counters. The trigger logic had three parts. The trigger logic system is shown in Fig. 5.1.

(i) Beam logic : For a genuine beam pion, a set of coincidence was made so that a beam particle had passed through only a single counter of each hodoscope array, no pulse from Čerenkov counter and a pulse from the timing counter B2. Thus for the beam logic we had

B2 1H 1G B3 $\bar{\check{C}}$ $\overline{B4}$. Four momentum channels were formed by grouping G and H combinations by the coincidence circuit. These four channels were further combined to form the total number of incident pions (ΣP_{π}).

(ii) Interaction : The interaction of a beam particle is identified by the absence of a pulse in the two circular scintillation counters, V_1 and V_2, which are positioned downstream of the liquid hydrogen target. The interaction logic was defined by B2 1G 1H B3 $\bar{\check{C}}$ $\overline{B4}$ $\overline{V_1}$ $\overline{V_2}$.

(iii) Elastic trigger : An elastic trigger logic was formed from the four scintillation counters as (D1 OR D2) AND (D3 OR D4). A coincidence of elastic trigger and interaction trigger formed the Event trigger logic.

Pulses from D's counters were timed with the gate from event trigger and formed a coincidence. When such coincidence occurred, this was the master trigger. If a particle is within $\pm$ 3.2μsec of an event which may be due to noise or background, we labelled such an event as IR = 1 otherwise IR = 0. When the master trigger occurred, it was used to strobe all counters. The state of each counter was recorded by the setting or otherwise of a corresponding bit in a set of camac parallel bit registers. Certain digitised quantities e.g. digits of the drift time of the drift chambers and digitised pulse height from the D's counters were also recorded in camac. In addition to the scalars which were read at every event, there were some which counted up throughout a burst and were read at the end of each burst. These were the total number of incident pions, the number of incident pions in each momentum bin and certain monitors.

Between the burst the events were transferred from camac to disk.

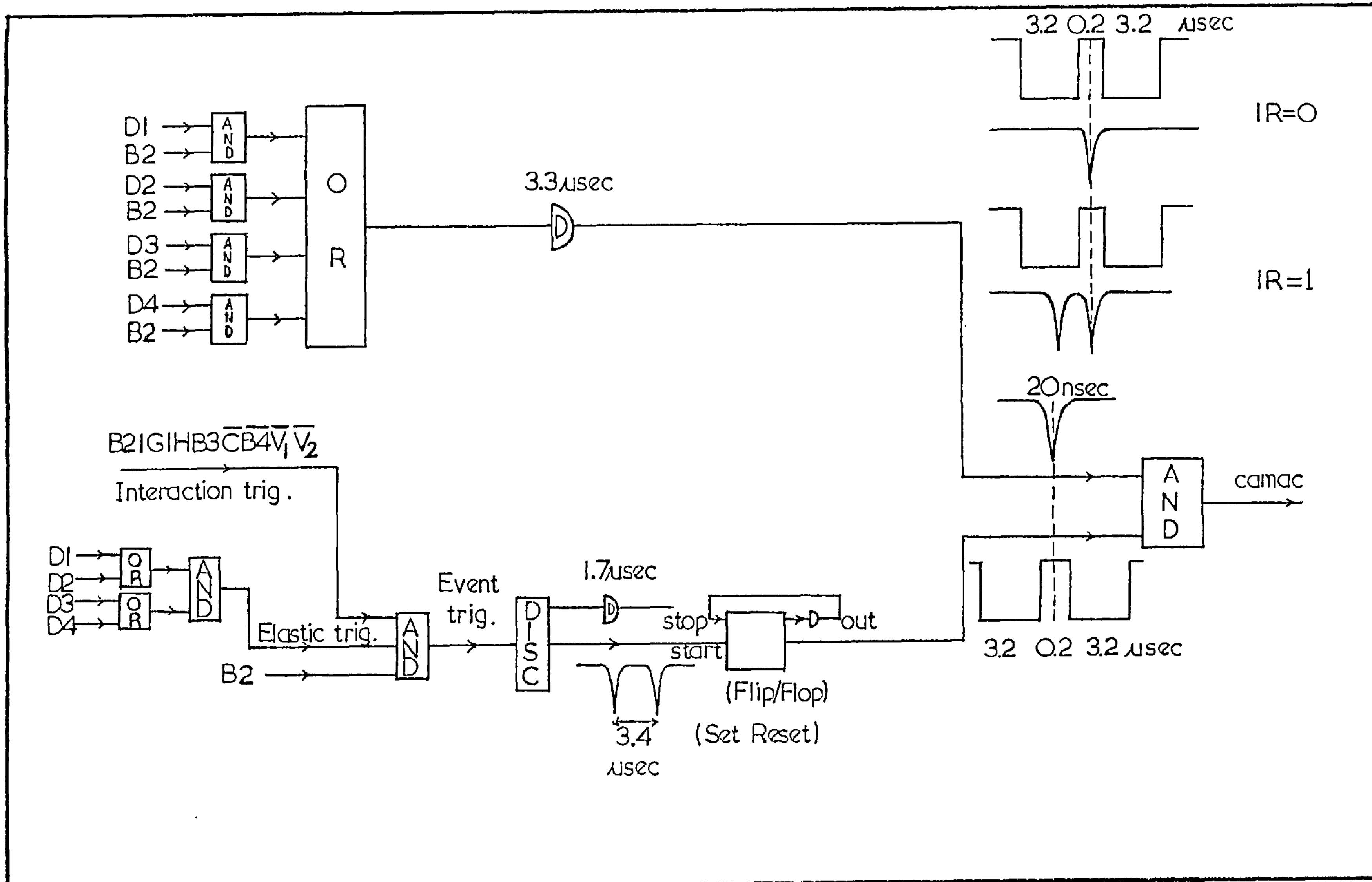

3.2 0.2 3.2 μsec
IR=0
IR=1
D1
B2
D2
B2
D3
B2
D4
B2
AND
OR
3.3μsec
20nsec
B2 1G1HB3 $\overline{C}\overline{B4}\overline{V_1}\overline{V_2}$
Interaction trig.
camac
AND
D1
D2
D3
D4
OR
OR
AND
Elastic trig.
B2
AND
Event
trig.
DISC
1.7μsec
stop
start
out
3.2 0.2 3.2 μsec
(Flip/Flop)
(Set Reset)
3.4
μsec

FIG. 5.1

The data was written in blocks of 18 events. Also between the bursts, the events of the last burst were read into core and a number of register addresses in the computer were updated. All the registers were set to zero between bursts. In order to have an idea of beam distribution, after every fifth event trigger, beam trigger events were collected called "beam sample".

5.2 Mode of data collection

The experiment for $\pi^- p$ elastic scattering near η-threshold was performed towards the end of 1974. Nimrod accelerates a circulating beam of $\sim 3 \times 10^{12}$ protons/pulse and pulse repetition rate was 22 times a minute. The extracted proton beam strikes a copper target and π^- 8A beam line was designed for π^-, covering the momentum range of 0.600 GeV/c to $\sim$ 2.000 GeV/c and has a production angle 7^o. The negative pion beam gave on average 50 K beam trigger and $\sim$ 80 event triggers. After each burst the data was transferred from camac to computer and arranged in blocks of 18 events. Every 3 or 4 bursts when 216 events had been recorded, a set of block was written onto 7 tracks magnetic tape. Each tape could record about 7000 blocks and was thus completed in approximately 1 hr and 30 minutes. A run corresponds to one full tape and contained about 60 to 80 million beam pions.

Each run was characterized by its central beam spectrometer momentum, and covered a range of 4 bins corresponding to different G and H hodoscope combinations. Most of the data was taken around the η-threshold.

Systematic effects are reduced when a momentum bin has contributions from other several runs. Around the η-threshold we had a number of runs contributing to the same momentum bin. To further reduce the systematic effects the momentum setting was varied after at least three runs. The beam current setting for a different momentum took less than 20 minutes.

Before each run the currents to the magnet were set to the proper values corresponding to the momentum of the run. The currents for M 201 and M 202 were adjusted to give the correct NMR frequencies. The signals from the proton probes were monitored by TV cameras and displayed in the control room on TV screens. The stability of the fields could be checked by observing the positions of the signals throughout data taking period. The stabilities of M 201 and M 202 were much better than 1 part in 10^4. The currents in quadrupoles Q 113 and Q 402 were always cycled slowly towards the final values in order to remove the hysteresis effect. Finally the current in M 213 was adjusted so as to make the beam distributionsymmetric about the centre of H wire chamber. Before the start of data taking, the beam distribution, histograms of drift chamber scalars etc. were checked on-line in the computer. If everything was all right the run parameters would then be typed into the index block of the new tape and data taking would be started. In all 51 runs were taken for $\pi^- p$ elastic sacattering in the momentum range of 0.600 GeV/c to 0.780 GeV/c. Table 5.1 shows the run number, central momentum and useful pions collected in each run. Fig. 5.2 shows the number of incident beam pions that were accumulated in 0.50 MeV/c bin.

Table 5.1

Distribution of data taking runs (Calibration runs not included)

Run number	Momentum in GeV/c	Total number of pions (millions)
424	0.6648	46.59
425	0.6694	55.92
426	0.6744	54.01
427	0.6790	15.01
428	0.6790	49.41
429	0.6790	32.13
430	0.6836	49.21
431	0.6836	50.10
432	0.6882	48.38
433	0.6882	46.24
434	0.6882	47.30
435	0.6900	47.71
436	0.6900	49.32
437	0.6900	47.71
438	0.6928	47.89
439	0.6928	47.44
440	0.6928	48.18
441	0.6974	46.82
442	0.6974	45.25
443	0.7020	46.43
444	0.7020	44.50
445	0.7067	43.30
446	0.7114	43.13
447	0.7200	42.93
448	0.7200	43.77
449	0.7114	40.43
450	0.7067	44.43
451	0.7020	48.72
452	0.7020	44.63
453	0.6974	48.50
454	0.6974	46.59
455	0.6928	48.18
456	0.6928	48.45
457	0.6928	47.95
458	0.6900	48.90
459	0.6900	51.88
460	0.6900	51.23
461	0.6882	48.69
462	0.6882	50.27
463	0.6882	43.16
464	0.6836	51.97
465	0.6836	52.84
466	0.6790	51.94
467	0.6790	53.56
468	0.6744	48.18
470	0.6694	55.24
471	0.6648	49.76
472	0.6400	62.84
473	0.6000	73.62
474	0.7400	45.11
475	0.7800	51.80

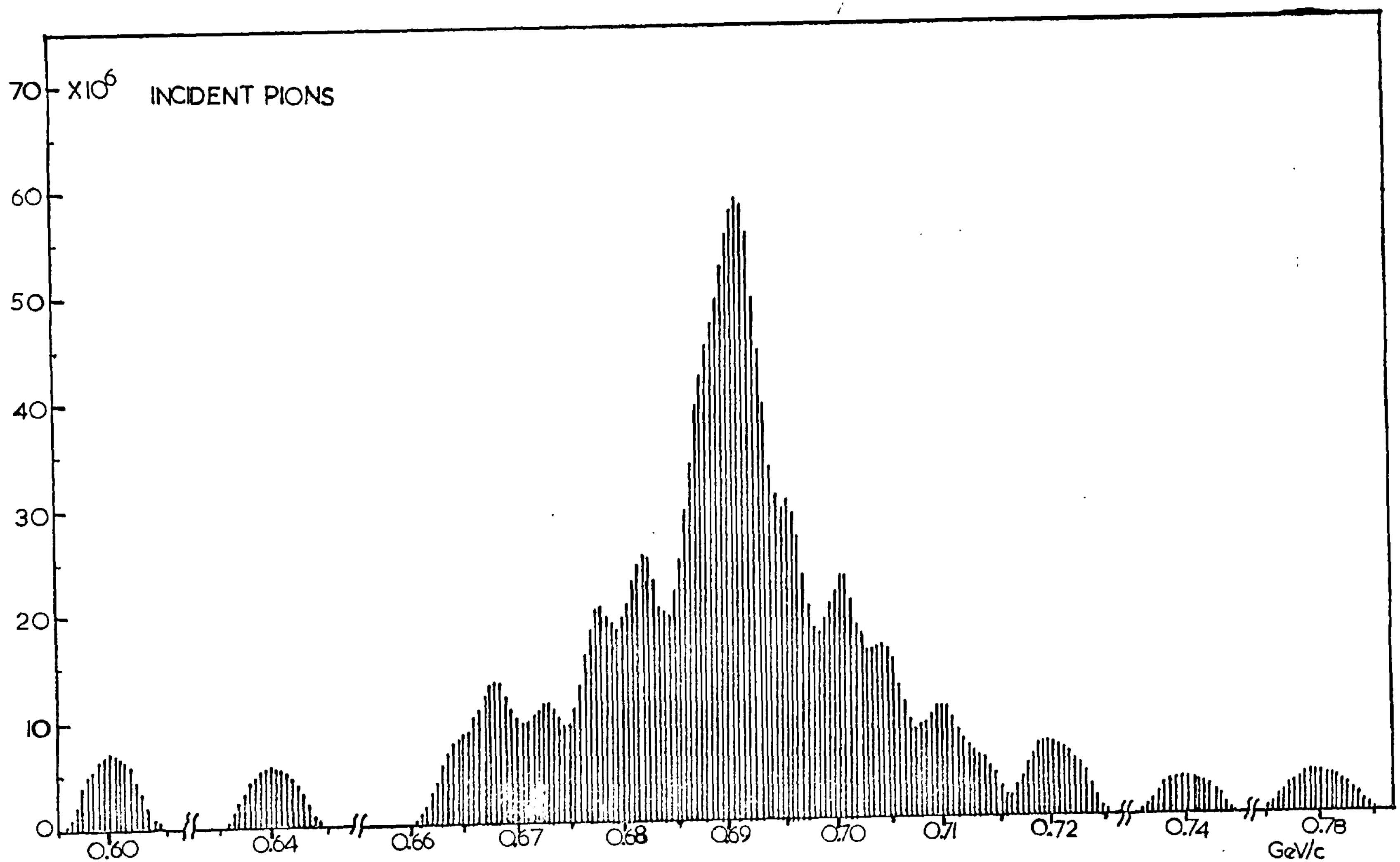

FIG. 5.2 Total number of incident pions that were accumulated in each 0.50 MeV/c momentum bin.

6. Data analysis

This chapter describes the off-line analysis of the data.

6.1 Enriching the data

Each raw data tape contains about 7000 blocks. Each block is itself self contained, in the sense that a block contains (i) complete information on different triggers (ii) beam sample events and (iii) different scalars e.g. $\sum P_{\pi}$ and monitors. A tape covered a pion momentum range of about 10 MeV/c. We had 47 tapes for a range of p_{π} from 0.660 GeV/c to 0.720 GeV/c. In general we had 3tapes/beam momentum setting.

The enriching programme examined the data structure and if a block does not have proper $\sum P_{\pi}$, such blocks were rejected so as not to disturb in the normalisation.

Events having only good wire chamber information, and which are not beam sample and do not have the interference remover (IR) bit set were written onto enriched tapes. The beam sample momentum distribution was written for each run in a permanently mounted disk data set in 80 bins, each bin having a width of 1/40.5 % of the central momentum setting of that run. The absolute central momentum of each run was known to better than 1 part in 10^4 from the NMR frequency. The momentum for each beam sample event or elastic event was calculated from the wire chamber information of G and H, together with the angle measurement from J, K and L wire chambers.

As we required drift velocities for the construction of tracks, throughout the enriching process, the drift velocities were calculated for each side of the drift chambers for each run from the distribution of events which trigger both sides of the signal wire. In Fig. 6.1(a) and (b), we have shown the distribution of events which trigger both sides of the signal wire in a typical run. The drift chamber velocities, the beam scalar and other information were also written in the disk data set in addition to the beam sample momentum distribution.

For each run the momentum distribution of the beam sample events were normalised to ΣP_{π} after correcting for the observed inefficiency and then combined in an array having 0.5 MeV/c bin width. For the elastic events each run was combined and then stored in a three dimensional array (momentum, interaction point, c.m. scattering angle), and then each bin was normalised to the corresponding momentum bin of the beam sample. After the normalisation, the momentum of the elastic events had to include the correction for ionisation loss in the liquid hydrogen target.

The error of the normalised elastic events was stored in a two dimensional (momentum and c.m. scattering angle) array.

6.2 Writing DST (Data Summary Tape)

The drift velocities which were written in the disk data set in the enriching process were used to find the coordinates for the tracks in each module separately in the module frame. Upto six points which were obtained from the drift chambers in the module frame were then transferred to the beam frame. Using a least squares fitting programme a line was fitted to the points for each "side" or "box". The fits in the xz and xy planes (Fig. 3.2) were carried out independently. Extrapolation of the fitted tracks in the liquid hydrogen target gives the interaction point. If the two tracks did not meet at a point with the beam track, then an average interaction point is calculated. For fitting tracks in the xy plane this interaction point in the liquid hydrogen target was also included. A small correction was applied for the tracks making an angle to the module. Fig. 6.2 and Fig. 6.3

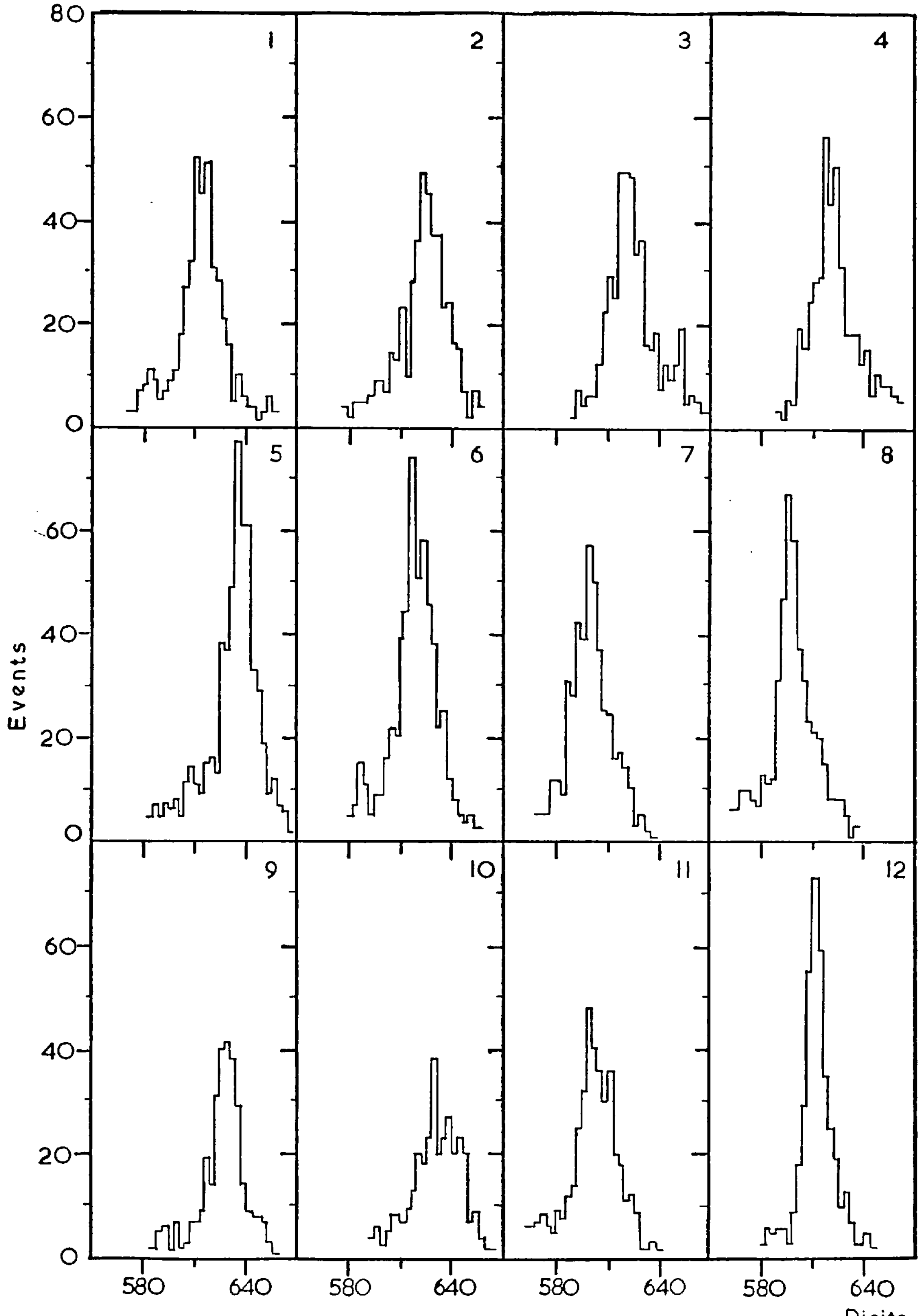

FIG. 6.1 (a)

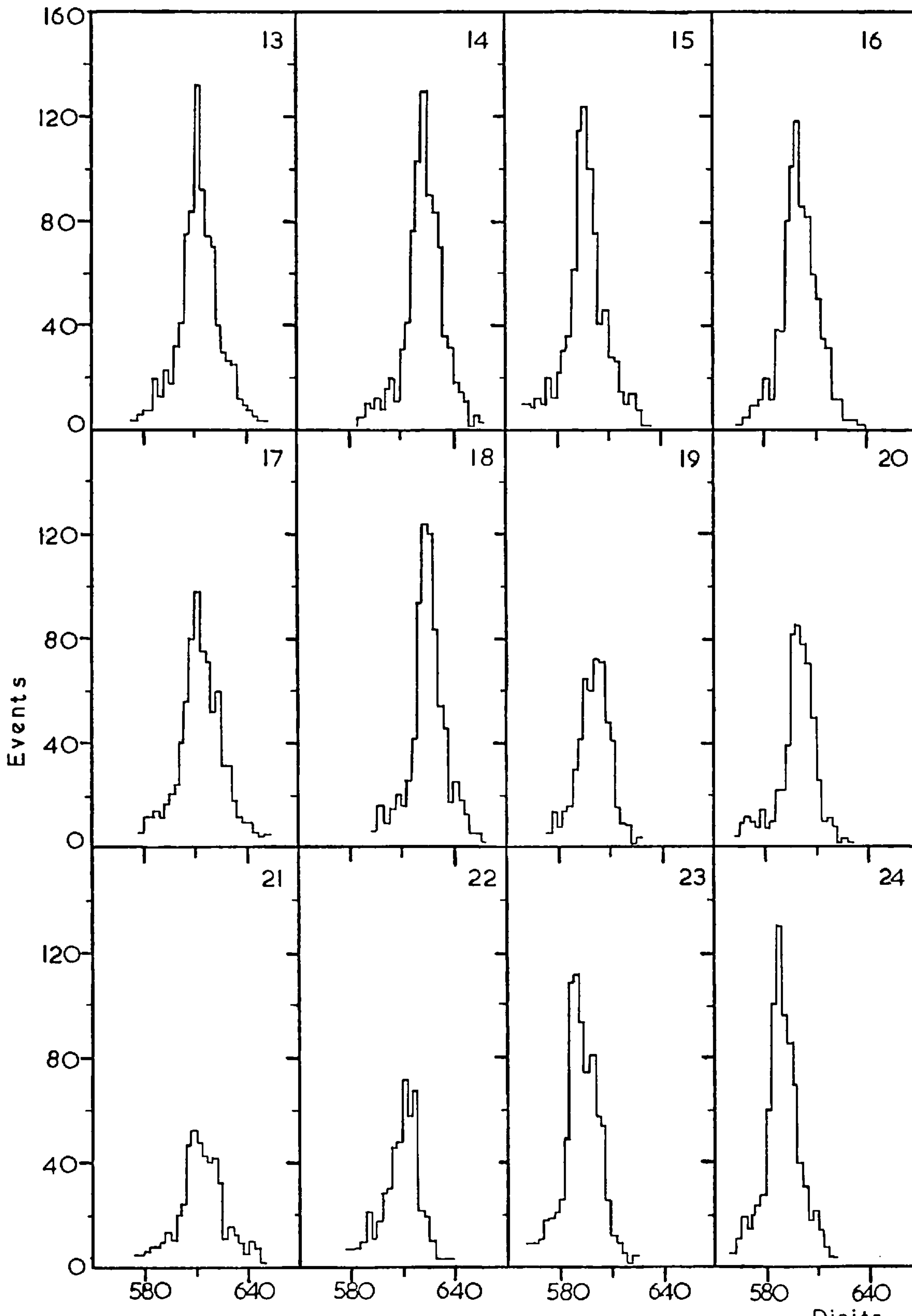
160
120
80
40
0
Events
13
14
15
16
17
18
19
20
21
22
23
24
580
640
Digits

FIG. 6.1 (b)

show rms deviation of the fitted tracks for a typical run for the side 1 and 2 respectively. $\sigma_x \simeq 0.5$mm for the side 1 while for side 2 it is about 0.4mm. Fig. 6.4 shows the angle between the tracks in the xy plane which is integrated over all positions in the chambers and all range of angles. The angular resolution in xy plane is about $\pm 4.0^{\circ}$. After the construction of tracks, the angles made by the tracks with respect to the incident beam direction were found out. Because of the finite angular resolution the two tracks usually did not meet at a point with the incident beam trajectory. Fig. 6.5 shows the distribution of the difference of the intersection of the tracks with the incident beam. The rms deviation is about 8.0mm.

The distinction of π^- and p tracks were made by kinematics constraints. Fig. 6.7 shows the variation of pion scattering angle (θ_π) with proton scattering angle (θ_p), in laboratory, for a pion beam momentum of 0.702 GeV/c. The dashed lines show approximately the effect of angular resolution. π^- and p cannot be distinguished at a c.m. scattering angle $\simeq 74.0^{\circ}$ ($\cos\theta^* \simeq 0.28$), which corresponds to $\theta_\pi \simeq \theta_p \simeq 50.4^{\circ}$ in the laboratory, by the kinematics constraints. Pulse height information of D3 and D4 were used in the ambiguity region. Fig. 6.8 shows the pulse height distribution of π^- and p for D3 and D4. The minimum position between π^- and p peaks shifts slowly with momentum. The programme which distinguishes between π^- and p from the pulse height information in the ambiguity region took into account this shift.

Events usually do not lie exactly either on A or B as given by kinematics (Fig. 6.7). Kinematics constraints allow us to establish the event to be associated either with A or B. Once it is established the determination of θ^* (c.m. scattering angle) is carried out as follows:

Let us have an event having coordinates θ_π and θ_p , which is associated with A. The c.m. scattering angle θ^*_π is given by,

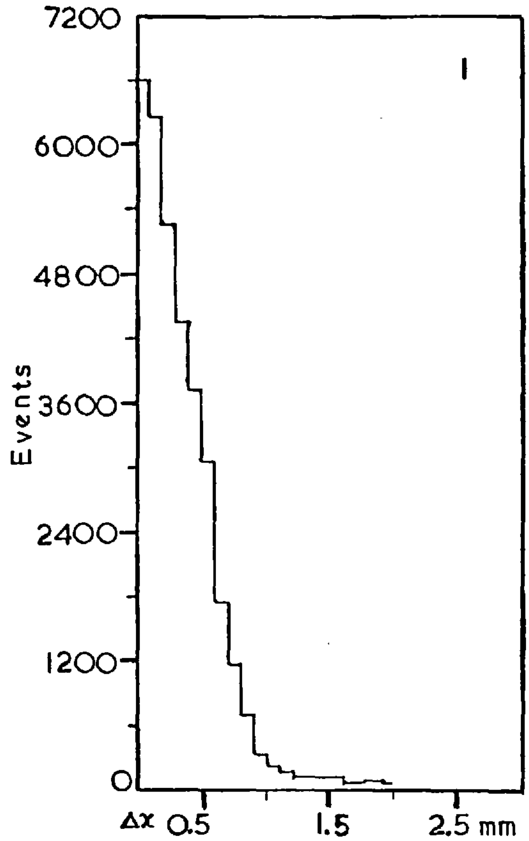

FIG. 6.2

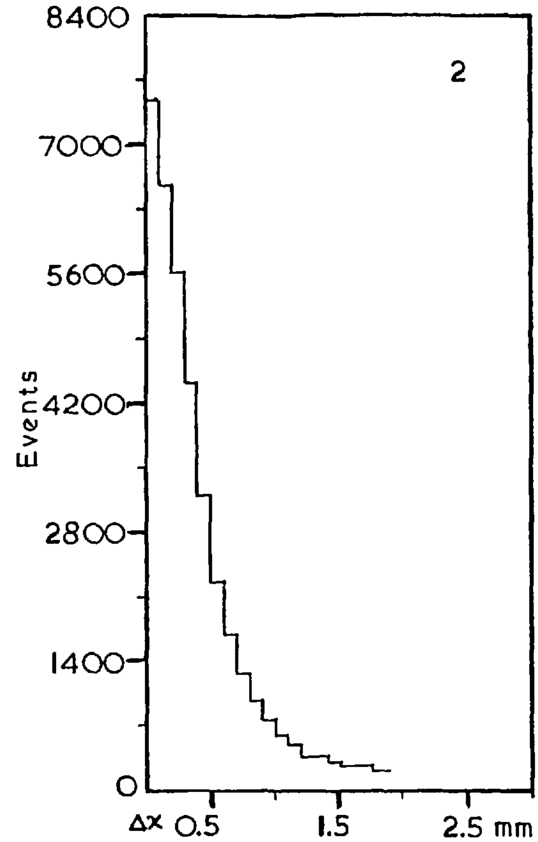

FIG. 6.3

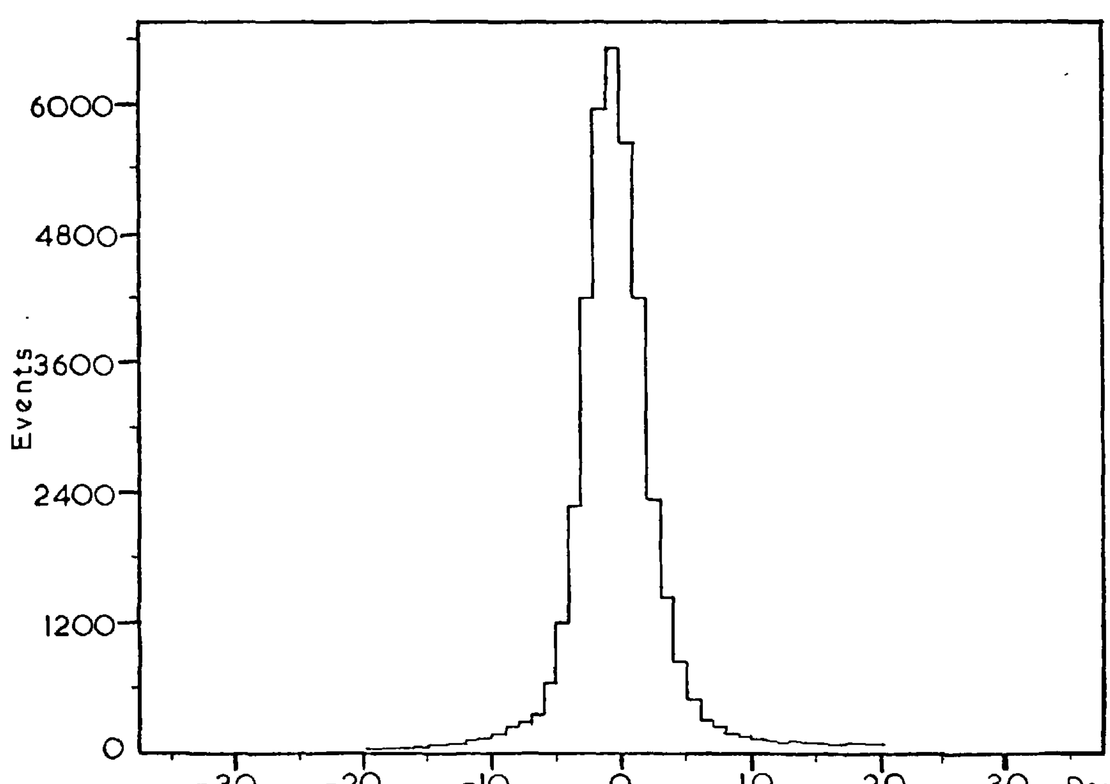

FIG.6.4 Angle between the tracks in XY plane.

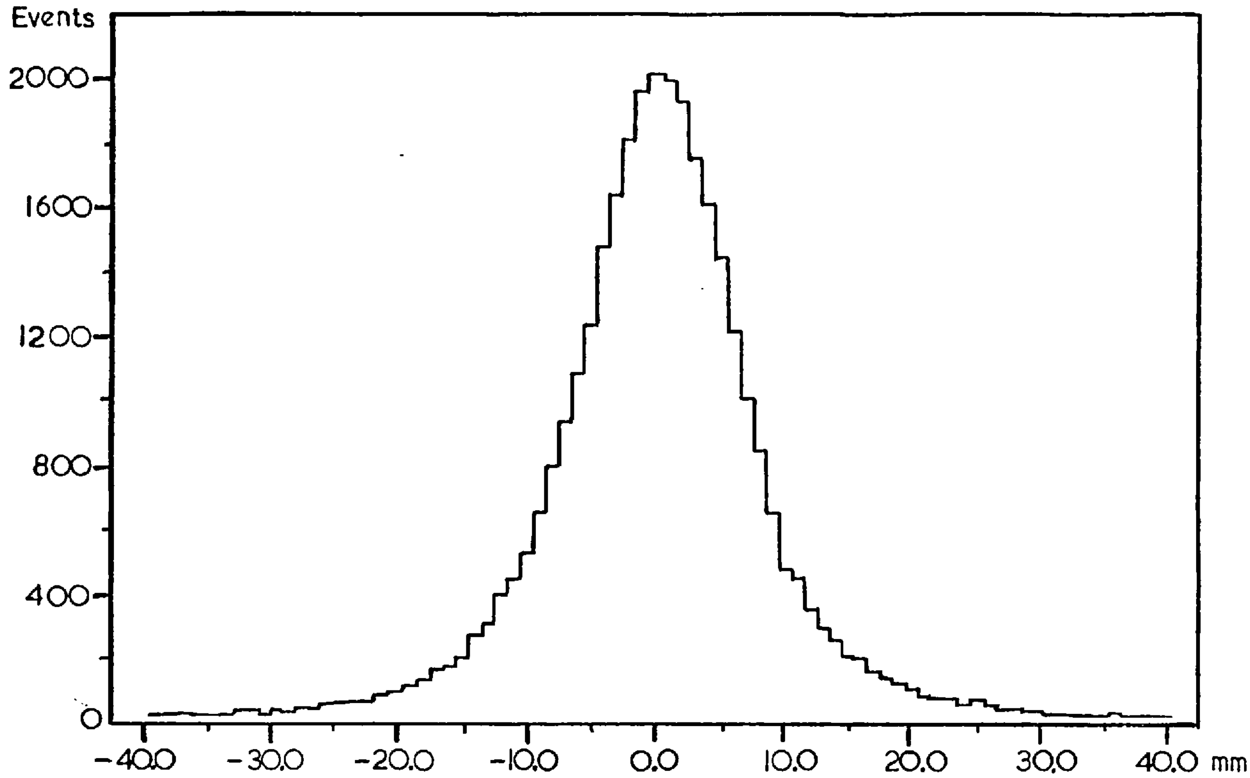

FIG. 6.5 Difference in intersection of tracks with beam track.

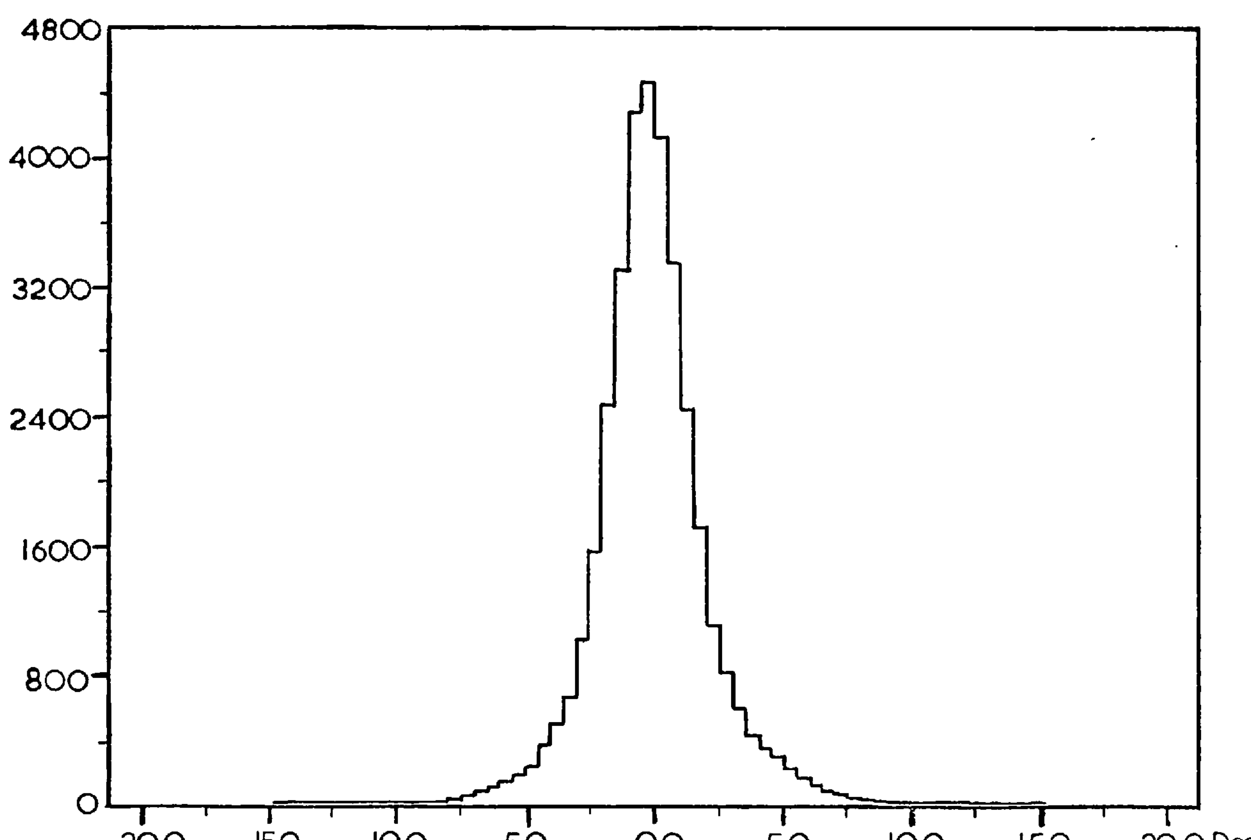

FIG. 6.6

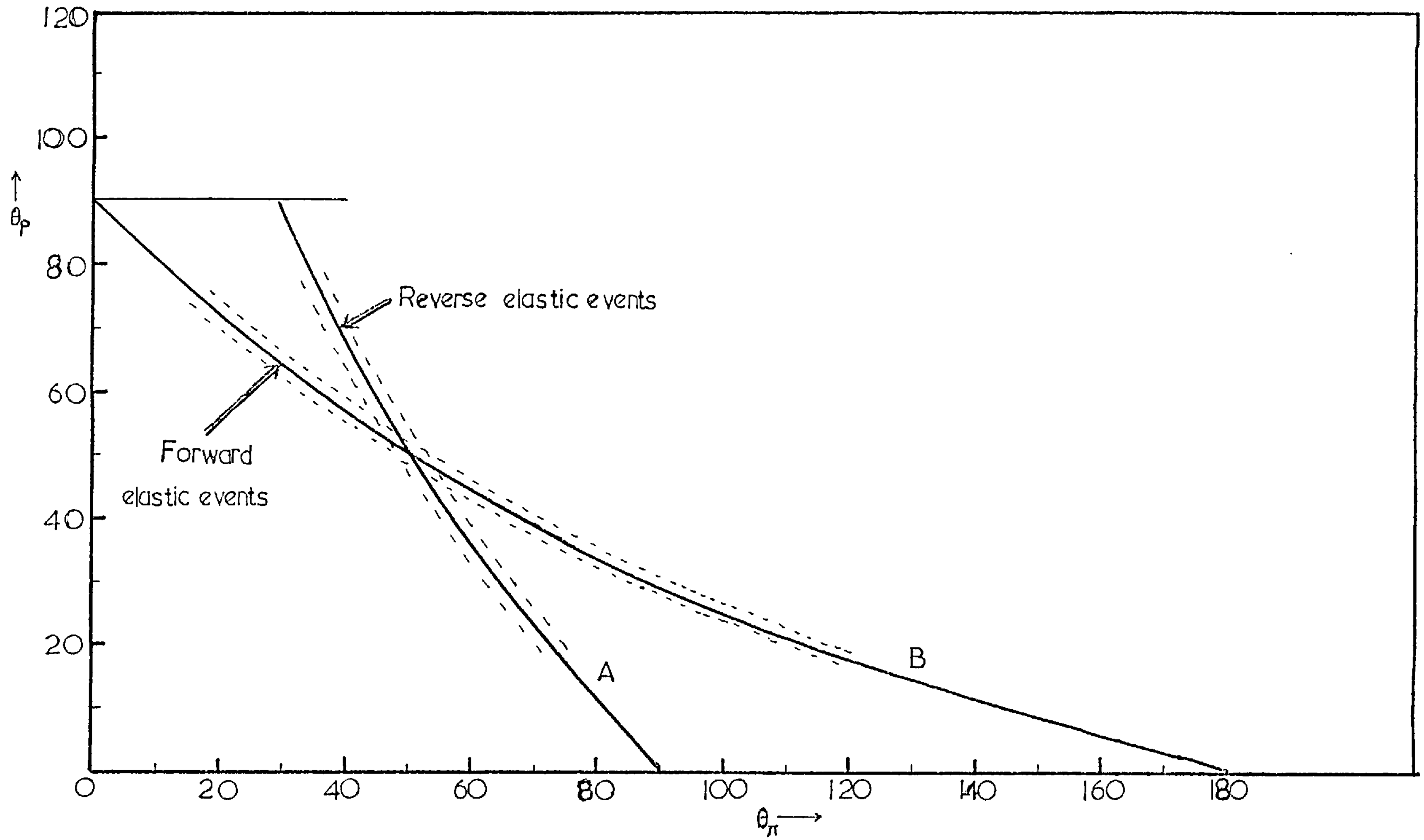

FIG. 6.7 Variation of pion scattering angle (θ_π) with proton scattering angle (θ_p), for a pion beam momemtum of 0.702 GeV/c. The dashed lines show approximately the effect of angular resolution.

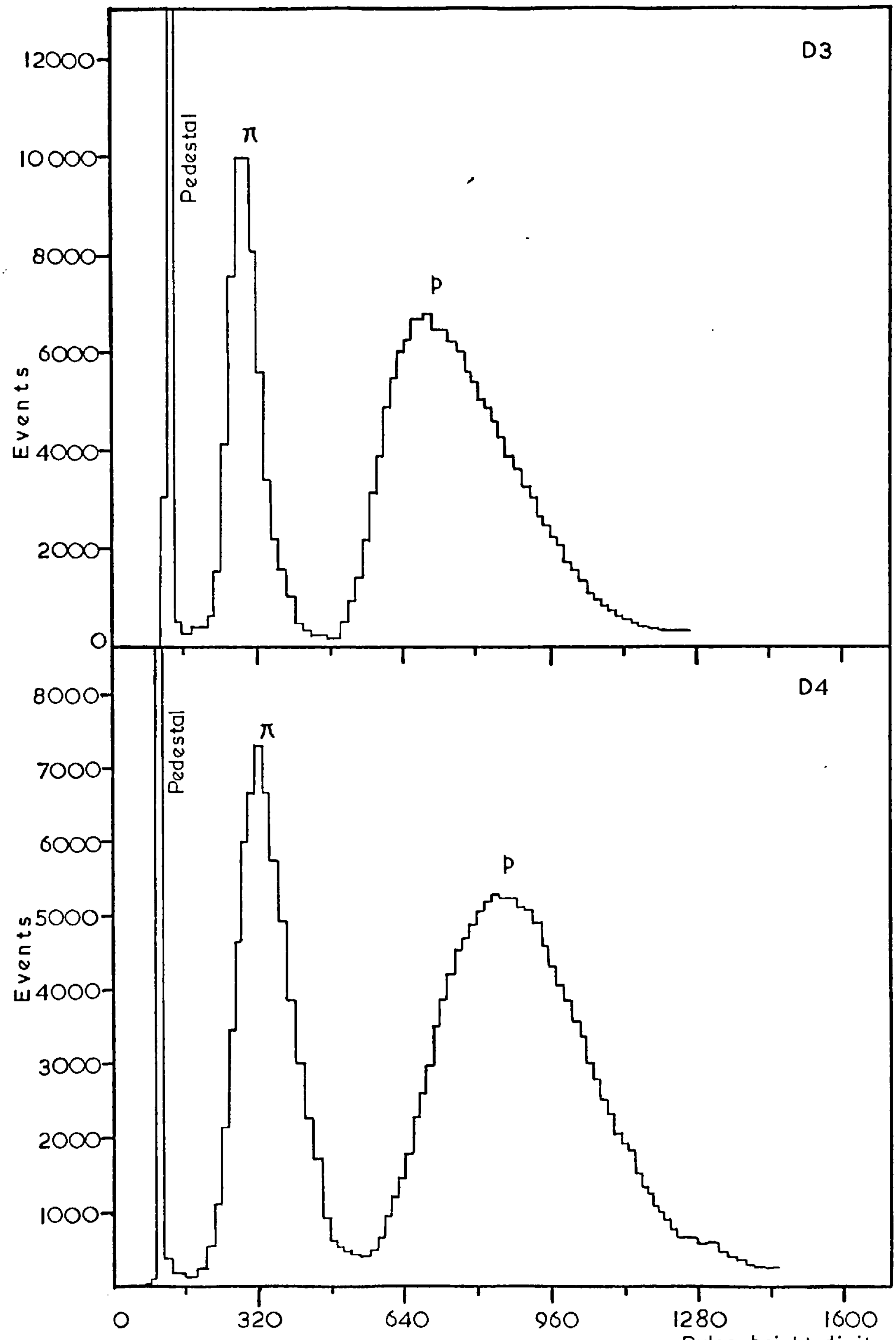

D3
12000
10 000
8000
6000
4000
2000
0
Events
Pedestal
π
p
D4
8000
7000
6000
5000
4000
3000
2000
1000
Events
Pedestal
π
p
0
320
640
960
1280
1600
Pulse height digits

FIG. 6.8

$$\theta_{\pi}^{*} = \mathrm{Cos}^{-1}\left[\frac{\gamma_c^{2}\beta_c \pm \left[\gamma_c^{4}\beta_c^{2} - (\gamma_c^{2} + \mathrm{Cot}^{2}\theta_3)(\gamma_c^{2}\beta_c^{2} - \beta_3^{*2}\mathrm{Cot}^{2}\theta_3)\right]^{1/2}}{\beta_3^{*}(\gamma_c^{2} + \mathrm{Cot}^{2}\theta_3)}\right]$$

$+$ for $\theta_3 \leqslant 90^{0}$

$-$ for $\theta_3 > 90^{0}$ (6.1a)

Similarly the c.m. scattering angle θ_p^{*} is given by,

$$\theta_{p}^{*} = \mathrm{Cos}^{-1}\left[\frac{\gamma_c^{2}\beta_c - \left[\gamma_c^{2}\beta_c^{2} - (\gamma_c^{2} + \mathrm{Cot}^{2}\theta_4)(\gamma_c^{2}\beta_c^{2} - \beta_4^{*2}\mathrm{Cot}^{2}\theta_4)\right]^{1/2}}{\beta_4^{*}(\gamma_c^{2} + \mathrm{Cot}^{2}\theta_4)}\right] \quad (6.1b)$$

Assuming the errors associated in the measurement of π^{-} and p angles in the laboratory are independent and same for both particles, we can write θ^{*} (c.m. scattering angle) as,

$$\theta^{*} = \frac{\left(\theta_{\pi}^{*}\left|\frac{\partial\theta_p^{*}}{\partial\theta_p}\right| + \theta_p^{*}\left|\frac{\partial\theta_{\pi}^{*}}{\partial\theta_{\pi}}\right|\right)}{\left(\left|\frac{\partial\theta_p^{*}}{\partial\theta_p}\right| + \left|\frac{\partial\theta_{\pi}^{*}}{\partial\theta_{\pi}}\right|\right)} \quad (6.2)$$

where

$$\left(\frac{\partial\theta_p^{*}}{\partial\theta_p}\right) = \frac{1 + \mathrm{Cot}^{2}\theta_4}{\gamma_c\left(\frac{\mathrm{Cos}\,\theta_p^{*}\,(\beta_c + \beta_4^{*}\mathrm{Cos}\,\theta_p^{*})}{\beta_4^{*}\,\mathrm{Sin}^{2}\,\theta_4^{*}} - 1\right)} \quad (6.3a)$$

and

$$\left(\frac{\partial\theta_{\pi}^{*}}{\partial\theta_{\pi}}\right) = \frac{1 + \mathrm{Cot}^{2}\theta_3}{\gamma_c\left(\frac{\mathrm{Cos}\,\theta_{\pi}^{*}\,(\beta_c + \beta_3^{*}\mathrm{Cos}\,\theta_{\pi}^{*})}{\beta_3^{*}\,\mathrm{Sin}^{2}\,\theta_{\pi}^{*}} + 1\right)} \quad (6.3b)$$

Quantities with * are expressed in the c.m. system. For elastic scattering,

$$\pi^- + p \rightarrow \pi^- + p$$
$$1 \quad 2 \qquad 3 \quad 4$$

S the square of the total c.m. energy is,

$$S = m_1^2 + m_2^2 + 2E_1 m_2 \qquad (6.4)$$

where E_1 is the energy of the incident pion and is related to the incident momentum p_1 by

$$E_1 = \sqrt{m_1^2 + p_1^2} \qquad (6.5a)$$

$$\beta_c = \frac{p_1}{E_1 + m_2} \quad ; \quad \gamma_c = \frac{E_1 + m_2}{\sqrt{S}} \quad ; \quad \beta_c \gamma_c = \frac{p_1}{\sqrt{S}} \qquad (6.5b)$$

$$\beta_3^* = \frac{p_3^*}{E_3^*} \quad ; \quad \beta_4^* = \frac{p_4^*}{E_4^*} \qquad (6.5c)$$

where,

$$\left| p_3^* \right| = \left| p_4^* \right| = \left[\frac{(S - (m_3 + m_4)^2)(S - (m_3 - m_4)^2)}{4S} \right]^{1/2} \qquad (6.6)$$

Fig. 6.6 shows the distribution of ($\theta_\pi^* - \theta_p^*$) (= THDIF) for all angles. The angular resolution in c.m. is $\sim \pm 2.0^\circ$. Because of the multiple Coulomb scattering in the detecting system this angular resolution resolution is the limit with our drift chambers system.

(a) Cuts

The followigs cuts were imposed on events in wrtiting DST.

(i) DZX cut: 3mm cut was made in the rms deviation of the least squares fitting of the points on each side of the box. Constructed tracks having more than 3mm rms deviation were not written onto DST.

(ii) ZD cut: 3cm cut was made for the difference of intersection of the two tracks with the incident beam. Events having more than 3cm in ZD were not written in the DST.

(iii) ZIM cut: In order to have the interaction point in the liquid hydrogen target, a 22cm cut was made. This cut is slightly more than the length of the liquid hydrogen target, which is 20cm.

(iv) TXY cut: The two constructed tracks should be within 10° of coplanarity. Tracks having acoplanarity angle more than 10° were rejected.

(v) THDIF cut: If $|\theta_{\pi}^{*} - \theta_{p}^{*}|$ is greater than 10°, such events were not written in DST. Events having $|\theta_{\pi}^{*} - \theta_{p}^{*}|$ lying between $40^{\circ} \rightarrow 80^{\circ}$ were also stored in a different array, for the study of background contribution to elastic events.

Events having passed the above cuts were written in DST in an array ELAS (75, 80, 15), 75 bins of interaction points in the liquid hydrogen target (bin size = 3.0mm), 80 bins of momentum (bin size $\approx$ 0.18 MeV/c) and 15 different θ^{*}, the c.m. scattering angle. The fifteen different θ^{*} regions are given in Table 6.1.

From the constructed tracks the following percent were found to be inelastic or interaction outside the liquid hydrogen target.

Table 6.1.

Region	θ^* (degrees)	Cos θ^*	Mean Cos θ^*
1	30.68 → 40.54	$0.86 \geqslant \cos\theta^* > 0.76$	0.81
2	40.54 → 48.70	$0.76 \geqslant \cos\theta^* > 0.66$	0.71
3	48.70 → 55.94	$0.66 \geqslant \cos\theta^* > 0.56$	0.61
4	55.94 → 62.61	$0.56 \geqslant \cos\theta^* > 0.46$	0.51
5	62.61 → 68.90	$0.46 \geqslant \cos\theta^* > 0.36$	0.41
6	68.90 → 74.93	$0.36 \geqslant \cos\theta^* > 0.26$	0.31
7	74.93 → 80.79	$0.26 \geqslant \cos\theta^* > 0.16$	0.21
8	80.79 → 86.56	$0.16 \geqslant \cos\theta^* > 0.06$	0.11
9	86.56 → 92.29	$0.06 \geqslant \cos\theta^* > -0.04$	0.01
10	92.29 → 98.05	$-0.04 \geqslant \cos\theta^* > -0.14$	-0.09
11	98.05 → 103.89	$-0.14 \geqslant \cos\theta^* > -0.24$	-0.19
12	103.89 → 109.88	$-0.24 \geqslant \cos\theta^* > -0.34$	-0.29
13	109.88 → 116.10	$-0.34 \geqslant \cos\theta^* > -0.44$	-0.39
14	116.10 → 122.68	$-0.44 \geqslant \cos\theta^* > -0.54$	-0.49
15	122.68 → 129.79	$-0.54 \geqslant \cos\theta^* > -0.64$	-0.59

(i) 5.3% (ZIM cut) was found to be interaction outside the liquid hydrogen target. The interactions were mainly from the materials around the liquid hydrogen target and the P counter.

(ii) 10.2% (TXY cut) was found to be more than 10° of acoplanarity.

(iii) 3.7% (THDIF cut) of events after TXY cut were rejected by $\left| \theta_{\pi}^{*} - \theta_{p}^{*} \right|$ condition.

Events in section (ii) and (iii) were inelastic. In the calculation of differential cross-sections only the above three conditions were finally used to reject inelastic events and events having an interaction outside the liquid hydrogen target.

(b) Normalisation

The normalisation of the elastic events was carried out as follows:

For each run, the momentum distribution of the beam sample events was normalised to ΣP_{π} after correction for the observed inefficiency. After having this information all the runs were combined and stored in a big array, having a bin width of 0.5 MeV/c, and the normalisation factors for the 100 million incident pions for each of the 0.5 MeV/c bin were found out.

All the elastic events were also combined, each having a bin width of 0.5 MeV/c, but still keeping the information of the interaction point in the liquid hydrogen target and the c.m. scattering angle. Normalisation of the elastic events was carried out for each of the 0.5 MeV/c bin width. The error associated for each bin was calculated at this stage from the known number of events and the corresponding normalisation factor of that bin.

For each 0.5 MeV/c, we have for 10^8 incident pions, the number of scattered events in 15 θ^* regions at 75 different points in the liquid hydrogen target. Thus these array represent the yield of elastic events for $10^8\pi$, 0.5 MeV/c bin. Finally, a new binning in the momentum for the normalised elastic events was carried out by correcting for momentum lost in the liquid hydrogen target which is calculated from the known interaction point.

The differential cross-section is calculated from the following formula

$$\left(\frac{d\sigma}{d\Omega}\right) = \frac{\text{Number of elastic events/100m pions X Fac}}{\text{HC X PL X } 10^8 \text{ X } 2\pi} \qquad (6.7a)$$

where HC = hydrogen concentration

= density of hydrogen/weight of one atom of hydrogen

PL = length of the liquid hydrogen target

The factor " Fac " includes the acceptance of the drift chambers system, systematic corrections and the bin width of Cos θ^* of the elastic events. For our experiment, having a length of 20cm liquid hydrogen target and 0.0703 gm/cc for the density of liquid hydrogen, we have,

$$\left(\frac{d\sigma}{d\Omega}\right) = \frac{\text{Number of elastic events/100m pions X Fac}}{84014.0 \text{ X } 2\pi} \text{ mb/sr} \qquad (6.7)$$

The errors associated with the differential cross-sections were calculated in a similar way, but the momentum bin was shifted by -3.0 MeV/c, taking into account the energy loss of the pions in the 10cm of the liquid hydrogen (i.e. calculating the momentum at the centre of the liquid hydrogen target).

(c) Acceptance of drift chambers

A Monte Carlo simulation was made for the acceptance of the drift chambers. The acceptance hardly changes with momentum in the momentum range from 0.600 GeV/c to 0.800 GeV/c. The acceptance calculated at 0.700 GeV/c was used throughout the range of momentum of this experiment. In the range of $\cos\theta^* \simeq -0.44$ to $\cos\theta^* \simeq 0.76$, the acceptance of the drift chamber is approximately 20%, falling to about 13% at $0.76 \leqslant \cos\theta^* \leqslant 0.86$, $-0.64 \leqslant \cos\theta^* \leqslant -0.44$. Data outside these limits was not used.

6.3 Rate effect

Our drift chambers were operated with 25% CH_4 and 75% Ar at a voltage of $\sim$ -12 KV. This gas mixture gives a velocity of $\sim$ 7 cm/μsec in this field and hence we have about 3 μsec memory time for a drift length of 21.4 cm. If a particle enters the drift chamber less than 3 μsec within a particle passes through it, then there is a chance of losing that event. There may be again more events lost in a particular $\cos\theta^*$, where the particle passes near the cathode wire and hence has a longer drift length. This effect on $\cos\theta^*$ dependence may not be very much significant, since our drift chamber system is asymmetric about the beam axis.

In order to investigate these effects on the elastic cross-sections, test data was collected at 0.690 GeV/c, at 20, 35, 50, 65 and 75 K pions/burst. A monitor of the rate was obtained by forming a coincidence between ΣP_π and itself delayed by 200 nsec. In Fig. 6.9(a) we have shown the number of rate monitor events/ 10 K pions as a function of beam pions/ burst. It shows a linear increase of monitor events with beam intensity. The test runs at different beam intensities were also analysed in the same way as the main data. The number of accepted elastic events/ 100 m incident pions as a function of beam intensity is shown in Fig. 6.9(b). The number of elastic events decreases with the increase of beam intensity, which shows a loss of about 6% events at 50K pions/ burst. In order to investigate the rate effect on $\cos\theta^*$, the range of $\cos\theta^*$ which we covered in our experiment ($-0.64 \leqslant \cos\theta^* \leqslant 0.86$) was divided into 5 regions. The number of elastic events for these five $\cos\theta^*$ regions as a function of beam intensity is shown in Fig. 6.10. There is no marked difference between the different regions of $\cos\theta^*$ due to the rate effect.

Since we have observed the rate dependence on elastic events, it is necessary to check the rate monitor events of every run. There are two causes which may affect the number of incident pions/ burst. Firstly, the adjustment of the collimator in the beam line and secondly the length of the target at X_3. In Fig. 6.9(c), we have plotted the number of rate monitor events/ 10 K pions as a function of run number. Data at all these runs was taken at 50K pions/ burst. The scattering of rate monitor events around the mean value (330 events/ 10 K) is quite small and is equivalent to less than $\pm$ 5K pions/ burst. When we combine the rate monitor events for different runs, but having the same momentum, there is much less scattering of rate monitor events around the mean value (Fig. 6.9(d)). A change of $\pm$ 5K pions/ burst corresponds to a change in the accepted elastic events $< \pm 0.6\%$ (Fig. 6.9(b)). Hence we have made no correction from run to run for the fluctuation of beam intensity. A $(6 \pm 1)\%$ correction has been made only in the final differential cross-section for the rate effect.

6.4 Corrections for systematic effects

The following systematic effects were taken into account and used to adjust the values of differential cross-sections by the indicated amount.

(i) $(7 \pm 2)\%$: Contamination of the beam particles other than π^- (mostly μ's). Electrons were rejected by the gas Čerenkov

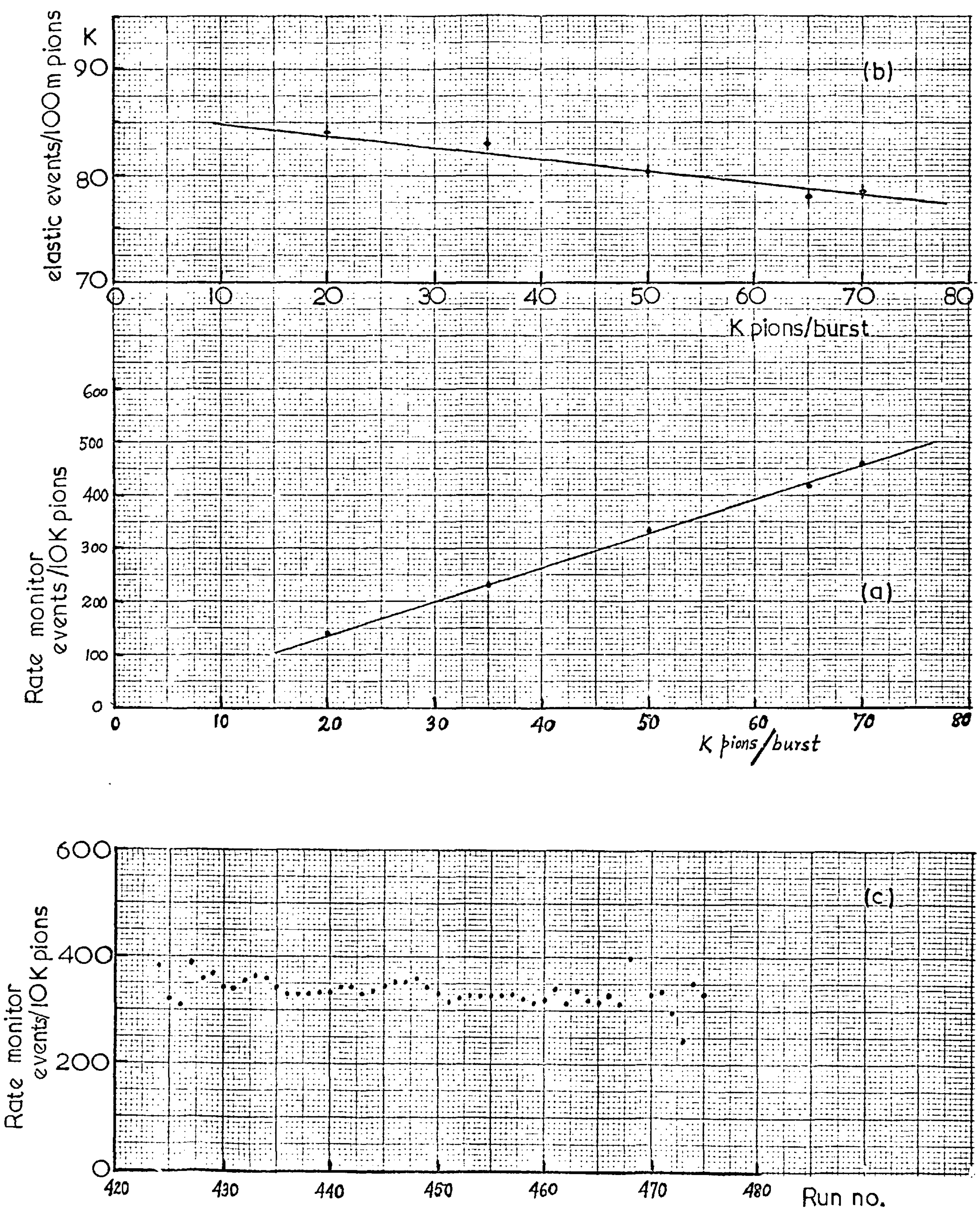
K
elastic events/100m pions
70
80
90
(b)
0
10
20
30
40
50
60
70
80
K pions/burst
Rate monitor
events/10K pions
0
100
200
300
400
500
600
(a)
K pions/burst
Rate monitor
events/10K pions
0
200
400
600
(c)
420
430
440
450
460
470
480
Run no.

FIG. 6.9

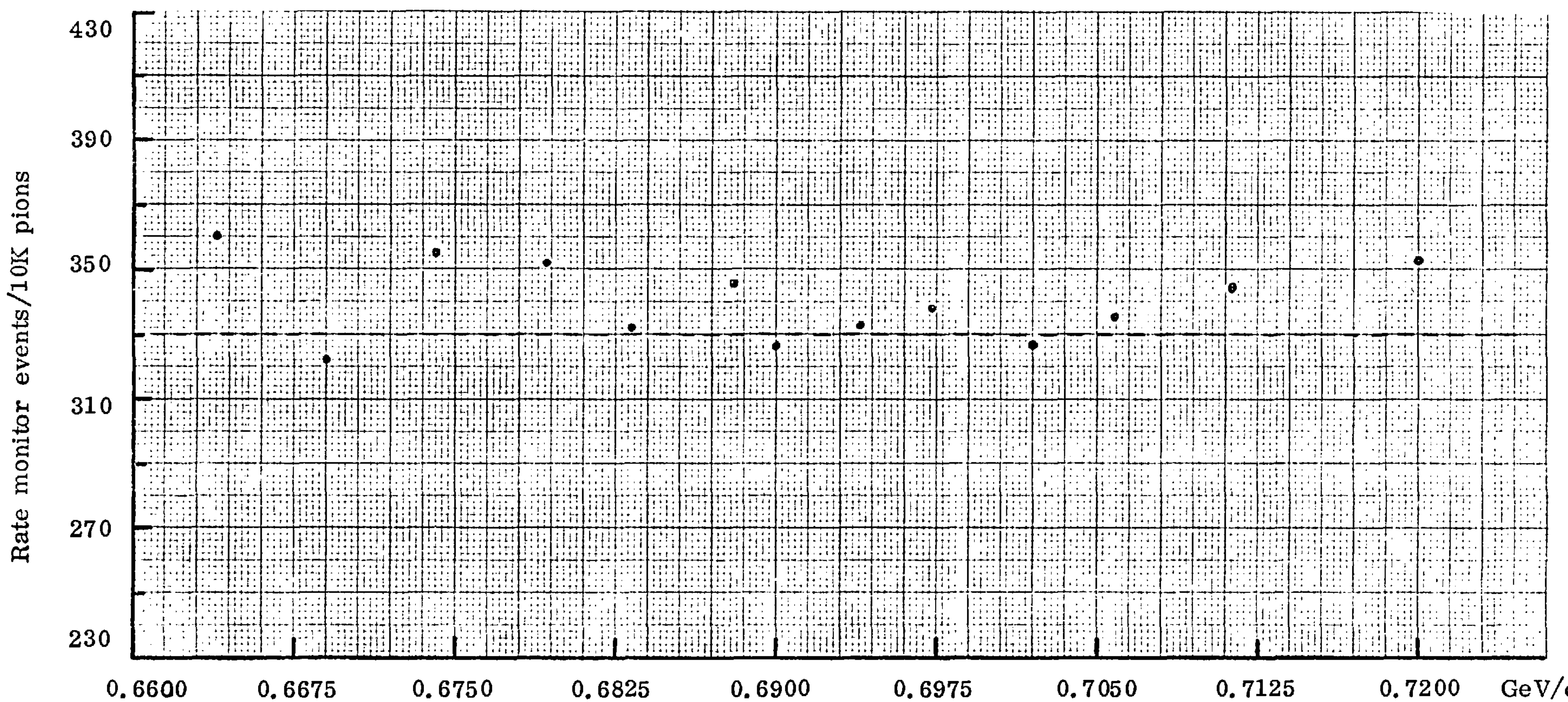
Rate monitor events/10K pions
430
390
350
310
270
230
0.6600
0.6675
0.6750
0.6825
0.6900
0.6975
0.7050
0.7125
0.7200
GeV/c

FIG. 6.9(d)

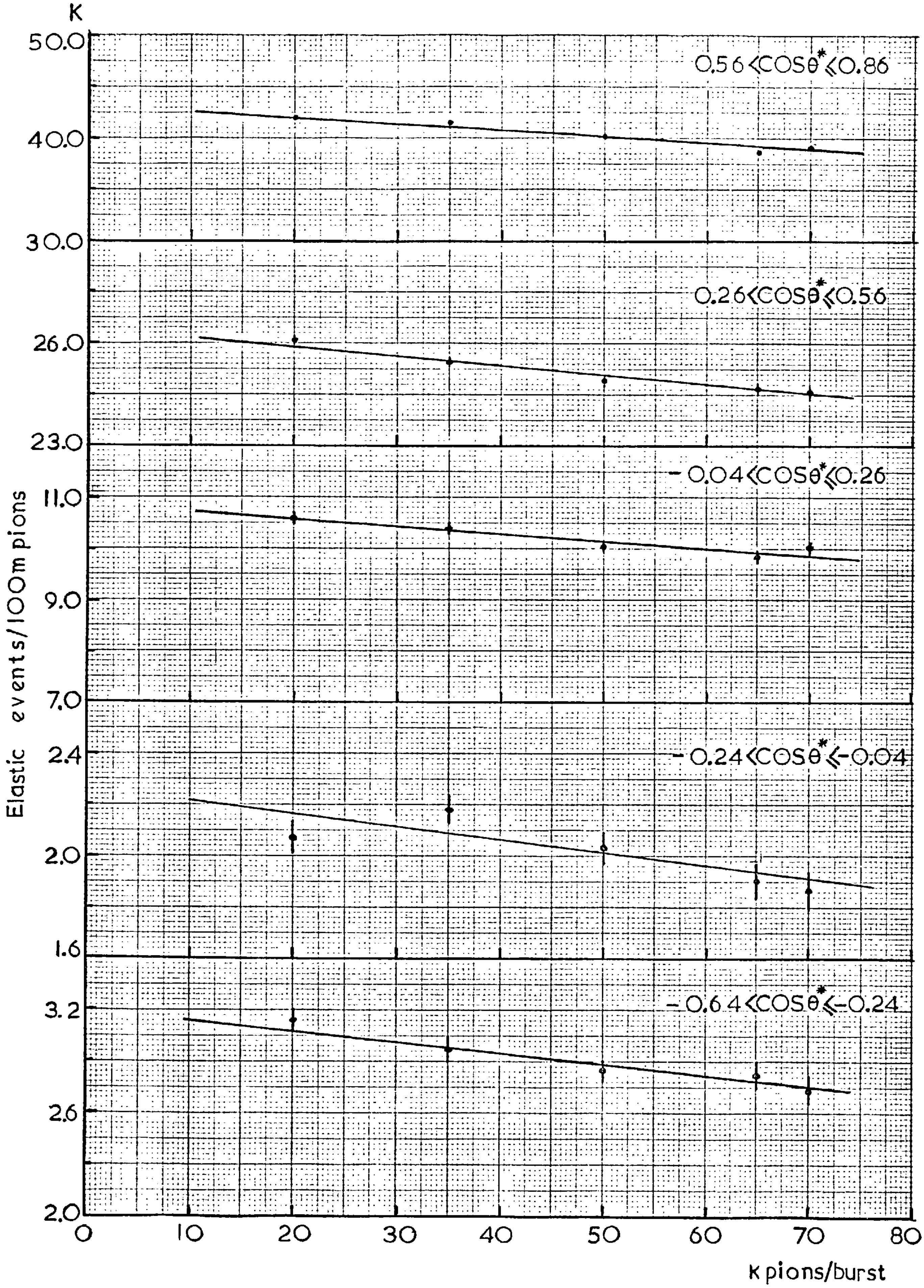
K
50.0
40.0
30.0
26.0
23.0
11.0
9.0
7.0
2.4
2.0
1.6
3.2
2.6
2.0
0
10
20
30
40
50
60
70
80
Elastic events/100m pions
K pions/burst
0.56 ≤ COSθ* ≤ 0.86
0.26 ≤ COSθ* ≤ 0.56
− 0.04 ≤ COSθ* ≤ 0.26
− 0.24 ≤ COSθ* ≤ −0.04
− 0.64 ≤ COSθ* ≤ −0.24

FIG. 6.10

counter .

(ii) (4 $\pm$ 1)% : The pion flux reaching the centre of the liquid hydrogen target was less than recorded owing to absorption in B3, the target walls and the liquid hydrogen target.

(iii) (2 $\pm$ 1)% : Absorption of the recoil protons and the scattered pions in the target.

Non elastic events surviving the various cuts gave a contamination of $<$ 1% and could therefore be ignored.

The above effects lead to a systematic uncertainty in the differential cross-section by 2.6%. The uncertainty of the acceptance of the drift chambers in the range $\cos\theta^* = -0.50$ to $\cos\theta^* = 0.70$ was $\sim \pm$ 2%, while beyond that range it was $\pm$ 4%. In addition there is a $\sim$ 4% systematic error in the different cuts imposed to accept the events as elastic. By quadratically adding the above contributions we obtain a total systematic uncertainty of $\pm$ 5.2% in the range $-0.50 \leqslant \cos\theta^* \leqslant 0.70$, and $\pm$ 6.2% beyond that range of $\cos\theta^*$.

6.5 Differential cross-sections

The systematically corrected differential cross-sections of $\pi^- p$ elastic scattering across the η meson threshold are tabulated in Tables 6.2 (a) - (e). The errors quoted are statistical only.

A comparision has been made between our measured differential cross-sections and that of Brody et al (1971). In the momentum range of 0.660 GeV/c to 0.705 GeV/c, they had two measured differential cross-sections data. Their differential cross-sections at 0.660 GeV/c and 0.700 GeV/c

Table 6.2(a)

$\pi^- p$ elastic scattering differential cross-sections across the threshold for η-production

p_π (GeV/c)	$\left(\frac{d\sigma}{d\Omega}\right)$ mb/sr $\cos\theta^*=-0.59$	$\left(\frac{d\sigma}{d\Omega}\right)$ mb/sr $\cos\theta^*=-0.49$	$\left(\frac{d\sigma}{d\Omega}\right)$ mb/sr $\cos\theta^*=-0.39$
0.6655	0.282 +- 0.024	0.243 +- 0.017	0.160 +- 0.013
0.6665	0.324 +- 0.024	0.238 +- 0.017	0.154 +- 0.012
0.6675	0.322 +- 0.023	0.276 +- 0.017	0.171 +- 0.013
0.6685	0.291 +- 0.022	0.235 +- 0.016	0.152 +- 0.012
0.6695	0.364 +- 0.027	0.229 +- 0.017	0.131 +- 0.012
0.6705	0.350 +- 0.025	0.257 +- 0.017	0.155 +- 0.013
0.6715	0.339 +- 0.021	0.239 +- 0.014	0.153 +- 0.011
0.6725	0.355 +- 0.019	0.251 +- 0.012	0.165 +- 0.010
0.6735	0.336 +- 0.018	0.235 +- 0.012	0.154 +- 0.009
0.6745	0.349 +- 0.019	0.259 +- 0.013	0.168 +- 0.010
0.6755	0.369 +- 0.019	0.251 +- 0.012	0.178 +- 0.010
0.6765	0.348 +- 0.017	0.265 +- 0.012	0.141 +- 0.008
0.6775	0.362 +- 0.017	0.272 +- 0.011	0.157 +- 0.008
0.6785	0.391 +- 0.019	0.248 +- 0.012	0.158 +- 0.009
0.6795	0.403 +- 0.020	0.252 +- 0.013	0.174 +- 0.010
0.6805	0.389 +- 0.018	0.268 +- 0.012	0.155 +- 0.008
0.6815	0.403 +- 0.016	0.257 +- 0.010	0.166 +- 0.007
0.6825	0.406 +- 0.014	0.272 +- 0.009	0.158 +- 0.007
0.6835	0.407 +- 0.013	0.262 +- 0.009	0.167 +- 0.006
0.6845	0.396 +- 0.013	0.269 +- 0.008	0.159 +- 0.006
0.6855	0.408 +- 0.012	0.270 +- 0.008	0.154 +- 0.006
0.6865	0.372 +- 0.011	0.266 +- 0.008	0.162 +- 0.006
0.6875	0.389 +- 0.012	0.248 +- 0.008	0.145 +- 0.006
0.6885	0.392 +- 0.014	0.233 +- 0.008	0.131 +- 0.006
0.6895	0.370 +- 0.015	0.240 +- 0.010	0.135 +- 0.007
0.6905	0.347 +- 0.015	0.246 +- 0.010	0.127 +- 0.007
0.6915	0.356 +- 0.016	0.230 +- 0.010	0.127 +- 0.007
0.6925	0.356 +- 0.018	0.232 +- 0.011	0.124 +- 0.008
0.6935	0.327 +- 0.019	0.229 +- 0.012	0.125 +- 0.009
0.6945	0.343 +- 0.018	0.227 +- 0.012	0.114 +- 0.008
0.6955	0.315 +- 0.017	0.201 +- 0.011	0.113 +- 0.007
0.6965	0.343 +- 0.018	0.201 +- 0.011	0.121 +- 0.008
0.6975	0.337 +- 0.019	0.221 +- 0.012	0.111 +- 0.008
0.6985	0.366 +- 0.021	0.212 +- 0.013	0.122 +- 0.009
0.6995	0.353 +- 0.020	0.212 +- 0.012	0.106 +- 0.008
0.7005	0.355 +- 0.021	0.221 +- 0.013	0.098 +- 0.008
0.7015	0.340 +- 0.023	0.233 +- 0.015	0.102 +- 0.010
0.7025	0.365 +- 0.028	0.224 +- 0.017	0.104 +- 0.011
0.7035	0.348 +- 0.027	0.209 +- 0.017	0.104 +- 0.011
0.7045	0.317 +- 0.024	0.224 +- 0.016	0.099 +- 0.010

Table 6.2 (b)

$\pi^- p$ elastic scattering differential cross-sections across the threshold for η-production

p_π (GeV/c)	$\left(\frac{d\sigma}{d\Omega}\right)_{Cos\theta^*=-0.29}$ mb/sr	$\left(\frac{d\sigma}{d\Omega}\right)_{Cos\theta^*=-0.19}$ mb/sr	$\left(\frac{d\sigma}{d\Omega}\right)_{Cos\theta^*=-0.09}$ mb/sr
0.6655	0.144 +- 0.012	0.147 +- 0.012	0.232 +- 0.015
0.6665	0.136 +- 0.011	0.132 +- 0.011	0.220 +- 0.014
0.6675	0.135 +- 0.011	0.149 +- 0.012	0.222 +- 0.014
0.6685	0.141 +- 0.011	0.136 +- 0.011	0.242 +- 0.014
0.6695	0.123 +- 0.012	0.126 +- 0.012	0.220 +- 0.015
0.6705	0.131 +- 0.011	0.138 +- 0.011	0.225 +- 0.014
0.6715	0.107 +- 0.009	0.133 +- 0.010	0.202 +- 0.012
0.6725	0.131 +- 0.008	0.144 +- 0.009	0.212 +- 0.010
0.6735	0.124 +- 0.008	0.128 +- 0.008	0.231 +- 0.011
0.6745	0.145 +- 0.009	0.130 +- 0.009	0.208 +- 0.011
0.6755	0.117 +- 0.008	0.133 +- 0.008	0.218 +- 0.010
0.6765	0.104 +- 0.007	0.139 +- 0.008	0.204 +- 0.009
0.6775	0.125 +- 0.007	0.117 +- 0.007	0.204 +- 0.009
0.6785	0.113 +- 0.008	0.121 +- 0.008	0.199 +- 0.010
0.6795	0.111 +- 0.008	0.131 +- 0.008	0.199 +- 0.010
0.6805	0.106 +- 0.007	0.120 +- 0.007	0.214 +- 0.010
0.6815	0.110 +- 0.006	0.130 +- 0.007	0.201 +- 0.008
0.6825	0.107 +- 0.005	0.112 +- 0.006	0.196 +- 0.007
0.6835	0.110 +- 0.005	0.126 +- 0.006	0.201 +- 0.007
0.6845	0.105 +- 0.005	0.125 +- 0.005	0.186 +- 0.006
0.6855	0.102 +- 0.004	0.115 +- 0.005	0.209 +- 0.006
0.6865	0.091 +- 0.004	0.111 +- 0.005	0.184 +- 0.006
0.6875	0.089 +- 0.004	0.105 +- 0.005	0.182 +- 0.006
0.6885	0.096 +- 0.005	0.101 +- 0.005	0.198 +- 0.007
0.6895	0.083 +- 0.005	0.107 +- 0.006	0.188 +- 0.008
0.6905	0.079 +- 0.005	0.105 +- 0.006	0.179 +- 0.008
0.6915	0.078 +- 0.006	0.097 +- 0.006	0.205 +- 0.009
0.6925	0.066 +- 0.006	0.093 +- 0.007	0.185 +- 0.010
0.6935	0.074 +- 0.007	0.095 +- 0.007	0.179 +- 0.010
0.6945	0.067 +- 0.006	0.094 +- 0.007	0.174 +- 0.010
0.6955	0.073 +- 0.006	0.088 +- 0.007	0.179 +- 0.009
0.6965	0.070 +- 0.006	0.093 +- 0.007	0.180 +- 0.009
0.6975	0.074 +- 0.007	0.091 +- 0.007	0.184 +- 0.010
0.6985	0.065 +- 0.007	0.091 +- 0.008	0.195 +- 0.011
0.6995	0.064 +- 0.007	0.096 +- 0.008	0.199 +- 0.011
0.7005	0.082 +- 0.007	0.086 +- 0.008	0.189 +- 0.011
0.7015	0.061 +- 0.007	0.084 +- 0.009	0.162 +- 0.012
0.7025	0.072 +- 0.009	0.110 +- 0.011	0.204 +- 0.015
0.7035	0.067 +- 0.009	0.098 +- 0.011	0.176 +- 0.014
0.7045	0.067 +- 0.008	0.090 +- 0.010	0.189 +- 0.014

Table 6.2(c)

$\bar{\pi} p$ elastic scattering differential cross-sections across the threshold for η-production

p_π (GeV/c)	$\left(\frac{d\sigma}{d\Omega}\right)_{\cos\theta^*=0.01}$ mb/sr	$\left(\frac{d\sigma}{d\Omega}\right)_{\cos\theta^*=0.11}$ mb/sr	$\left(\frac{d\sigma}{d\Omega}\right)_{\cos\theta^*=0.21}$ mb/sr
0.6655	0.353 +- 0.019	0.532 +- 0.022	0.829 +- 0.026
0.6665	0.343 +- 0.017	0.536 +- 0.021	0.791 +- 0.024
0.6675	0.364 +- 0.017	0.528 +- 0.020	0.797 +- 0.023
0.6685	0.376 +- 0.018	0.550 +- 0.021	0.807 +- 0.023
0.6695	0.352 +- 0.019	0.567 +- 0.023	0.770 +- 0.025
0.6705	0.325 +- 0.017	0.538 +- 0.021	0.827 +- 0.024
0.6715	0.355 +- 0.015	0.527 +- 0.018	0.803 +- 0.021
0.6725	0.337 +- 0.013	0.529 +- 0.016	0.814 +- 0.018
0.6735	0.318 +- 0.013	0.500 +- 0.015	0.801 +- 0.018
0.6745	0.359 +- 0.014	0.544 +- 0.016	0.798 +- 0.017
0.6755	0.364 +- 0.013	0.566 +- 0.016	0.797 +- 0.016
0.6765	0.352 +- 0.012	0.534 +- 0.016	0.809 +- 0.016
0.6775	0.333 +- 0.011	0.522 +- 0.014	0.826 +- 0.016
0.6785	0.346 +- 0.012	0.527 +- 0.014	0.796 +- 0.017
0.6795	0.345 +- 0.013	0.529 +- 0.015	0.806 +- 0.018
0.6805	0.331 +- 0.012	0.510 +- 0.014	0.827 +- 0.016
0.6815	0.341 +- 0.010	0.506 +- 0.012	0.794 +- 0.014
0.6825	0.333 +- 0.009	0.535 +- 0.011	0.822 +- 0.013
0.6835	0.336 +- 0.008	0.508 +- 0.010	0.816 +- 0.012
0.6845	0.338 +- 0.008	0.546 +- 0.010	0.827 +- 0.011
0.6855	0.327 +- 0.008	0.520 +- 0.009	0.828 +- 0.011
0.6865	0.334 +- 0.008	0.537 +- 0.009	0.846 +- 0.011
0.6875	0.338 +- 0.008	0.538 +- 0.010	0.840 +- 0.011
0.6885	0.334 +- 0.009	0.546 +- 0.011	0.856 +- 0.013
0.6895	0.316 +- 0.010	0.533 +- 0.012	0.839 +- 0.014
0.6905	0.342 +- 0.010	0.546 +- 0.013	0.855 +- 0.015
0.6915	0.322 +- 0.010	0.539 +- 0.013	0.871 +- 0.015
0.6925	0.347 +- 0.013	0.544 +- 0.015	0.870 +- 0.018
0.6935	0.348 +- 0.014	0.553 +- 0.016	0.870 +- 0.019
0.6945	0.317 +- 0.013	0.537 +- 0.016	0.864 +- 0.018
0.6955	0.340 +- 0.012	0.538 +- 0.015	0.880 +- 0.017
0.6965	0.334 +- 0.012	0.597 +- 0.016	0.894 +- 0.018
0.6975	0.345 +- 0.014	0.538 +- 0.016	0.866 +- 0.019
0.6985	0.341 +- 0.014	0.578 +- 0.018	0.911 +- 0.021
0.6995	0.334 +- 0.014	0.557 +- 0.017	0.896 +- 0.020
0.7005	0.343 +- 0.014	0.555 +- 0.018	0.864 +- 0.020
0.7015	0.355 +- 0.017	0.601 +- 0.021	0.872 +- 0.024
0.7025	0.335 +- 0.019	0.591 +- 0.024	0.916 +- 0.028
0.7035	0.346 +- 0.019	0.569 +- 0.024	0.881 +- 0.027
0.7045	0.355 +- 0.018	0.599 +- 0.023	0.875 +- 0.026

Table 6.2 (d)

$\pi^- p$ elastic scattering differential cross-sections across the threshold for η -production

p_π (GeV/c)	$\left(\frac{d\sigma}{d\Omega}\right)_{\cos\theta^*=0.31}$ mb/sr	$\left(\frac{d\sigma}{d\Omega}\right)_{\cos\theta^*=0.41}$ mb/sr	$\left(\frac{d\sigma}{d\Omega}\right)_{\cos\theta^*=0.51}$ mb/sr
0.6655	1.123 +- 0.031	1.242 +- 0.033	1.583 +- 0.039
0.6665	1.116 +- 0.029	1.287 +- 0.032	1.651 +- 0.038
0.6675	1.102 +- 0.028	1.224 +- 0.030	1.602 +- 0.036
0.6685	1.144 +- 0.028	1.284 +- 0.031	1.646 +- 0.036
0.6695	1.134 +- 0.031	1.327 +- 0.035	1.653 +- 0.040
0.6705	1.137 +- 0.029	1.324 +- 0.033	1.644 +- 0.038
0.6715	1.168 +- 0.025	1.315 +- 0.028	1.752 +- 0.033
0.6725	1.139 +- 0.022	1.282 +- 0.023	1.621 +- 0.027
0.6735	1.139 +- 0.022	1.254 +- 0.023	1.635 +- 0.027
0.6745	1.150 +- 0.023	1.263 +- 0.024	1.694 +- 0.029
0.6755	1.186 +- 0.022	1.250 +- 0.023	1.683 +- 0.028
0.6765	1.146 +- 0.022	1.312 +- 0.021	1.679 +- 0.025
0.6775	1.151 +- 0.020	1.295 +- 0.021	1.675 +- 0.025
0.6785	1.119 +- 0.019	1.282 +- 0.022	1.700 +- 0.027
0.6795	1.148 +- 0.022	1.316 +- 0.024	1.742 +- 0.028
0.6805	1.165 +- 0.020	1.326 +- 0.022	1.721 +- 0.026
0.6815	1.175 +- 0.017	1.291 +- 0.018	1.746 +- 0.022
0.6825	1.177 +- 0.015	1.325 +- 0.017	1.769 +- 0.020
0.6835	1.159 +- 0.014	1.340 +- 0.016	1.803 +- 0.019
0.6845	1.212 +- 0.014	1.360 +- 0.015	1.786 +- 0.018
0.6855	1.198 +- 0.014	1.399 +- 0.014	1.830 +- 0.017
0.6865	1.192 +- 0.013	1.405 +- 0.014	1.847 +- 0.017
0.6875	1.226 +- 0.013	1.406 +- 0.015	1.852 +- 0.018
0.6885	1.189 +- 0.015	1.390 +- 0.017	1.880 +- 0.021
0.6895	1.244 +- 0.018	1.367 +- 0.019	1.896 +- 0.023
0.6905	1.209 +- 0.018	1.441 +- 0.020	1.923 +- 0.024
0.6915	1.225 +- 0.019	1.406 +- 0.021	1.933 +- 0.025
0.6925	1.253 +- 0.022	1.424 +- 0.024	1.955 +- 0.029
0.6935	1.229 +- 0.023	1.434 +- 0.026	1.960 +- 0.031
0.6945	1.217 +- 0.022	1.534 +- 0.026	2.001 +- 0.030
0.6955	1.245 +- 0.021	1.421 +- 0.023	1.921 +- 0.028
0.6965	1.269 +- 0.022	1.460 +- 0.024	1.981 +- 0.029
0.6975	1.277 +- 0.024	1.450 +- 0.026	1.969 +- 0.032
0.6985	1.273 +- 0.025	1.478 +- 0.028	2.016 +- 0.034
0.6995	1.284 +- 0.025	1.502 +- 0.027	2.022 +- 0.033
0.7005	1.269 +- 0.025	1.434 +- 0.027	1.950 +- 0.033
0.7015	1.252 +- 0.029	1.523 +- 0.033	1.926 +- 0.038
0.7025	1.250 +- 0.034	1.465 +- 0.037	2.028 +- 0.046
0.7035	1.242 +- 0.033	1.509 +- 0.037	2.048 +- 0.046
0.7045	1.238 +- 0.031	1.514 +- 0.035	1.987 +- 0.042

Table 6.2(e)

$\pi^- p$ elastic scattering differential cross-sections across the threshold for η-production

p_π (GeV/c)	$\left(\frac{d\sigma}{d\Omega}\right)_{\cos\theta^*=0.61}$ mb/sr	$\left(\frac{d\sigma}{d\Omega}\right)_{\cos\theta^*=0.71}$ mb/sr	$\left(\frac{d\sigma}{d\Omega}\right)_{\cos\theta^*=0.81}$ mb/sr
0.6655	2.010 +- 0.044	2.476 +- 0.049	2.764 +- 0.065
0.6665	2.135 +- 0.043	2.530 +- 0.047	2.819 +- 0.063
0.6675	2.030 +- 0.040	2.632 +- 0.046	2.844 +- 0.061
0.6685	2.027 +- 0.040	2.701 +- 0.047	2.914 +- 0.062
0.6695	2.123 +- 0.046	2.584 +- 0.051	2.846 +- 0.067
0.6705	2.141 +- 0.043	2.547 +- 0.047	2.992 +- 0.065
0.6715	2.028 +- 0.036	2.637 +- 0.041	3.040 +- 0.054
0.6725	2.173 +- 0.032	2.645 +- 0.035	3.009 +- 0.048
0.6735	2.146 +- 0.032	2.666 +- 0.035	3.077 +- 0.051
0.6745	2.139 +- 0.033	2.681 +- 0.037	3.148 +- 0.049
0.6755	2.203 +- 0.032	2.701 +- 0.035	3.211 +- 0.045
0.6765	2.257 +- 0.029	2.779 +- 0.033	3.309 +- 0.044
0.6775	2.188 +- 0.028	2.786 +- 0.032	3.306 +- 0.044
0.6785	2.253 +- 0.031	2.818 +- 0.035	3.379 +- 0.048
0.6795	2.278 +- 0.033	2.799 +- 0.036	3.337 +- 0.051
0.6805	2.340 +- 0.029	2.899 +- 0.033	3.413 +- 0.046
0.6815	2.333 +- 0.026	2.875 +- 0.029	3.529 +- 0.041
0.6825	2.316 +- 0.023	2.863 +- 0.024	3.476 +- 0.036
0.6835	2.342 +- 0.022	2.957 +- 0.024	3.531 +- 0.034
0.6845	2.332 +- 0.021	3.004 +- 0.022	3.675 +- 0.033
0.6855	2.396 +- 0.020	3.029 +- 0.022	3.681 +- 0.031
0.6865	2.439 +- 0.020	3.016 +- 0.023	3.837 +- 0.031
0.6875	2.466 +- 0.021	3.041 +- 0.023	3.946 +- 0.033
0.6885	2.492 +- 0.023	3.123 +- 0.027	3.959 +- 0.037
0.6895	2.488 +- 0.026	3.111 +- 0.030	3.915 +- 0.042
0.6905	2.475 +- 0.027	3.107 +- 0.031	4.029 +- 0.044
0.6915	2.485 +- 0.028	3.136 +- 0.032	4.021 +- 0.046
0.6925	2.511 +- 0.033	3.175 +- 0.037	4.106 +- 0.053
0.6935	2.582 +- 0.036	3.219 +- 0.040	4.148 +- 0.058
0.6945	2.527 +- 0.034	3.226 +- 0.039	4.159 +- 0.056
0.6955	2.586 +- 0.033	3.207 +- 0.036	4.198 +- 0.053
0.6965	2.549 +- 0.033	3.261 +- 0.037	4.142 +- 0.053
0.6975	2.663 +- 0.037	3.295 +- 0.041	4.244 +- 0.060
0.6985	2.528 +- 0.038	3.256 +- 0.043	4.369 +- 0.064
0.6995	2.590 +- 0.038	3.326 +- 0.043	4.422 +- 0.063
0.7005	2.671 +- 0.039	3.301 +- 0.044	4.392 +- 0.064
0.7015	2.660 +- 0.045	3.304 +- 0.051	4.501 +- 0.075
0.7025	2.666 +- 0.053	3.341 +- 0.059	4.543 +- 0.087
0.7035	2.723 +- 0.055	3.356 +- 0.059	4.530 +- 0.087
0.7045	2.728 +- 0.049	3.286 +- 0.055	4.468 +- 0.081

are shown in Fig. 6.11 (c). The smooth curves represent their fit to the data points by an expansion in Legendre polynomials.

Our measured differential cross-sections $\left(\frac{d\sigma}{d\Omega}\right)$ were expanded in terms of the Legendre polynomials $P_l(\mathrm{Cos}\,\theta^*)$ as,

$$\left(\frac{d\sigma}{d\Omega}\right)= \sum_{l=0}^{l_{max}} C_l P_l(\mathrm{Cos}\,\theta^*) \qquad (6.8)$$

where θ^* is the c.m. scattering angle. Values of coefficients C_l were obtained from a minimum χ^2 fitting programme. The expansions were made in terms of the function $P_l(\mathrm{Cos}\,\theta^*)$ rather than $\mathrm{Cos}^l\,\theta^*$ on account of the smaller correlation among the expansion coefficients. The minimum χ^2 was searched for the coefficients C_l's by the programme. Upto l=4th order was sufficient to fit the data. Inclusion of l=5th order did not improve χ^2 and did not cause significant changes in the values of the coefficients obtained from the lower order fit. Fittings of the angular distributions were made for 1.0 MeV/c bin of momentum. In Figs. 6.11 (a) and (b), we have presented some of our elastic angular distributions. The smooth curves superposed on the data represent the fit to the data points. We compare our angular distributions at 0.6635 GeV/c and 0.7005 GeV/c respectively to the angular distributions at 0.660 GeV/c and 0.700 GeV/c of Brody. In the range of $\mathrm{Cos}\,\theta^*$ which we covered in our experiment, the agreement between our measured differential cross-sections is very good.

The values of the Legendre polynomial coefficients C_l as a function of momentum are tabulated in Tables 6.3 (a) and (b). The error quoted corresponds to a change of χ^2 of one. The coefficients C_l's are plotted in Fig. 6.12. It is of some interest that there is no evidence for the $\sim$36 MeV wide N^* suggested in the Glasgow solution (Davies 1970).

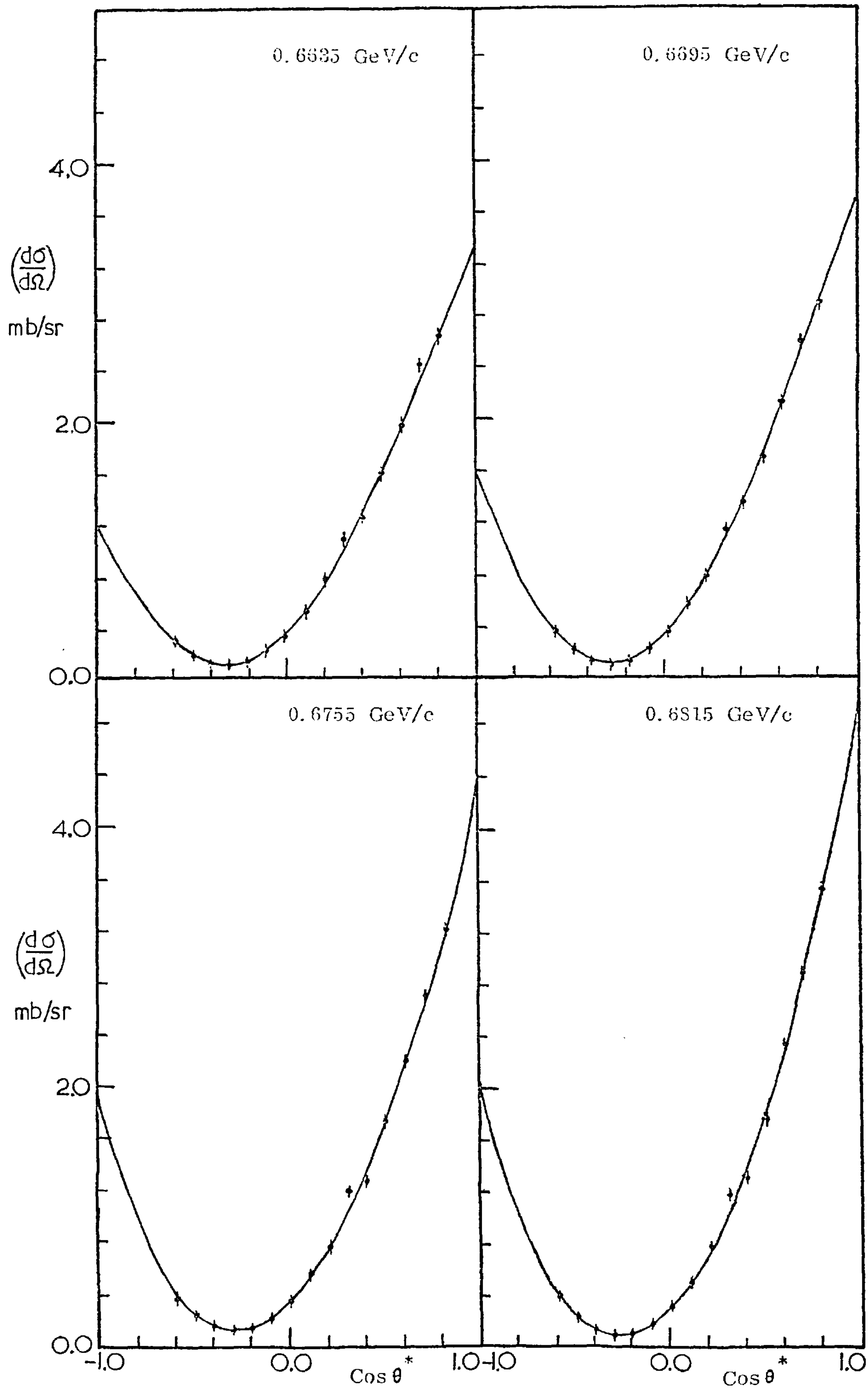

FIG. 6.11(a) Differential cross-sections for $\pi^- p$ elastic scattering.

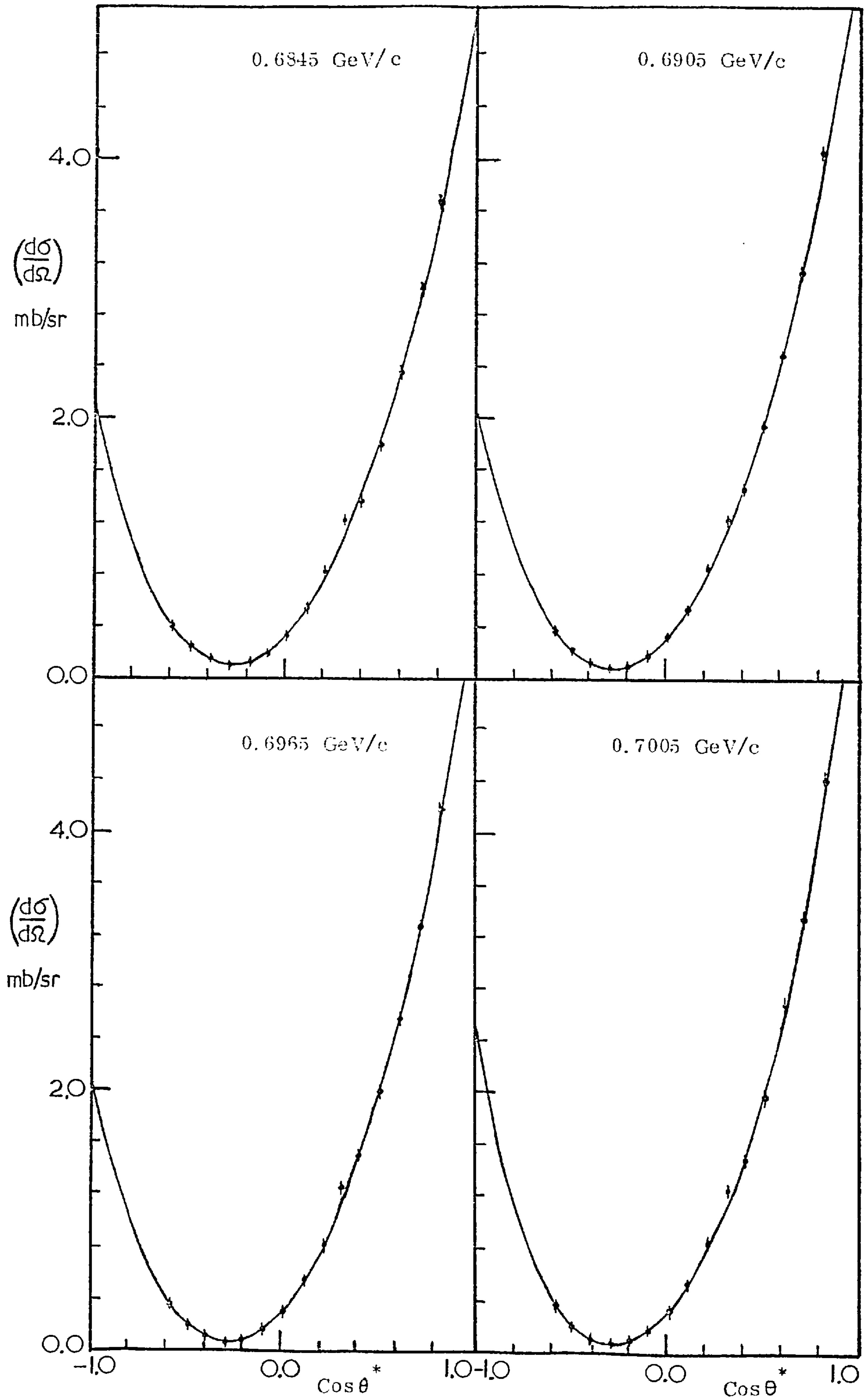

FIG. 6.11(b) Differential cross-sections for π^-p elastic scattering.

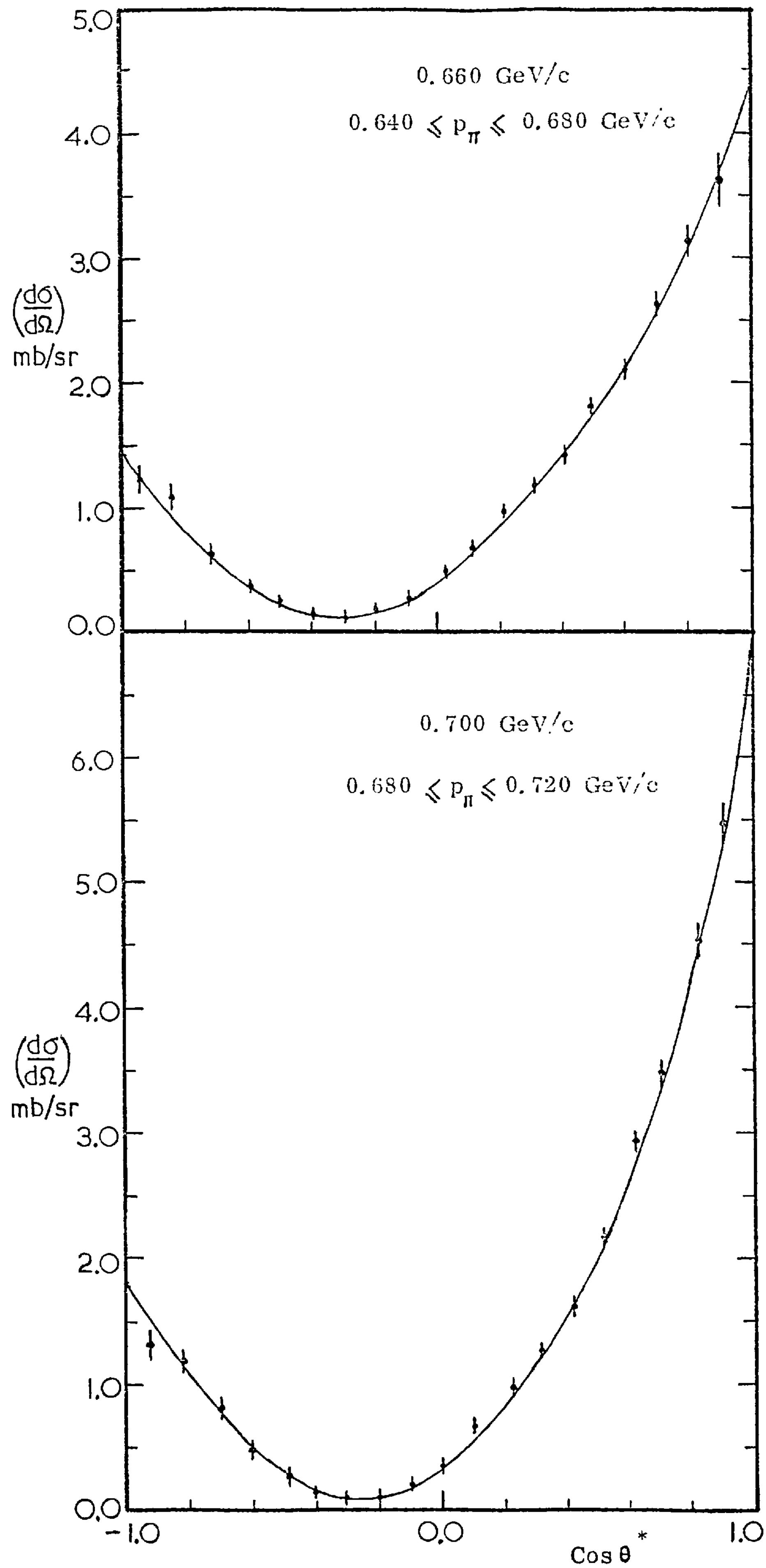

FIG. 6.11(c) The differential cross-sections for $\pi^- p$ elastic scattering. The smooth curves represent the best fit by an expansion in Legendre polynomials (Brody et al 1971).

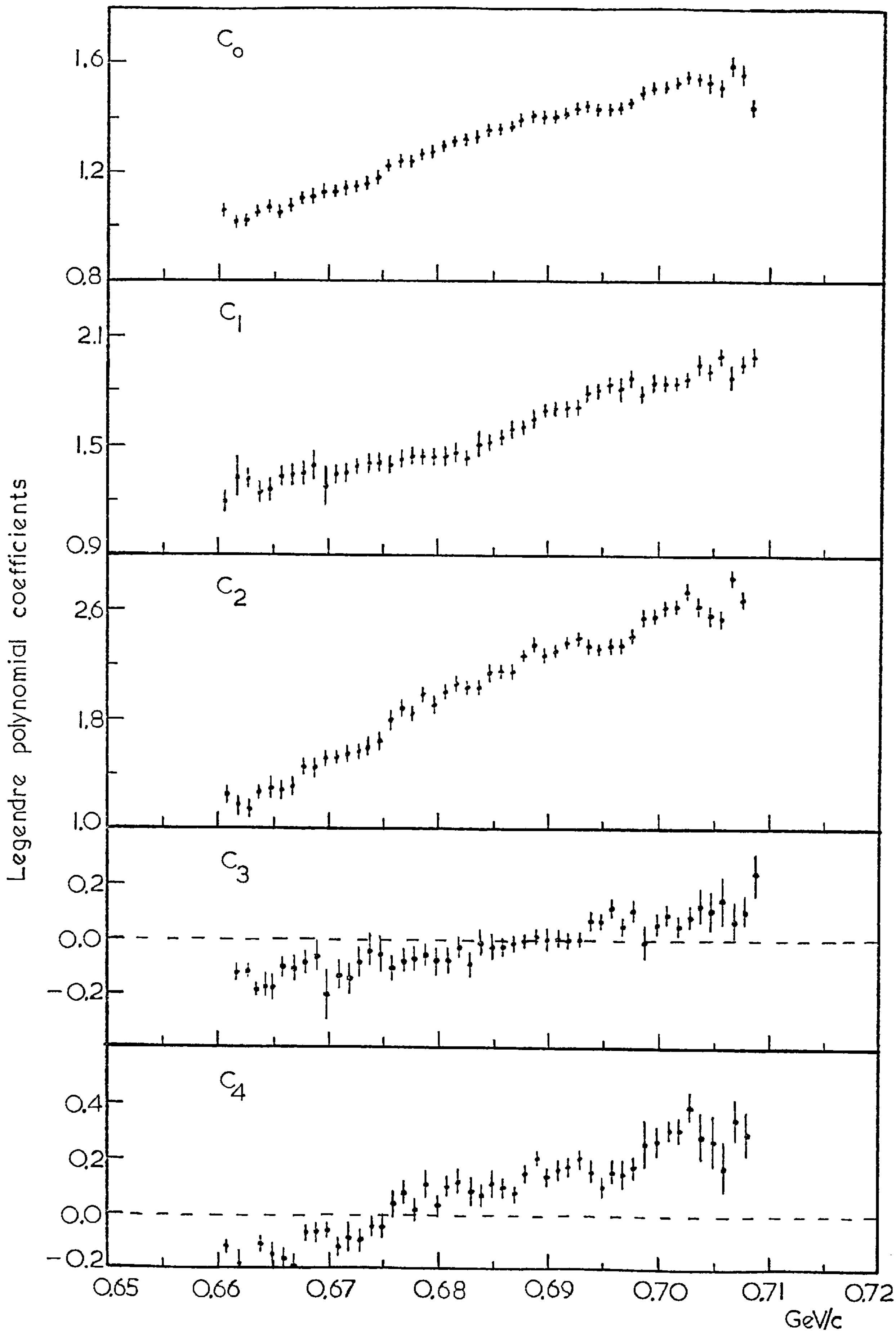

FIG. 6.12 Coefficients of the Legendre polynomial expansions for $\pi^- p$ elastic scattering.

Table 6.3(a)

Legendre polynomial coefficients $\left(\frac{d\sigma}{d\Omega}\right) = \sum_{l=0}^{l_{max}} C_l P_l(\cos\theta^*)$

p_π (GeV/c)	C_o	C_1	C_2	C_3	C_4
0.6605	1.071+-0.019	1.207+-0.040	1.280+-0.018	-0.249+-0.019	-0.116+-0.029
0.6615	1.022+-0.020	1.342+-0.154	1.193+-0.107	-0.099+-0.179	-0.203+-0.167
0.6625	1.021+-0.017	1.326+-0.014	1.177+-0.023	-0.091+-0.015	-0.246+-0.026
0.6635	1.047+-0.015	1.234+-0.018	1.306+-0.018	-0.179+-0.034	-0.107+-0.028
0.6645	1.068+-0.026	1.256+-0.060	1.353+-0.105	-0.167+-0.067	-0.154+-0.082
0.6655	1.041+-0.029	1.347+-0.057	1.261+-0.114	-0.071+-0.038	-0.164+-0.074
0.6665	1.072+-0.027	1.366+-0.056	1.334+-0.078	-0.092+-0.056	-0.193+-0.065
0.6675	1.112+-0.017	1.330+-0.058	1.489+-0.083	-0.066+-0.043	-0.069+-0.048
0.6685	1.114+-0.027	1.410+-0.087	1.466+-0.068	-0.055+-0.062	-0.069+-0.055
0.6695	1.139+-0.022	1.274+-0.161	1.546+-0.057	-0.206+-0.179	-0.062+-0.036
0.6705	1.134+-0.019	1.337+-0.052	1.509+-0.052	-0.127+-0.050	-0.108+-0.036
0.6715	1.149+-0.025	1.351+-0.087	1.569+-0.078	-0.142+-0.126	-0.079+-0.069
0.6725	1.150+-0.017	1.378+-0.045	1.575+-0.032	-0.074+-0.044	-0.074+-0.040
0.6735	1.152+-0.018	1.422+-0.059	1.623+-0.097	-0.026+-0.097	-0.037+-0.040
0.6745	1.178+-0.030	1.411+-0.087	1.656+-0.051	-0.046+-0.080	-0.037+-0.037
0.6755	1.236+-0.017	1.360+-0.060	1.833+-0.072	-0.112+-0.037	0.073+-0.088
0.6765	1.254+-0.020	1.431+-0.054	1.901+-0.035	-0.073+-0.033	0.089+-0.072
0.6775	1.239+-0.019	1.422+-0.047	1.853+-0.069	-0.059+-0.047	0.035+-0.057
0.6785	1.284+-0.019	1.426+-0.036	2.014+-0.041	-0.054+-0.035	0.132+-0.051
0.6795	1.266+-0.019	1.431+-0.057	1.906+-0.060	-0.073+-0.036	0.041+-0.048
0.6805	1.299+-0.018	1.439+-0.056	2.025+-0.041	-0.073+-0.065	0.108+-0.043
0.6815	1.316+-0.017	1.495+-0.052	2.079+-0.057	-0.010+-0.041	0.129+-0.058
0.6825	1.314+-0.015	1.437+-0.032	2.043+-0.040	-0.098+-0.040	0.084+-0.088
0.6835	1.317+-0.016	1.537+-0.073	2.042+-0.039	-0.002+-0.048	0.069+-0.042
0.6845	1.358+-0.014	1.535+-0.033	2.160+-0.056	-0.032+-0.065	0.133+-0.085

Table 6.3 (b)

Legendre polynomial coefficient $\left(\frac{d\sigma}{d\Omega}\right) = \sum_{l=0}^{l_{max}} C_l P_l(\cos\theta^*)$

p_π (GeV/c)	C_o	C_1	C_2	C_3	C_4
0.6855	1.364+-0.015	1.564+-0.020	2.159+-0.015	-0.027+-0.020	0.104+-0.033
0.6865	1.365+-0.014	1.634+-0.022	2.155+-0.020	0.013+-0.031	0.083+-0.022
0.6875	1.407+-0.015	1.629+-0.017	2.296+-0.010	-0.008+-0.033	0.167+-0.020
0.6885	1.431+-0.015	1.668+-0.028	2.376+-0.012	0.021+-0.020	0.226+-0.015
0.6895	1.395+-0.014	1.696+-0.027	2.261+-0.020	0.041+-0.023	0.142+-0.022
0.6905	1.406+-0.013	1.723+-0.030	2.276+-0.013	0.035+-0.030	0.147+-0.030
0.6915	1.419+-0.014	1.720+-0.037	2.323+-0.025	0.030+-0.024	0.181+-0.026
0.6925	1.449+-0.017	1.721+-0.020	2.403+-0.036	0.001+-0.028	0.208+-0.046
0.6935	1.429+-0.018	1.832+-0.040	2.326+-0.031	0.095+-0.031	0.150+-0.038
0.6945	1.421+-0.017	1.835+-0.021	2.288+-0.020	0.074+-0.015	0.095+-0.017
0.6955	1.423+-0.018	1.861+-0.015	2.335+-0.042	0.120+-0.034	0.171+-0.069
0.6965	1.442+-0.022	1.811+-0.090	2.339+-0.035	0.037+-0.034	0.158+-0.076
0.6975	1.463+-0.018	1.884+-0.034	2.417+-0.034	0.114+-0.032	0.181+-0.042
0.6985	1.515+-0.022	1.773+-0.031	2.568+-0.068	-0.001+-0.084	0.289+-0.109
0.6995	1.521+-0.019	1.860+-0.074	2.584+-0.060	0.066+-0.032	0.286+-0.070
0.7005	1.519+-0.017	1.859+-0.021	2.615+-0.037	0.103+-0.041	0.313+-0.035
0.7015	1.534+-0.018	1.844+-0.018	2.644+-0.027	0.055+-0.039	0.304+-0.037
0.7025	1.576+-0.016	1.864+-0.022	2.753+-0.022	0.081+-0.041	0.401+-0.073
0.7035	1.534+-0.019	1.952+-0.077	2.617+-0.066	0.139+-0.074	0.277+-0.138
0.7045	1.513+-0.027	1.914+-0.029	2.555+-0.067	0.105+-0.081	0.268+-0.141
0.7055	1.496+-0.030	2.006+-0.037	2.497+-0.173	0.179+-0.100	0.186+-0.126
0.7065	1.610+-0.022	1.856+-0.118	2.856+-0.056	0.050+-0.109	0.389+-0.083
0.7075	1.587+-0.025	1.946+-0.052	2.773+-0.053	0.120+-0.063	0.298+-0.081
0.7085	1.444+-0.021	2.098+-0.056	2.324+-0.039	0.289+-0.090	0.039+-0.064

7. Cusp

7.1 Cusp in $\pi^- p$ elastic scattering differential cross-sections.

When the differential cross-section for $\pi^- p$ elastic scattering is plotted as a function of pion momentum for each $\cos\theta^*$ bin (Figs. 7.1(a), (b) and (c)), a very clear cusp is observed near the threshold for η meson production. The continuous curves are hand drawn and not fits to the data points. Taking the mass of η meson, $m_\eta = 548.8 \pm 0.6$ MeV as given by Particle Data Group (1976), we have $p_\pi = 0.687 \pm 0.0012$ GeV/c for the threshold for η -production. This value is comparable to our $p_\pi = 0.6855 \pm 0.0005$ GeV/c, where we have observed cusp. Recent measurements of the η mass by Binnie et al (1973) gave a value of $m_\eta = 548.1 \pm 0.40$ MeV, giving the threshold for η-production as, $p_\pi = 0.6858 \pm 0.0008$ GeV/c. This value is in good agreement with the π^- momentum where the cusp occurs. Thus the cusp is due to the opening of the $\pi^- p \rightarrow \eta\, n$ channel. The shape of the cusp shows a variation with $\cos\theta^*$. The magnitude and shape of the cusp depend on the followings (Chapter 2)

(i) $\sigma_{reac}(|K_1|)$: The production cross-section for $\pi^- p \rightarrow \eta\, n$.

(ii) $|f(\theta^*, K)|$: The non-spin flip amplitude.

(iii) $\sin(2\delta_o - \alpha(\theta^*))$
$\cos(2\delta_o - \alpha(\theta^*))$
where $(2\delta_o - \alpha(\theta^*))$ is the relative phase of the S_{11} wave and the non-spin flip amplitude $f(\theta^*, K)$.

Thus at $\cos\theta^* = -0.59$ (Fig. 7.1(a)), the shape of the cusp indicates that $(2\delta_o - \alpha(\theta^*))$ is in the first quadrant, whereas at $\cos\theta^* = 0.31$ (Fig. 7.1(c)), $(2\delta_o - \alpha(\theta^*))$ lies in the fourth quadrant.

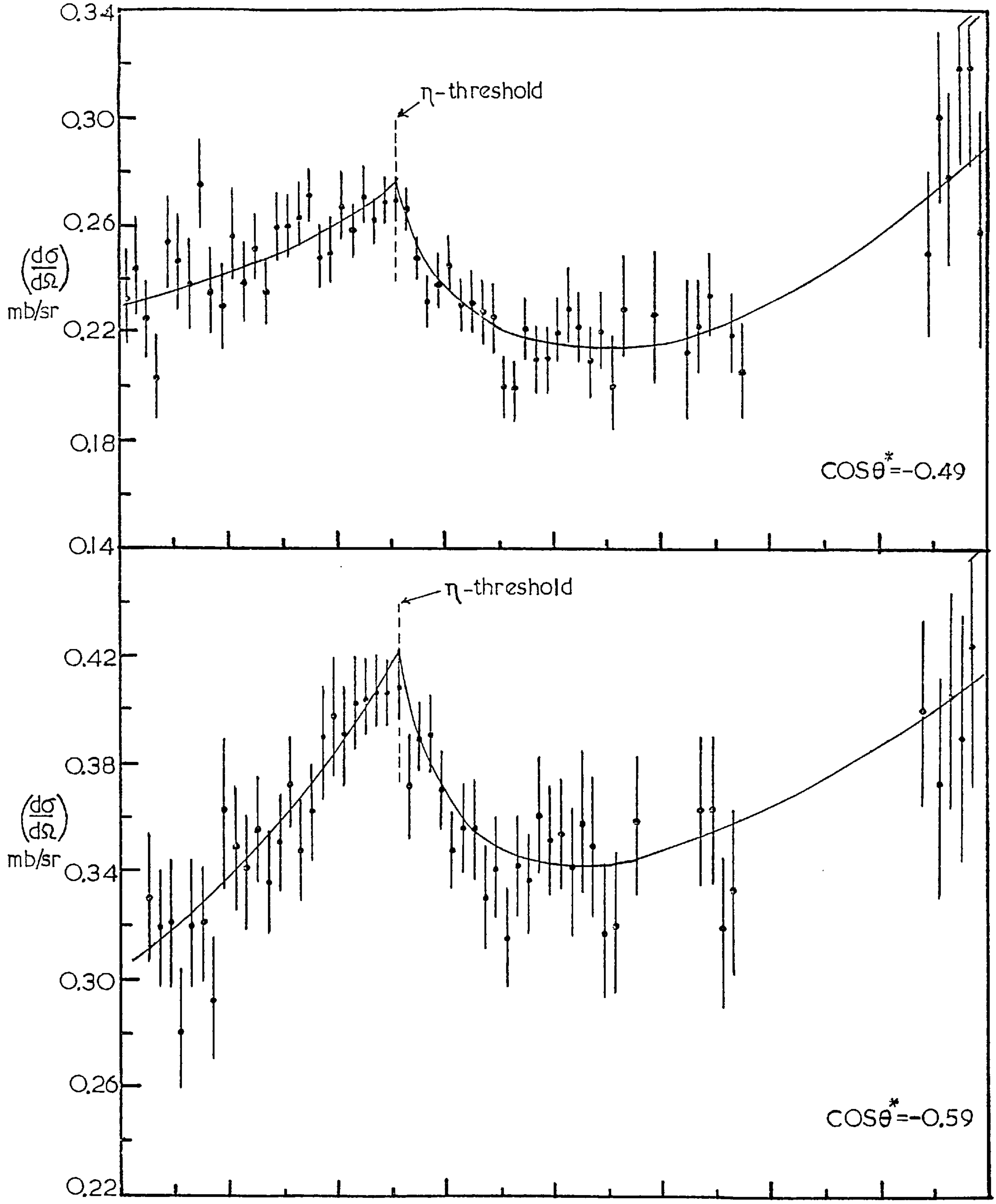

FIG. 7.1(a) $\pi^- p$ elastic scattering differential cross-sections near η-production threshold.

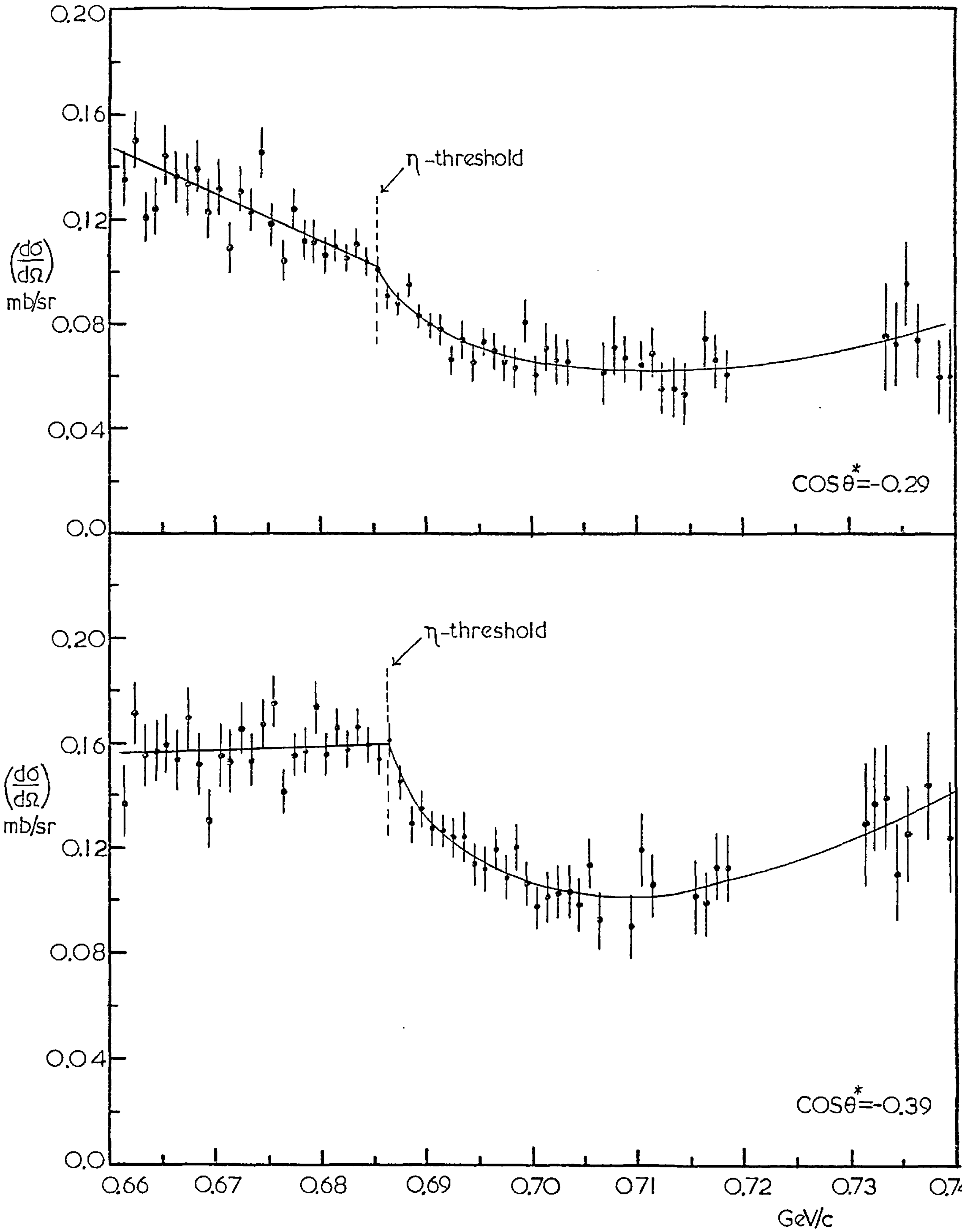

FIG. 7.1(b) $\pi^- p$ elastic scattering differential cross-sections near η-production threshold.

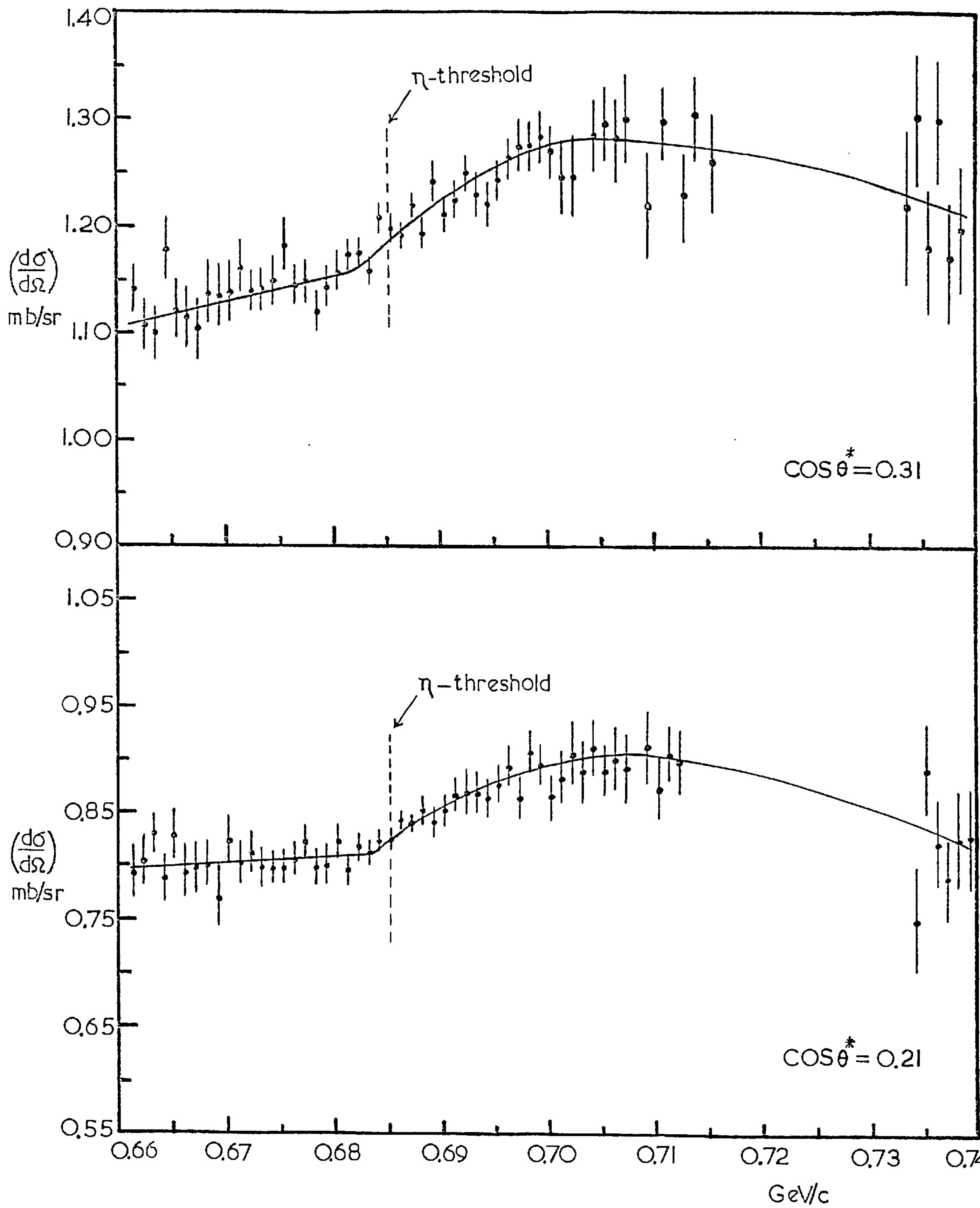

FIG. 7.1(c) $\pi^- p$ elastic scattering differential cross-sections near η-production threshold.

7.2 Relative phase of S_{11} and $f(\theta^*, K)$

It is possible to extract the relative phase of the S_{11} wave and the non-spin flip amplitude $f(\theta^*, K)$, from the behaviour of the cusp. In order to extract the relative phase of S_{11} and $f(\theta^*, K)$, cusps were fitted using relation (2.21). $|p_\eta^*|$, the c.m. momentum of the η was calculated assuming the η-threshold as $p_\pi = 0.6855 \pm 0.0005$ GeV/c. Straight lines are expected if the cross-sections near the η-threshold are plotted against η momentum in the c.m. system. In a range of ~ 14 MeV/c above and below the η-threshold, $\pi^- p$ elastic scattering cross-sections were fitted by the relations,

$$\left(\frac{d\sigma}{d\Omega}\right) = A_0 - A_1 \, |p_\eta^*| \, \mathrm{Cos}A_2 \qquad (7.1a)$$

and

$$\left(\frac{d\sigma}{d\Omega}\right) = A_0 - A_1 \, |p_\eta^*| \, \mathrm{Sin}A_2 \qquad (7.1b)$$

respectively. Where A_0 is the $\pi^- p$ elastic scattering differential cross-section at the η-threshold, A_1 is related to the η-production cross-section and c.m. momentum of $\pi^- p$ elastic scattering and A_2 is related to the relative phase of S_{11} and $f(\theta^*, K)$. A minimum χ^2 was searched for by the fitting programme by varying the parameters A_0, A_1 and A_2. These parameters are tabulated in Table 7.1, for different Cos θ^* regions. The goodness of fit parameter which is defined by χ^2/NDF (NDF = Number of degrees of freedom) is also shown in the last column of Table 7.1. The errors associated with A_0, A_1 and A_2 were calculated from the error matrix and correspond to a change of χ^2 by 1. In the region of Cos $\theta^* > 0.51$, the fit to the data was not very good as the momentum dependence of the cross-section apart from cusp becomes important. So in these regions, the cross-section data within 9 MeV/c from η- threshold were used in the fitting program. This gave a better fit than the previous selection of data points. The values of A_0's and A_2's are within one standard deviation, but the values of

Table 7.1

$\cos\theta^*$	A_o (mb/sr) A_2 (degrees)	χ^2/NDF
-0.59	A_o = 0.416 +- 0.011 A_1 = 1.419 +- 0.059 A_2 = 57.50 +- 3.33	1.07
-0.49	A_o = 0.275 +- 0.020 A_1 = 0.982 +- 0.026 A_2 = 70.47 +- 2.45	0.70
-0.39	A_o = 0.161 +- 0.046 A_1 = 0.697 +- 0.202 A_2 = 87.52 +- 14.94	0.85
-0.29	A_o = 0.099 +- 0.004 A_1 = 0.526 +- 0.004 A_2 = 122.29 +- 0.39	0.98
-0.19	A_o = 0.114 +- 0.022 A_1 = 0.398 +- 0.055 A_2 = 126.81 +- 6.01	0.86
-0.09	A_o = 0.188 +- 0.050 A_1 = 0.316 +- 0.219 A_2 = 171.89 +- 26.63	0.98
0.01	A_o = 0.331 +- 0.050 A_1 = 0.177 +- 0.266 A_2 = 202.71 +- 27.95	0.90
0.11	A_o = 0.525 +- 0.062 A_1 = 0.450 +- 0.297 A_2 = 266.33 +- 25.19	1.04

Table 7.1 (contd.)

$\cos\theta^*$	A_o (mb/sr) A_2 (degrees)	χ^2/NDF
0.21	A_o = 0.828 +- 0.034 A_1 = 0.826 +- 0.243 A_2 = 292.03 +- 9.98	0.52
0.31	A_o = 1.194 +- 0.047 A_1 = 1.048 +- 0.064 A_2 = 305.71 +- 4.31	1.10
0.41	A_o = 1.385 +- 0.023 A_1 = 1.753 +- 0.004 A_2 = 326.86 +- 0.37	1.35
0.51	A_o = 1.834 +- 0.049 A_1 = 2.345 +- 0.031 A_2 = 320.24 +- 1.31	0.91
0.61	A_o = 2.430 +- 0.073 A_1 = 3.325 +- 0.033 A_2 = 333.87 +- 0.33	0.73
0.71	A_o = 3.037 +- 0.037 A_1 = 3.505 +- 0.46 A_2 = 333.30 +- 0.70	1.38
0.81	A_o = 3.809 +- 0.036 A_1 = -------------- A_2 = 327.49 +- 1.38	1.06

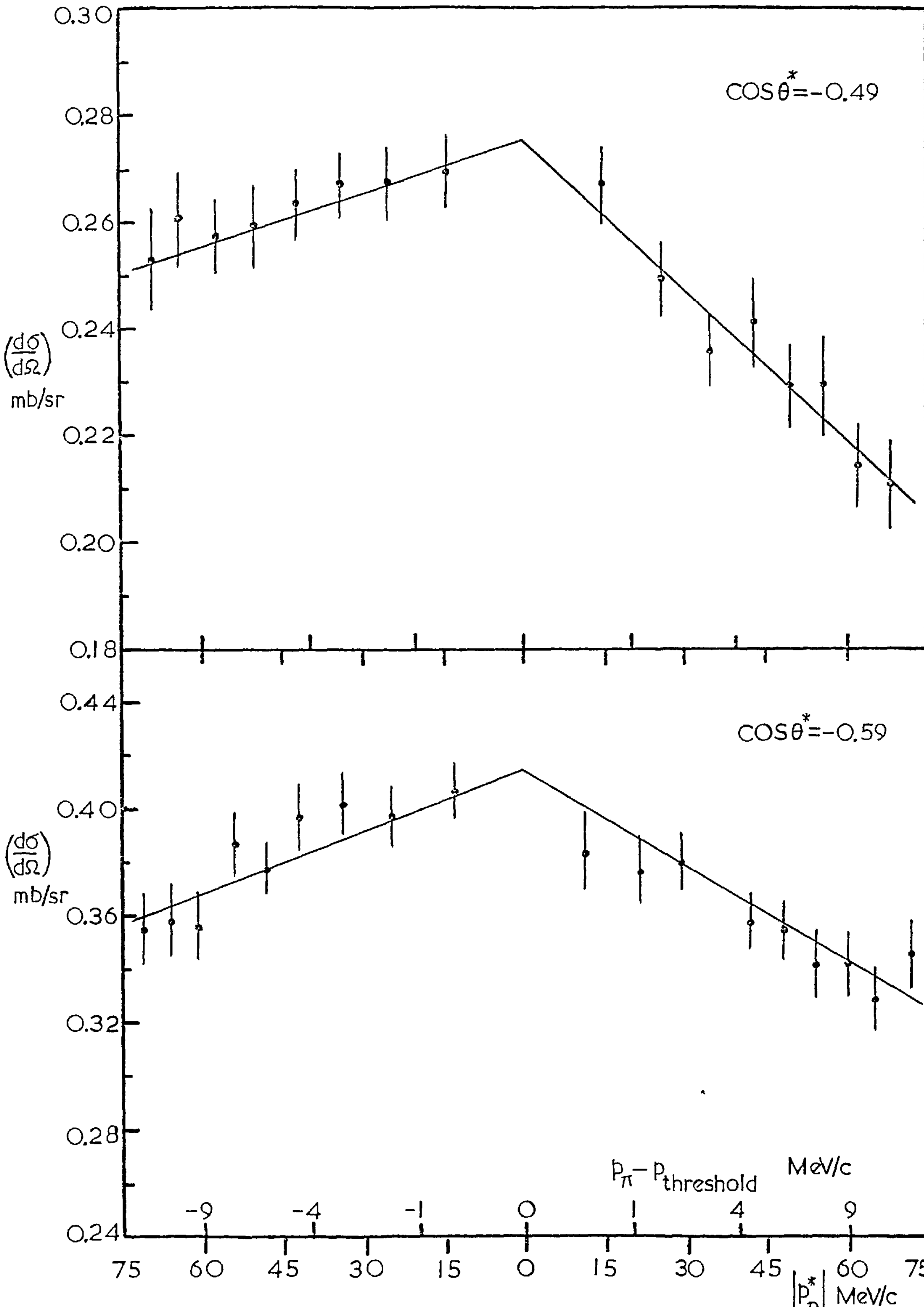

FIG. 7.2(a) Cusp in $\pi^- p$ elastic scattering across the threshold for η-production.

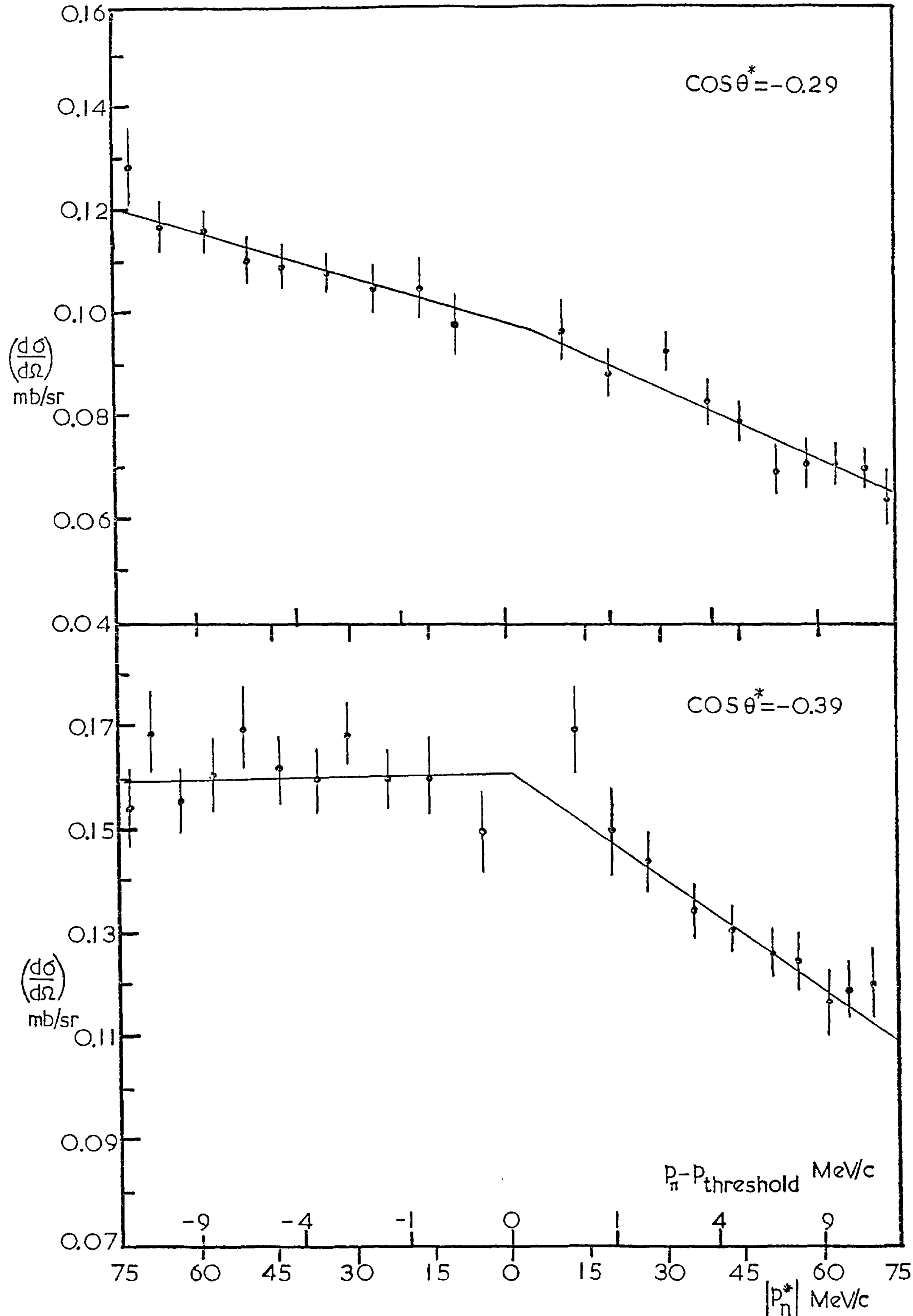

FIG. 7.2(b) Cusp in π^-p elastic scattering across the threshold for η-production.

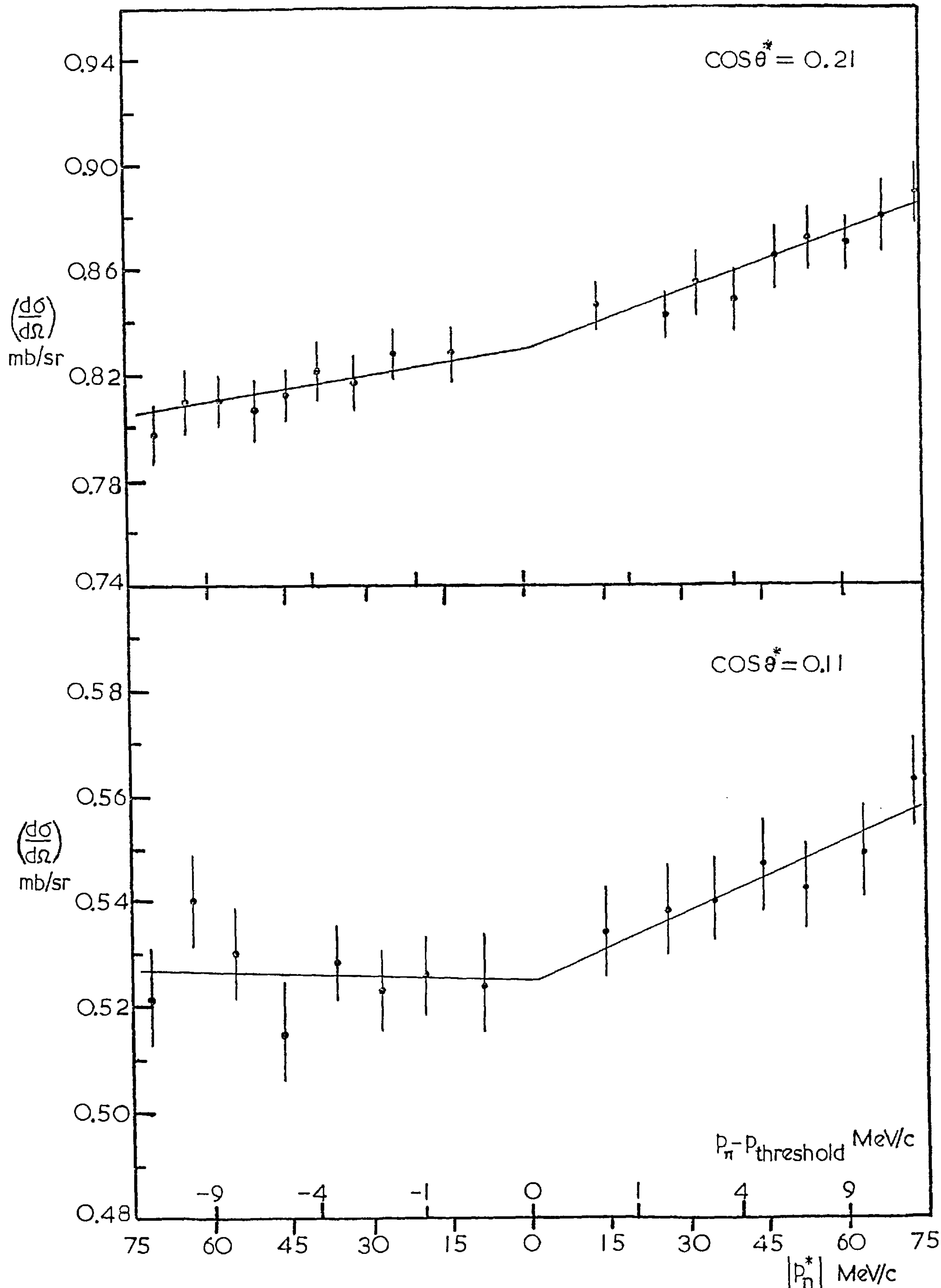

FIG. 7.2(c) Cusp in $\pi^- p$ elastic scattering across the threshold for η-production.

A_1's differ by as much as two standard deviations from the previous fittings. In Figs. 7.2(a)-(c) we have presented some of the cross-sections as a function of $|p^*_\eta|$ ($|p^*_\eta| \simeq 20\,(p_\pi - p_{threshold})^{\frac{1}{2}}$, where all quantities are expressed in MeV/c.) across the threshold for η- production. The straight lines are fits to the data points.

A fit by changing η-production threshold was also made. $|p^*_\eta|$ was calculated from a threshold value of $\sim$ 0.687 GeV/c, which corresponds to m_η = 548.8 MeV (PDG, 1976). The fit was poorer. The value of A_o hardly changes while the values of A_1 and A_2 are within one standard deviation as compared to the previous fittings. Thus the parameters A_o, A_1 and A_2 which we extract from the behaviour of the cusp are not very sensitive to the absolute value of the η- production threshold.

7.3 η-production cross-section

A lower limit of η-production cross-section has been estimated from the behaviour of the cusp in the differential cross-section at $\cos\theta^* = -0.59$, assuming the spin-flip cross-section to be zero. A_1, which entered in relations (7.1a) and (7.1b), is given by

$$A_1 = \frac{K}{2\pi} \sqrt{\left(\frac{d\sigma}{d\Omega}\right)_{thres} - |g(\theta^*, K)|^2} \quad \sigma_{reac} \Big/ |p^*_\eta| \qquad (7.2)$$

where

k = momentum of π^- in the $\pi^- p$ c.m. system at η-threshold

= 0.4325 GeV/c

= 0.6944 $mb^{-\frac{1}{2}}$

$\left(\frac{d\sigma}{d\Omega}\right)_{thres}$ = A_o = $\pi^- p$ elastic differential cross-section at η-threshold

σ_{reac} = production cross-section of $\pi^- p \rightarrow \eta\, n$

Using the values of A_0 and A_1 from Table 7.1, and assuming $|g(\theta^*, \kappa)| \rightarrow 0$, we have,

$$\sigma_{reac} / p^*_\eta \gg (19.91 \pm 0.87)\ \mu b/MeV/c \qquad (7.3)$$

This limit is comparable to the η-production cross-section obtained by Binnie et al (1973), $\sigma_{reac} / p^*_\eta = (21.2 \pm 1.8)\ \mu b/MeV/c$. The production cross-section given by (7.3) clearly shows that the spin flip cross-section for $\pi^- p$ elastic scattering at Cos $\theta^* = -0.59$ is quite small.

7.4 Spin flip and non-spin flip cross-sections

The spin flip and the non-spin flip cross-sections for the $\pi^- p$ elastic scattering at the η-threshold have been evaluated using the η-production cross-section of

$$\sigma_{reac} / p^*_\eta = (21.2 \pm 1.8)\ \mu b/MeV/c.$$

The values of $|g(\theta^*, \kappa)|^2$, $|f(\theta^*, \kappa)|^2$ and $|f(\theta^*, \kappa)|$ have been tabulated for different Cos θ^* in Table 7.2. Fig. 7.3 shows the angular distribution of $\pi^- p$ elastic scattering at the η-threshold. The smooth curves are the fitted curves to the data points. The forward differential cross-section has been calculated from the fitting coefficients and is found to be

$$\left(\frac{d\sigma}{d\Omega}\right)_{\text{Cos } \theta^* = 1} = (5.631 \pm 0.064)\ mb/sr \qquad (7.4a)$$

and

$$| f(0 , \kappa) | = (2.373 \pm 0.014)\ (mb/sr)^{\frac{1}{2}} \qquad (7.4b)$$

Table 7.2

Cos θ*	$\lvert g(\theta^*,k)\rvert^2$ mb/sr	$\lvert f(\theta^*,k)\rvert^2$ mb/sr	$\lvert f(\theta^*,k)\rvert (mb/sr)^{\frac{1}{2}}$
-0.59	0.049 +- 0.070	0.367 +- 0.069	0.606 +- 0.057
-0.49	0.099 +- 0.037	0.176 +- 0.031	0.419 +- 0.037
-0.39	0.073 +- 0.070	0.089 +- 0.053	0.298 +- 0.090
-0.29	0.050 +- 0.010	0.050 +- 0.009	0.225 +- 0.019
-0.19	0.085 +- 0.024	0.029 +- 0.009	0.170 +- 0.028
-0.09	0.170 +- 0.056	0.018 +- 0.025	0.135 +- 0.094
0.01	0.325 +- 0.053	0.006 +- 0.017	0.076 +- 0.114
0.11	0.488 +- 0.079	0.037 +- 0.049	0.192 +- 0.128
0.21	0.704 +- 0.083	0.124 +- 0.076	0.353 +- 0.108
0.31	0.994 +- 0.063	0.200 +- 0.042	0.447 +- 0.047
0.41	0.825 +- 0.098	0.560 +- 0.095	0.748 +- 0.064
0.51	0.832 +- 0.179	1.002 +- 0.172	1.001 +- 0.086
0.61	0.417 +- 0.352	2.014 +- 0.344	1.419 +- 0.121
0.71	0.799 +- 0.386	2.238 +- 0.385	1.496 +- 0.129

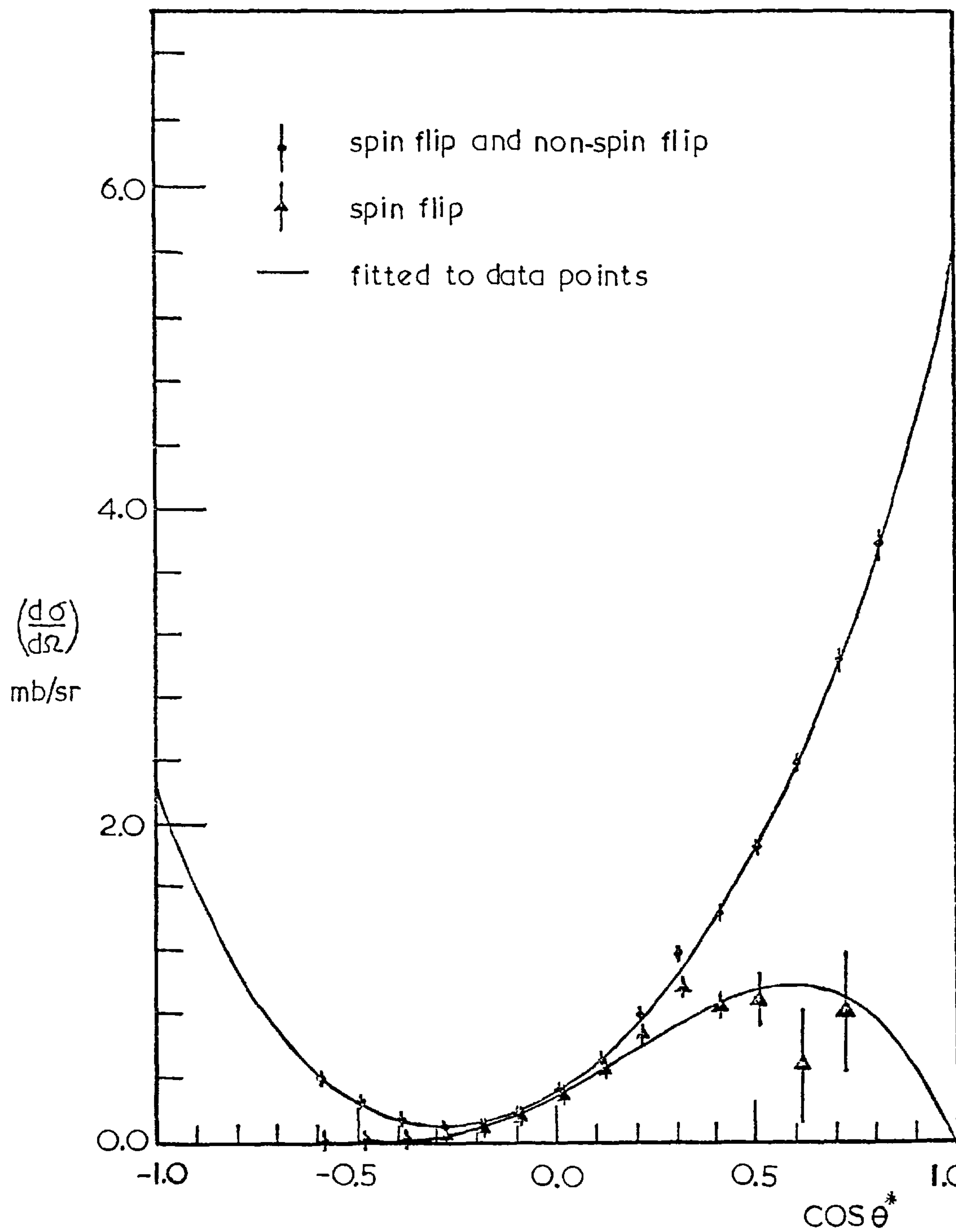

FIG. 7.3 Angular distribution of π^-p elastic scattering at η-threshold.

7.5 Phase of S_{11} and $f(\theta^*, \kappa)$

The measurement of the differential cross-section alone only gives us the modulus of the scattering amplitude. In the π^- p scattering (spin 0 and spin $\frac{1}{2}$), a complete set of measurements will give us the modulii of the spin flip and non-spin flip amplitudes and their relative phase and not the overall angular dependent phase (Martin 1975).

Thus we have the question, can the phase be measured? The phase is defined from the continuity of the scattering amplitude which we assume is a continuous function of K (c.m. momentum) and Cos θ^* (c.m. scattering angle) in the region where $F(\kappa, \text{Cos}\,\theta^*)$ does not vanish. Martin (1975) has discussed in detail regarding the phase and scattering amplitude. Though in principle one can measure phases, the direct measurement of phase is almost impossible in high energy physics.

Phase has observable consequences in the situations where multiple scattering occurs, such as the scattering from deuterons. Since the internal dynamics of the scattering system is not well understood it is not possible in practice to extract the phase. Thus Bowcock et al (1975) regarded the overall phase of the amplitude as unmeasurable.

From the relative phase of the S_{11} and $f(\theta^*, \kappa)$ as a function of Cos θ^*, in principle we can determine the phase of S_{11} and $f(\theta^*, \kappa)$. For this we proceed as follows:

Optical theorem gives us,

$$\text{Im}f(0, \kappa) = (\kappa/4\pi)\,\sigma_{tot} \qquad (7.5)$$

were κ is the c.m. momentum and σ_{tot} is the π^-p total cross-section at the η-threshold. Precise measurements of total cross-section in this momentum range had been carried out by Carter et al (1968) and Davidson et al (1972). Davidson result gives σ_{tot} at the η-threshold

$$\sigma_{tot} = (41.5 \pm 0.13) \text{ mb} \qquad (7.6)$$

From (7.5) and (7.6), we have,

$$\mathrm{Im} f(0, K) = (2.293 \pm 0.007) \qquad (7.7)$$

The phase of $f(\theta^{*}, K)$ in the forward direction is related to $\mathrm{Im} f(0, K)$ and $| f(0, K) |$ by,

$$\mathrm{Sin}\, \alpha (0) = \mathrm{Im} f(0, K) / | f(0, K) | \qquad (7.8)$$

where $\alpha (0)$ is the phase of $f(\theta^{*}, K)$ at $\theta^{*} = 0$. $\mathrm{Im} f(0, K)$ is positive and cannot vanish unless the scattering amplitude is identically zero at all angles and at all energies. So we conclude that

$$0 < \alpha(0) < \pi \qquad (7.9)$$

Using our value of $| f(0, K) |$ from (7.4b) in (7.8) we have,

$$\alpha (0) = 75.09^{\circ} \pm 1.43^{\circ} \qquad (7.10)$$

The phase may also be

$$\alpha (0) = 104.91^{\circ} \pm 1.43^{\circ} \qquad (7.11)$$

which will also give the same amplitude for $| f(0, K) |$ but the sign of $\mathrm{Re} f(0, K)$

becomes negative. The sign of Ref(0, K) can be fixed from the interference of Coulomb and nuclear interaction. The sign and magnitude of the real part of the forward scattering amplitude had been determined below 2GeV/c by Baillon et al (1974) and the predicted values of Ref(0, K)/Imf(0, K) from the dispersion relation had also be given by Höhler et al (1972). In the momentum range of our interest Ref(0, K) is positive. Thus the phase of $f(\theta^{*}, K)$ in the forward direction at the η-threshold is,

$$\alpha(0) = 75.09^{o} \pm 1.43^{o} \qquad (7.12)$$

In Fig. 7.4 we have shown the variation of $(2\delta_{o} - \alpha(\theta^{*}))$ as a function of $\cos\theta^{*}$. It is seen that as one approaches the forward or the backward direction, the variation of $(2\delta_{o} - \quad (\theta^{*}))$ with $\cos\theta^{*}$ becomes very small. In order to determine the phase of S_{11} wave we have to make an extrapolation of $(2\delta_{o} - \alpha(\theta^{*}))$ to $\cos\theta^{*} = 1$. A linear extrapolation of the data gives,

$$2\delta_{o} - \alpha(0) = 335.16^{o} \pm 2.83^{o} \qquad (7.13)$$

Combining (7.12) and (7.13), we have δ_{o}, the phase of the S_{11} wave at the η-threshold

$$\delta_{o} = 25.13^{o} \pm 1.59^{o} \qquad (7.14)$$

In Table 7.3 we have tabulated $(\alpha(\theta^{*}) - \delta_{o})$, the phase difference between $f(\theta^{*}, K)$ and S_{11}, and $\alpha(\theta^{*})$, the phase of $f(\theta^{*}, K)$, as a function of $\cos\theta^{*}$ for $\pi^{-}p$ elastic scattering at the η-threshold.

It should be noted that the phase of S_{11} wave is unique. The ambiguity noted by Crichton (1966), which arises from a variety of artificial cases and which is assumed to be universally true in the elastic region does not arise in our S_{11} phase δ_o .

Our constructed non-spin flip amplitude at the η -threshold is shown in Fig. 7.5. We have made a comparision of our amplitude with the different phase shift solutions (Fig. 7.6). The agreement between our amplitude which we find out from a completely independent method, and different phase shift solutions is generally good. We prefer solutions where the amplitude passes the negative axis of Imf($\overset{*}{\theta}$) in the regions of Cos $\overset{*}{\theta} \simeq -0.20$. In these regions the Glasgow solution (Davies 1970) differs considerably from ours. Our phase of the S_{11} wave, $\delta_o = 25.13^o \pm 1.59^o$ is in agreement with the solution of Bareyre et al (1968) $\delta_o \simeq 26.5^o \pm 2.0^o$, and not differ considerably from that of Roper et al (1965) $\delta_o \simeq 30.5^o$, Bransden et al solution I $\delta_o \simeq 32.5^o$, and the Glasgow solution B $\delta_o \simeq 29.0^o$.

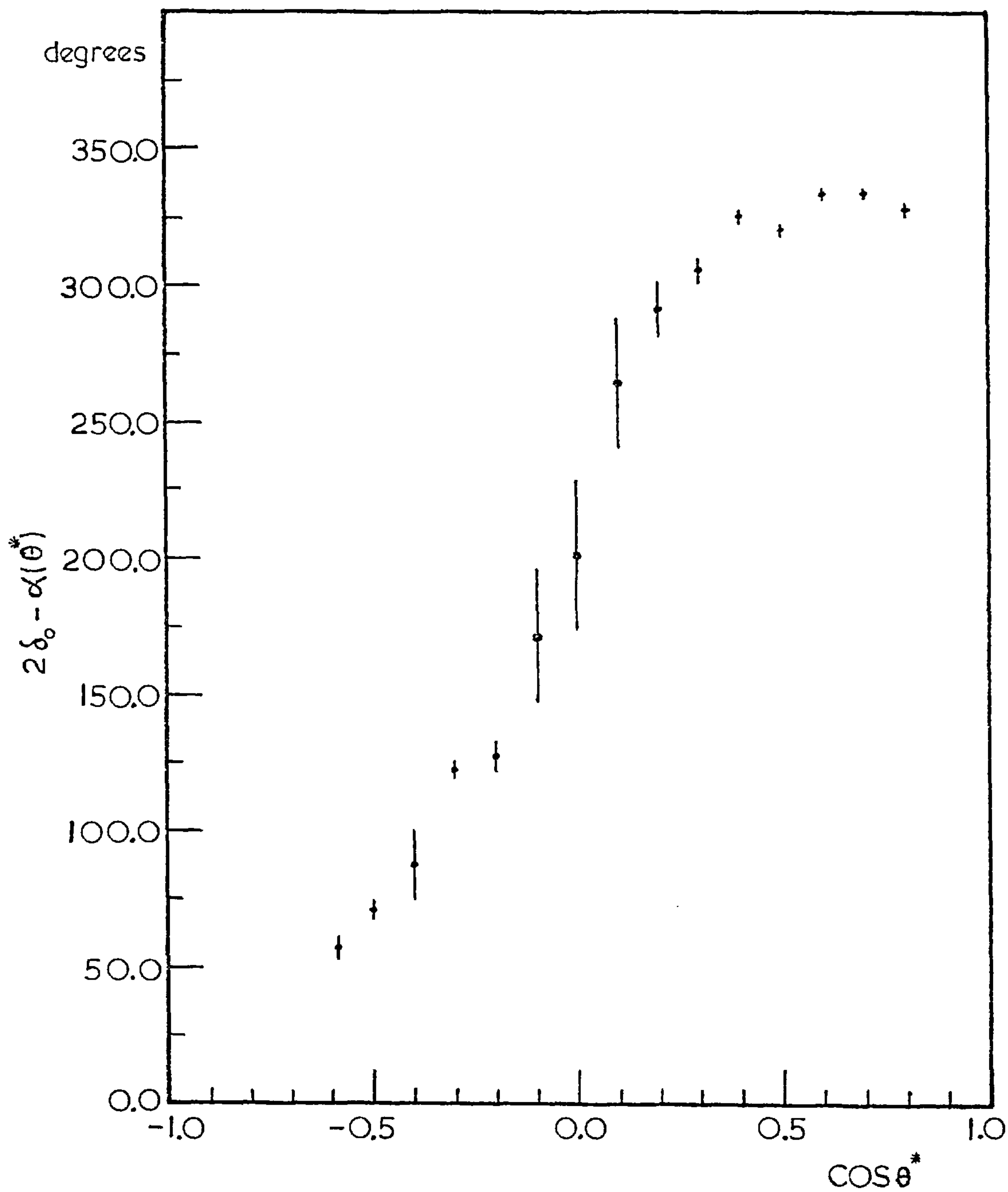

FIG. 7.4. The variation of $2\delta_o - \alpha(\theta^*)$ as a function of $\cos\theta^*$ for $\pi^- p$ elastic scattering at η-threshold.

Table 7.3

$\cos\theta^*$	$(\alpha(\theta^*) - \delta_0)$ (degrees)	$\alpha(\theta^*)$ (degrees)
-0.59	327.63 +- 3.69	352.76 +- 4.59
-0.49	314.66 +- 2.92	339.78 +- 4.01
-0.39	297.61 +- 15.03	322.73 +- 15.27
-0.29	262.84 +- 1.64	287.96 +- 3.19
-0.19	258.44 +- 6.22	283.44 +- 6.80
-0.09	213.24 +- 26.68	238.36 +- 26.82
0.01	182.42 +- 28.00	207.54 +-28.13
0.11	118.80 +- 25.24	143.92 +- 25.38
0.21	93.11 +- 10.10	118.23 +- 10.47
0.31	79.42 +- 4.59	104.54 +- 5.35
0.41	58.27 +- 1.63	83.39 +- 3.19
0.51	64.89 +- 2.06	90.01 +- 3.43
0.61	51.27 +- 1.62	76.39 +- 3.19
0.71	51.84 +- 1.74	76.96 +- 3.25
0.81	57.64 +- 2.10	82.76 +- 3.46
1.00	49.97 +- 3.25	75.09 +- 4.25

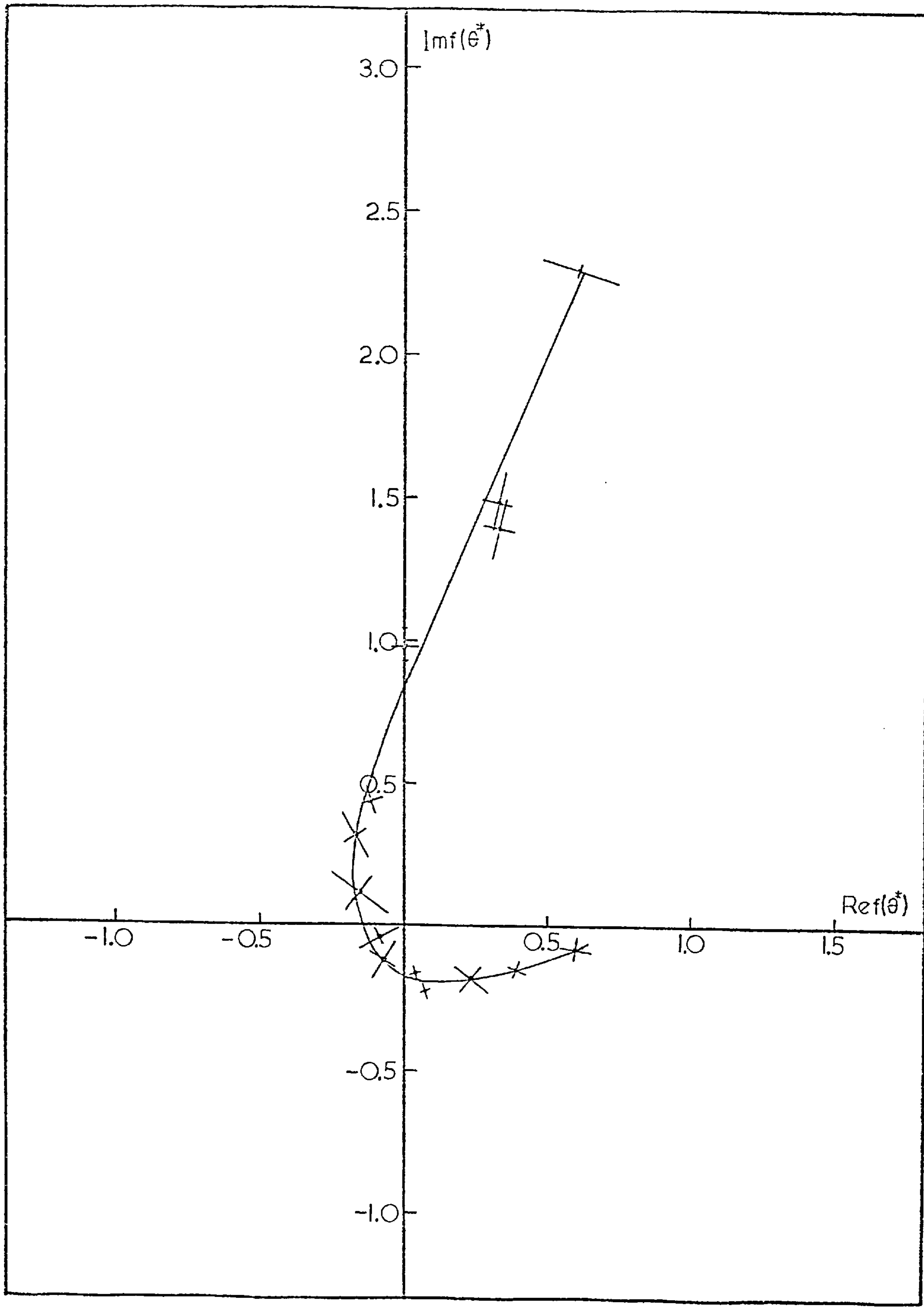

FIG. 7.5 The non-spin flip amplitude for $\pi^- p$ elastic scattering at η-threshold. The smooth curve is the hand drawn and not a fit to the data points.

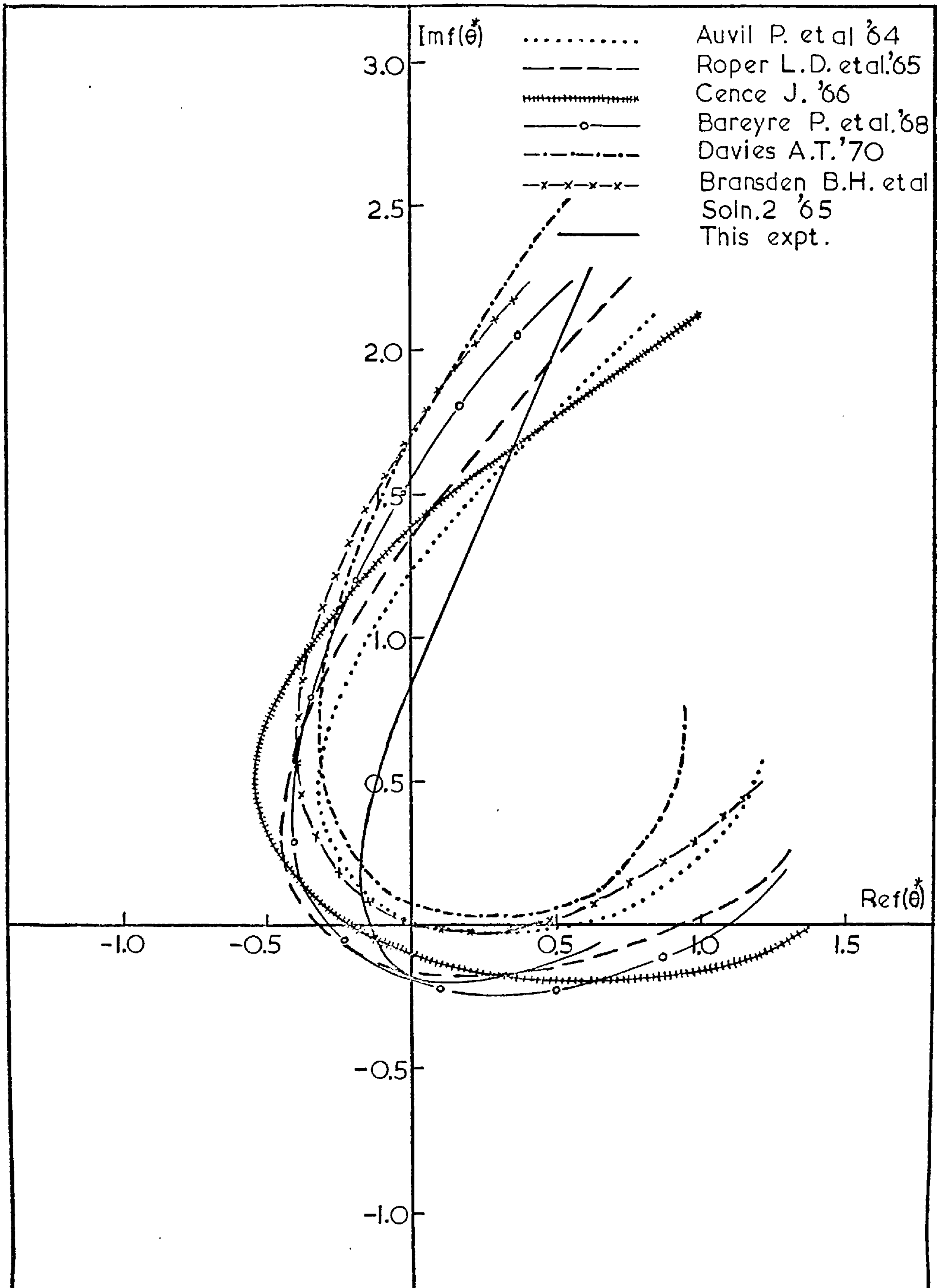

FIG. 7.6 Comparision of non-spin flip amplitude for $\pi^- p$ elastic scattering at η-threshold from this experiment with different phase shift solutions.

8. Conclusions

Using the analytic continuity and the conservation of probability of the scattering amplitude, we have derived the expression for the $\pi^- p$ elastic scattering differential cross-section near the threshold for a reaction channel. The expression gives the behaviour of the cusp, i.e. the discontinuity that occurs when the energy threshold for a competing reaction is crossed. We have used this technique at the η n threshold, which is known to be produced in the S_{11} state, to extract valuable information.

When the $\pi^- p$ elastic scattering differential cross-section is plotted as a function of beam momentum for each Cos θ^* bin a very clear cusp or discontinuity is observed. This cusp in the differential cross-section occurs for all the scattering angles at the same beam momentum, namely 0.6855 ± 0.0005 GeV/c, which closely corresponds to the η n threshold. The cusp changes in shape with the c.m. scattering angle. At a fixed c.m. scattering angle when one plots the differential cross-section as a function of $|p^*_\eta|$ (c.m. momentum of the η meson in the η n system), it closely corresponds to two straight lines, one below and the other above the η -threshold, as predicted by the theory.

A cusp in the $\pi^- p$ elastic scattering gives an independent method for the determination of the relative phase of S_{11} wave and the non-spin flip amplitude $f(\theta^*, K)$, as a function of Cos θ^*. It is also possible to extract the phase of the S_{11} wave. This was determined to be, $\delta_0 = 25.13^\circ \pm 1.59^\circ$. This phase value will be helpful for the comparision of different phase shift solutions, where the phase of the S_{11} wave ranges from $\delta_0 = 26.5^\circ \pm 2.0^\circ$ (Bareyre et al 1968) to $\delta_0 \sim 45^\circ$ (Glasgow solution A).

At $\theta^* = 0^\circ$ and 180°, the magnitude of cusp depends only on the production cross-section, while at other angles, $g(\theta^*, K)$ contributes to the cusp. By selecting the region $\cos\theta^* = -0.59$, where $g(\theta^*, K)$ is expected to be small, we have set a lower limit for σ_{reac}. Our limit $\sigma_{reac} / p^*_{\eta n} \geqslant (19.91 \pm 0.87)$ $\mu b/(MeV/c)$ is comparable to the measured η- production cross-section of Binnie et al (1973), $\sigma_{reac} / p^*_{\eta n} = (21.2 \pm 1.8)$ $\mu b/(MeV/c)$, thus showing the spin flip amplitude in this region to be quite small.

Using the η-production cross-section of Binnie, we have found out the spin flip and the non-spin flip cross-sections for the $\pi^- p$ elastic scattering at the η-threshold, over a wide range of $\cos\theta^*$. Our constructed non-spin flip amplitude is compared with the results of different phase shift solutions. We prefer the solutions where the non-spin flip amplitude passes the negative axis of $\mathrm{Im}f(\theta^*)$ in the region of $\cos\theta^* \sim -0.20$. In these regions, our amplitude is quite different from that of the Glasgow solution A.

The measured differential cross-sections $\left(\frac{d\sigma}{d\Omega}\right)$ were fitted with Legendre polynomials, and it is of interest that there is no evidence for the $\sim$ 36 MeV width N^* suggested in the Glasgow solution.

The method of cusp can also be applied to $\pi^- p \rightarrow K^0 \Lambda^0$ threshold and to other thresholds.

Acknowledgements

I would like to thank Professors I. Butterworth and P.T. Matthews for the opportunity to carry out research as a member of the High Energy Physics Group at Imperial College, London.

I am deeply indebted to my supervisor, Dr. D.M. Binnie, for his guidance, advice and encouragement throughout my period of research.

I wish to thank my colleagues Dr. J. Carr, Dr. J. Keyne, Dr. W.G. Jones, Dr. D.A. Garbutt, Dr. I. Siotis, Dr. N.C. Debenham, Mr. H. Karami, Mr. P. Mossidis for the useful discussions and suggestions and to Dr. S. Banerjee for his invaluable suggestions in fitting the data.

I would like to thank Mr. R.F. Hobbs, Mr. D.G. Miller and Mr. J. Hiddlestone for their assistance in the experimental setup.

I wish my sincere thanks to the Ministry of Education, Govt. of India, for the award of a research scholarship.

Finally, but by no means least, I must thank my parents without whose support and encouragement I should not have been able to indulge in the dilettante pursuit of an education for the better part of the past twentyfive years.

References

Abillon, J.M., Borg, A., Crozon, M., Leray, Th., Mendiburu, J.P. and Tocqueville, J., 1972, Nucl. Phys., B46, 630.

Adair, R.K., 1958, Phys. Rev., 111, 632.

Auvil, P., Lovelace, C., Donnachie, A. and Lea, A.T., 1964, Phys. Letters, 12, 76.

Baillon, P., Brickman, C., Eberhard, Ph., Ferro-Luzzi, M., Perrecue, J.M., Tripp, R.D., Ypsilantis, T., Dēclais, Y. and Séguinot, J., 1974, Phys. Letters, 50B, 387.

Ball, J.S. and Frazer, W.R., 1961, Phys. Rev. Letters, 7, 204.

Ball, J.S., 1966, Phys. Rev., 149, 1191.

Bareyre, P., Brickman, C. and Villet, G., 1965, Phys. Letters, 18, 342.

Bareyre, P., Brickman, C. and Villet, G., 1968, Phys. Rev., 165, 1730.

Baz', A.I., 1958, Sovt. Phys. JETP., 6, 709.

Baz', A.N. and Okun', L.B., 1959, Sovt. Phys. JETP., 8, 526.

Binnie, D.M. and Duane, A., 1970, Nucl. Instr. Meth., 77, 329.

Binnie, D.M., Camilleri, L., Debenham, N.C., Duane, A., Garbutt, D.A., Holmes, J.R., Jones, W.G., Keyne, J., Lewis, M., Siotis, I., Upadhyay, P.N., Burton, I.F. and McEwen, J.G., 1973, Phys. Rev., D8, 2789.

Bowcock, J.E. and Burkhardt, H., 1975, Rept. Prog. Phys., 38, 1099.

Bransden, B.H., O'Donnell, P.J. and Moorhouse, R.G., 1965, Phys. Rev., 139, B1566.

Breskin, A., Charpak, G. and Santiard, J.C., 1974, Nucl. Instr. Meth., 119, 1.

Brody, A.D., Leith, D.W.G.S., Levi, B.G., Shen, B.C., Herndon, D., Longacre, R., Price, L., Rosenfeld, A.H. and Söding, P., 1969, Phys. Rev. Letters, 22, 1401.

Brody, A.D., Cashmore, R.J., Kernan, A., Leith, D.W.G.S., Levi, B.S., Shen, B.C., Berge, J.P., Herndon, D.J., Longacre, R., Price, L.R., Rosenfeld, A.H. and Söding, P., 1971, Phys. Rev., D3, 2619.

Bulos, F., Lanou, R.E., Pifer, A.E., Shapiro, A.M., Widgoff, M., Panvini, R., Brenner, A.E., Bordner, C.A., Law, M.E., Ronat, E.E., Strauch, K., Szymanski, J.J., Bastien, P., Brabson, B.B., Eisenberg, Y., Feld, B.T., Fischer, V.K., Pless, I.A., Rosenson, L., Yamamoto, R.K., Calvelli, G., Guerriero, L., Salandin, G.A., Tomasin, A., Ventura, L., Voci, C. and Waldner, F., 1964, Phys. Rev. Letters, 13, 468.

Carter, A.A., Riley, K.F., Tapper, R.J., Bugg, D.V., Gilmore, R.S., Knight, K.M., Salter, D.C., Stafford, G.H., Wilson, E.J.N., Davies, J.D., Dowell, J.D., Hattersley, P.M., Homer, R.J. and O'Dell, A.W., 1968, Phys. Rev., 168, 1457.

Cence, J., 1966, Phys. Letters, 20, 306.

Charpak, G., Sauli, F. and Duinker, W., 1973, Nucl. Instr. Meth., 108, 413.

Charpak, G., 1974, Workshop on research goals for Cosmic Rays Astrophysics in 1980s ESRIN (Frascati).

Cheng, D.G., Kozanecki, W.A., Piccioni, R.L., Rubbia, C., Sulak, R.L., Weedon, H.J. and Whittaker, J., 1974, Nucl. Instr. Meth., 117, 157.

Crabb, D.G., Keller, R., O'Fallon, J.R., Richards, T.J., Ott, R.J., Trischuk, J., Va'vra, J. and Schroeder, L.S., 1971, Phys. Rev. Letters, 27, 216.

Crichton, J.H., 1966, Nuovo Cim., A45, 256.

Davidson, D., Caldwell, P.K., Jenkins, E.W., Kalbach, R.M., Petersen, D.V., Pifer, A.E. and Rothschild, R.E., 1972, Phys. Rev., D6, 1199.

Davies, A.T. and Moorhouse, R.G., 1967, Nuovo Cim., 52A, 1112.

Davies, A.T., 1970, Nucl. Phys., B21, 359.

Debenham, N.C., Binnie, D.M., Camilleri, L., Carr, J., Duane, A., Garbutt, D.A., Jones, W.G., Keyne, J., Siotis, I. and McEwen, J.G., 1975, Phys. Rev., D12, 2545.

Dobson, Jr. P.N., 1966, Phys. Rev., 146, 1022.

Donnachie, A., Kirsopp, R.G. and Lovelace, C., 1968, Phys. Letters, 26B, 161.

Duke, P.J., Jones, D.P., Kemp, M.A.R., Murphy, P.G., Prentice, J.D. and Thresher, J.J., 1966, Phys. Rev., 149, 1077.

Eisler, F., Franzini, P., Gaillard, J.M., Garfinkel, A., Keren, J., Plano, R., Prodell, A. and Schwartz, M., 1961, Rev. Mod. Phys., 33, 436.

Feltesse, J., Ayed, R., Bareyre, P., Borgeaud, P., David, M., Ernwein, J., Lemoigne, Y. and Villet, G., 1975, Nucl. Phys., B93, 242.

Foeth, H., Hammarström, R. and Rubbia, C., 1973, Nucl. Instr. Meth., 109, 521.

Guisan, O., Kirz, J., Sonderegger, P., Stirling, A.V., Borgeaud, P., Bruneton, C., Falk-Vairant, P., Amblard, B., Caversasio, C., Guilland, J.P. and Yvert, M., 1965, Phys. Letters, 18, 200.

Hendry, A.W. and Moorhouse, R.G., 1965, Phys. Letters, 18, 171.

Höhler, G. and Jakob, H.P., 1972, Tables of pion-nucleon forward amplitudes, Karlsruhe University (unpublished).

Jones, W.G., 1966, Ph.D. Thesis, University of London (unpublished).

Lemoigne, Y., Ganet, P., Marty, P., Ayed, R., Bareyre, P., Borgeaud, P., David, M., Ernwein, J., Feltesse, J. and Villet, G., 1973, Baryon Resonances Ed. E.C. Fowler (Prudue University, West Lafayette, Indiana).

Martin, A., 1975, CERN Preprint TH. 2077.

Nauenberg, M. and Pais, A., 1961, Phys. Rev., 123, 119.

Pais, A., 1961, CERN Seminar, CERN 61-30.

Particle Data Group, 1976, Rev. Mod. Phys., 48, No2.

Persner, A., Kraemer, R., Nussbaum, M., Richardson, C., Schlein, P., Strand, R., Toohig, T., Block, M., Engler, A., Gessaroli, R. and Meltzer, C., 1961, Phys. Rev. Letters, 7, 421.

Philip, R.J.N. and Rarita, W., 1965, Phys. Rev. Letters, 15, 807.

Richards, W.B., Chiu, C.B., Eandi, R.D., Carl Helmholz, A., Kenney, R.W., Moyer, B.J., Poirier, J.A., Cence, R.J., Peterson, V.Z., Sehgal, N.K. and Stenger, V.J., 1966, Phys. Rev. Letters, 16, 1221.

Richards, T.J., Crabb, D.G., Keller, R., O'Fallon, J.R., Ott, R.J., Trischuk, J., Va'vra, J. and Schroeder, L.S., 1974, Phys. Rev., D10, 45.

Roper, L.D., Wright, R.M. and Feld, B.T., 1965, Phys. Rev., 138, B190.

Rothschild, R.E., Bowen, T., Caldwell, P.K., Davidson, D., Jenkins, E.W., Kalbach, R.M., Petersen, D.V. and Pifer, A.E., 1972, Phys. Rev., D5, 499.

Saudinos, J., Duchazeaubeneix, J.C., Laspalles, C. and Chaminade, R., 1973, Nucl. Instr. Meth., 111, 77.

Uchiyama-Campbell, F., 1965, Phys. Letters, 18, 189.

Walenta, A.H., 1973, Nucl. Instr. Meth., 111, 467.

Wigner, E.P., 1948, Phys. Rev., 73, 1002.

Wolf, S.E., Schmitz, N., Lloyd, L.J., Laskar, W.Jr., Crawford, F.S., Button, J., Anderson, J.A. and Alexander, G., 1961, Rev. Mod. Phys., 33, 439.